POLITECNICO DI TORINO

Master's Degree in Mechatronic Engineering

Master's Degree Thesis

Localization of a Magnetically Actuated Capsule Endoscope: Performance Assessment and Proposal of an Improved Algorithm

Supervisors

Prof. Alessandro RIZZO

Dr. Bruno SCAGLIONI

Prof. Pietro VALDASTRI

Candidate

Francesco VERZOBIO

October 2023

Alla mia famiglia

Abstract

Colorectal cancer is a significant global health concern, ranking as the third most prevalent malignancy and the second most deadly cancer. Early detection of cancer plays a pivotal role in improving the chances of survival. Consequently, through colonoscopy, medical professionals conduct visual examinations of the colon to identify any early signs of cancer.

Existing endoscopes have been associated with concerns regarding tissue damage and patient discomfort, leading to a reluctance among patients to undergo recommended screening procedures. For this reason, significant efforts have been made over the past two decades to develop **alternative devices**. In particular, the STORM Lab has implemented a robotic platform called **Magnetic Flexible Endoscopy** (MFE). The MFE stands out for its remarkable front-pull actuation of the endoscopic tip facilitated by an external magnet. This revolutionary approach eliminates the need for rear-push mechanical actuation and the use of semi-rigid insertion tubes.

Accurately estimating the capsule pose is crucial for magnetic actuation systems to apply the required forces and torques effectively. Therefore, the STORM Lab developed a **localization algorithm based on the Particle Filter** (PF).

The **first objective** of the thesis project was to **estimate in real-time the correctness of the localization algorithm** developed at STORM Lab for the MFE. Therefore, a comprehensive exploration of various parameters was undertaken. Initially, tests were conducted to ascertain the interrelationships between the parameters. This process aimed to establish how these parameters should be interconnected and how their values could be combined to yield meaningful insights into the localization quality. Additionally, specific thresholds were defined to discern between good and bad localization. Subsequently, a validation phase was implemented to rigorously examine and confirm the effectiveness of the identified parameters and thresholds in different scenarios.

The **second goal** of the project was to develop a **new localization algorithm**. For this purpose, two possible algorithms were analyzed, and the **Unscented Kalman Filter** (UKF) was identified as the most suitable. Following the development of the novel localization algorithm, the UKF was tested to determine its parameters optimally. Subsequently, a series of static tests were conducted to validate the new algorithm and compare its results with those of the PF. The **concluding phase of the project** involved the **fusion of the two developed algorithms**, PF and UKF, strategically extracting the strengths of each in pursuit of a unified localization algorithm.

Given that the errors resulting from both localization algorithms, PF and UKF, are comparable, it is possible to state that the **lower limit of error has been attained** and is fundamentally contingent on the system's intrinsic characteristics. In pursuit of refining localization, any attempts to achieve further enhancements would necessitate altering the system.

Table of Contents

List of Tables

List of Figures

Acronyms

6-DOF
: six degrees-of-freedom

ADC
: analog-to-digital converter

CRC
: colorectal cancer

EKF
: extended kalman filter

EPM
: external permanent magnet

GI
: gastrointestinal

GRV
: gaussian random variable

IMU
: inertial measurement unit

IPM
: internal permanent magnet

LPF
: low-pass filter

MFE
: magnetic flexible endoscopy

PDF
: probability density function

PF
: particle filter

RV
: random variable

UKF
: unscented kalman filter

Chapter 1

Introduction

The main objectives of this work are as follows:

- Estimate in real-time the correctness of the localization developed at STORM Lab for the Magnetic Flexible Endoscopy (MFE), using certain parameters.
- Implementation of a new localization algorithm.
- Implementation of an overall localization algorithm, including both the algorithm previously developed at STORM Lab and the newly implemented algorithm, in order to improve the localization accuracy.

This first chapter explains the motivations for developing such work, the magnetic capsule endoscopy, and the several localization strategies already implemented.

The second chapter presents an in-depth exploration of the localization algorithm developed at STORM Lab. This is a fundamental starting point for comprehending the subsequent real-time evaluation of the algorithm's performance and its integration with the new algorithm, ultimately leading to enhanced overall localization capabilities. Finally, the state of the art of estimation algorithms for localization that can be used is presented.

In the third chapter, the parameters identified to assess the correctness of localization in real time are presented, and the results obtained with these parameters are shown.

In the fourth chapter, the newly implemented localization algorithm is explained.

The fifth chapter shows the overall localization algorithm, which includes both the algorithm previously developed by STORM Lab and the new algorithm presented in this work.

In the sixth and final chapter, future work to further improve localization is proposed, and conclusions are drawn.

Finally, tables, graphs, and the developed code are included in the appendix to provide all the material needed to understand better the work developed.

1.1 Clinical motivation

Colorectal cancer (CRC) stands as a significant global health concern, ranking as the third most prevalent malignancy and the second most deadly cancer. In 2020 alone, an estimated 1.9 million people were diagnosed with CRC, resulting in approximately 0.9 million deaths worldwide. This alarming trend is particularly pronounced in highly developed countries, while middle- and low-income countries are witnessing an unfortunate rise in CRC cases due to westernization (see Figure 1.1). Furthermore, an unsettling surge in early-onset CRC cases is also being observed [1].

The mounting number of CRC cases presents an ever-growing challenge for public health on a global scale. To effectively address this issue, raising awareness about CRC is crucial. By fostering awareness, it is possible to encourage individuals to make healthier lifestyle choices, advocate for novel and effective strategies in CRC management, and implement comprehensive screening programs on a worldwide scale. These proactive measures are imperative to curbing the morbidity and mortality rates of CRC in the future [1].

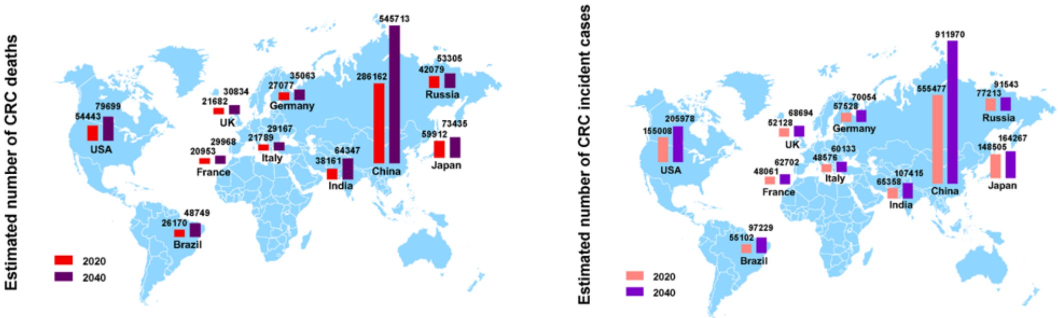

Figure 1.1: Estimated number of CRC deaths and of CRC incident cases [1].

Early detection of cancer plays a pivotal role in improving the chances of survival [2] [3] [4]. Consequently, medical professionals frequently utilize endoscopes to conduct visual examinations of the accessible regions within the gastrointestinal (GI) tract to identify any early signs of cancer.

Endoscopy is a medical procedure employing an endoscope, a versatile instrument equipped with diagnostic and therapeutic capabilities, to examine the interior of various hollow organs and body cavities. Areas of focus encompass the gastrointestinal tract, respiratory tract, urinary tract, female reproductive system, and other closed cavities within the body. Notably, colonoscopy stands as one of the most prevalent screening procedures, carried out using an endoscope to investigate the colon and rectum (see Figure 1.2).

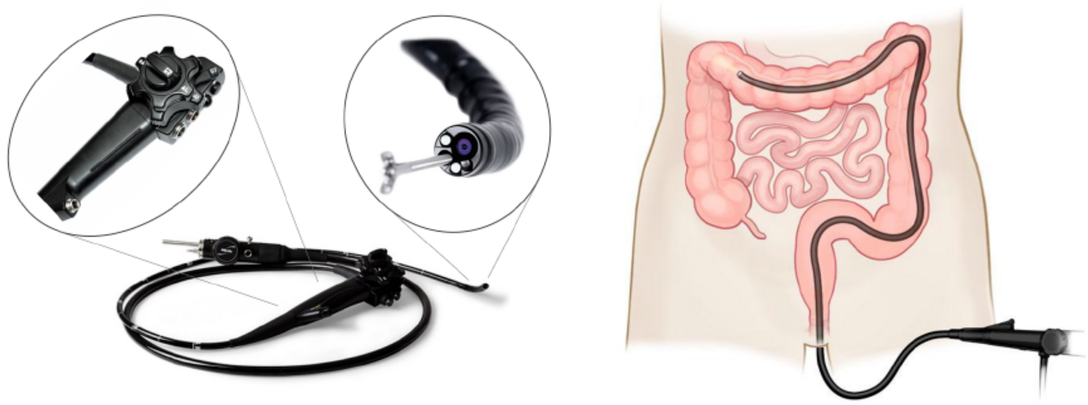

Figure 1.2: Traditional endoscope: on the left the control system for the bending section and endoscopic tip; on the right the illustration of a traditional colonoscopy [5].

Nevertheless, existing endoscopes have been associated with concerns regarding tissue damage and patient discomfort, leading to a reluctance among patients to undergo recommended screening procedures [6]. Moreover, certain regions of the GI tract, such as the small intestine, present challenges in accessibility using conventional semi-rigid endoscopes. In response to these limitations, significant efforts have been made over the past two decades to develop alternative devices capable of visualizing the GI tract and overcoming these obstacles.

The field of magnetically actuated mesoscale devices (capsules) remains an area of active research, displaying remarkable potential in terms of maneuverability and a substantial reduction in risks typically associated with conventional endoscopies. Among these innovations, actively controlled devices stand out as particularly promising, leveraging computer algorithms to generate or manipulate magnetic fields. This advancement has the power to revolutionize GI endoscopy, transforming patient perceptions and attitudes towards recommended screening procedures [7] [8].

1.2 Magnetic capsule endoscopy

To overcome the constraints of traditional endoscopes, researchers are delving into the potential of magnetic fields to wirelessly transmit forces and torques, enabling the translation and manipulation of capsule endoscopes. This innovative approach seeks to mitigate the limitations associated with conventional endoscopic techniques.

The system shown in Figure 1.3 was developed by the Science and Technologies Of Robotics in Medicine (STORM) Lab of Vanderbilt University (Nashville, TN) and of the University of Leeds (Leeds, UK). This robotic platform, called Magnetic Flexible Endoscopy (MFE), will be presented in detail in the second chapter.

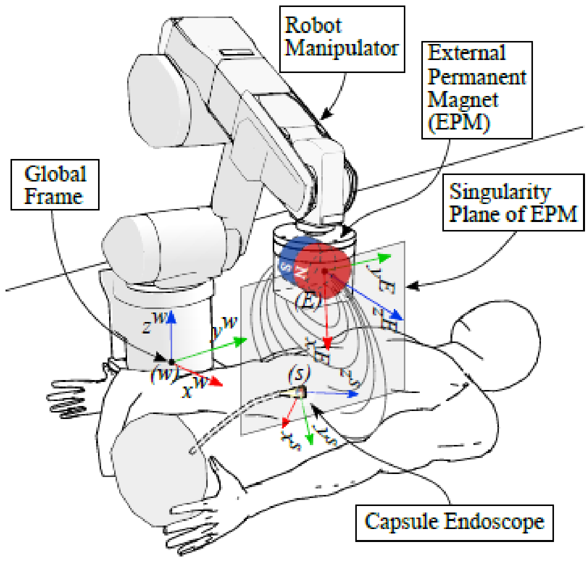

Figure 1.3: Schematic of magnetic capsule endoscopy [9].

The MFE stands out for its remarkable front-pull actuation of the endoscopic tip, facilitated by an external magnet placed outside the patient's body. This revolutionary approach eliminates the need for rear-push mechanical actuation and the use of semi-rigid insertion tubes, which previously aimed to prevent buckling and tissue stress-related trauma. However, manual operation of magnetic actuation isn't straightforward, necessitating computer-assisted operations to assist operators during training and complex clinical maneuvers. The MFE also incorporates proprioceptive sensing and advanced software algorithms for autonomous navigation, retroflexion, and diagnostic/therapeutic tasks. Particularly noteworthy is the MFE's autonomous capability in colonoscopy, mainly aimed at polyp detection. This cutting-edge technology promises to revolutionize endoscopy by improving maneuverability, reducing patient discomfort, and enhancing diagnostic accuracy.

1.3 Review of robotic endoscopic capsule localization strategies

Accurate estimation of the capsule's pose is crucial for magnetic actuation systems to effectively apply the required forces and torques. For this reason, it is essential to implement a localization algorithm to estimate the pose of the endoscope.

In this section, different magnetic localization methodologies are analyzed (see Figure 1.4).

Hu et al. [10] designed a real-time cubic magnetic sensor array for tracking a permanent magnet (see Figure 1.4.a). The Honeywell AMR 3-axis sensors, HMC1043, precision amplifiers, ADCs, and computer make up the system. The software (using Visual ++) completes the signal processing and all necessary operations on the sensing data based on the calibrations applied for the sensor sensitivity, position, and orientation, and computes the magnet 6-D position and orientation parameters via suitable algorithm.

Hu et al. [11] designed a magnetic localization system for the purpose of tracing intra-body capsule objects (see Figure 1.4.b). In this system, the source magnetic field is created by a ring magnet surrounding the capsule, and the reference objects, two magnets, are fastened to the surface of the human body. A suitable algorithm is used to analyse the sensing data obtained from a magnetic sensor array composed of 32 triaxial magnetic sensors to estimate the position and orientation characteristics of these three magnets.

Plotkin et al. [12] designed a multicoils electromagnetic tracking system (see Figure 1.4.c). They specifically created a novel method that enables the calibration of the whole magnetic tracking system at a single setting. The new method reduces the number of individual calibrations, streamlines the calibration process, and improves calibration accuracy.

Turan et al. [13] created a robust deep learning-based localization system with 6 degrees-of-freedom (DoF) for endoscopic capsule robots (see Figure 1.4.d). The primary focus of the system is to precisely locate endoscopic capsule robots within the GI tract, utilizing solely visual information captured by a mono camera integrated into the robot. The proposed solution revolves around a 23-layer deep convolutional neural network (CNN) designed to estimate the robot's pose in real-time. Remarkably, this advanced neural network achieves its capabilities using just a standard CPU, offering efficient and accurate localization for endoscopic capsule robotics.

In Figure 1.4.e it is possible to see the system developed by Taddese et al. [14], which will be presented in detail in the next chapter.

Popek et al. [16] present a novel and noniterative approach for accurately determining the six degrees-of-freedom (6-DOF) position and orientation of a wireless

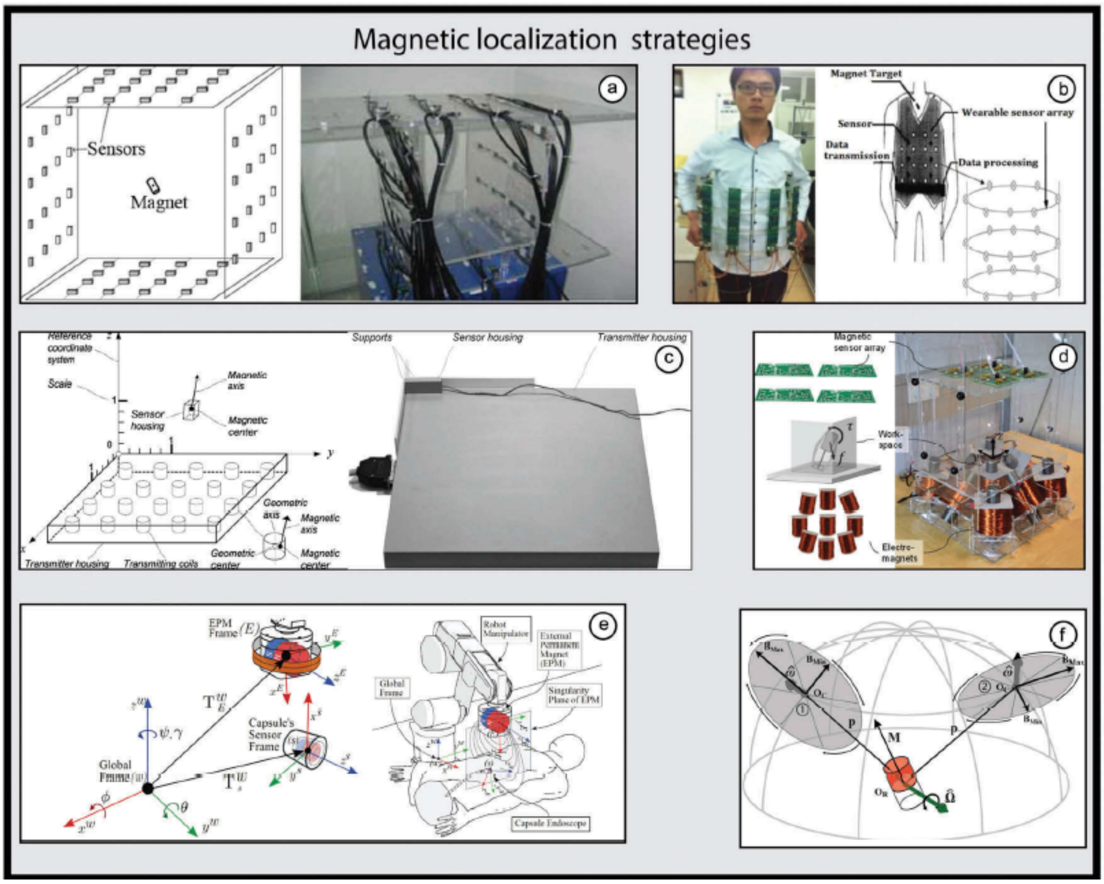

Figure 1.4: Examples of magnetic-based localization systems [15]. (a) Hu et al. [10], scheme and cubic magnetic array of sensors; (b) Hu et al. [11], wearable magnetic localization array of sensors; (c) Plotkin et al. [12], multicoils electromagnetic tracking system; (d) Turan et al. [13], electromagnetic locomotion and sensors array localization system; (e) Taddese et al. [14], application scenario of active magnetic manipulation of a capsule endoscope using a permanent magnet mounted at the end-effector of a robot manipulator; (f) Popek et al. [16], modelling principle.

capsule endoscope, which is actuated by a rotating magnetic dipole (see Figure 1.4.f). Through extensive experimentation, they demonstrate the effectiveness of their algorithm in calculating the 6-DOF position and orientation for capsules that remain stationary and those operated in the "step-out" regime. In the latter scenario, where the magnetic field rotation exceeds the capsule's synchronous rotation capability, the capsule exhibits chaotic movement. Despite these challenges, their solution proves to be robust and reliable.

These are just a few examples of magnetic localization. In the next chapter, the system developed by Taddese et al [14] will be introduced, as it represents the starting point of the entire work.

Chapter 2

Motivation and Context

In this chapter, the Magnetic Flexible Endoscopy (MFE) system will be thoroughly explained, and the localization algorithm implemented at the STORM Lab for estimating the endoscope's pose will be elucidated. Lastly, the reasons driving the development of a new localization algorithm will be presented, and so the state-of-the-art estimation algorithms for localization that can be used are shown.

2.1 Magnetic Flexible Endoscopy system

The STORM Lab team is currently in the process of developing an innovative Magnetic Flexible Endoscopy (MFE) system. This advanced system is envisioned to play a pivotal role in clinical investigations and research studies pertaining to the navigation and examination of the human colon, specifically in the context of colonoscopy. Conventional colonoscopy procedures utilizing a standard flexible endoscope have long been associated with challenges for the operator and discomfort for the patient. The intricacies of standard colonoscopy often necessitate sedation, leading to suboptimal patient adherence to screening protocols. The MFE system has been meticulously designed to supplant the conventional colonoscopy approach, with the potential to address and enhance the prevailing limitations. By doing so, it holds the promise of substantially improving patient well-being and longevity. This transformative technology could pave the way for enhanced procedure accessibility, heightened patient compliance with screening regimens, mitigated risks of colonic tissue trauma, and ultimately, a more efficacious diagnosis and management of colorectal ailments. The whole system is depicted in Figure 2.1.

The MFE comprises four primary hardware subsystems: an external robotic system serving as an actuation source situated adjacent to the patient, a tethered endoscopic capsule featuring a diverse array of sensors designed to navigate through the gastrointestinal (GI) tract via magnetic coupling, a processing unit, and a

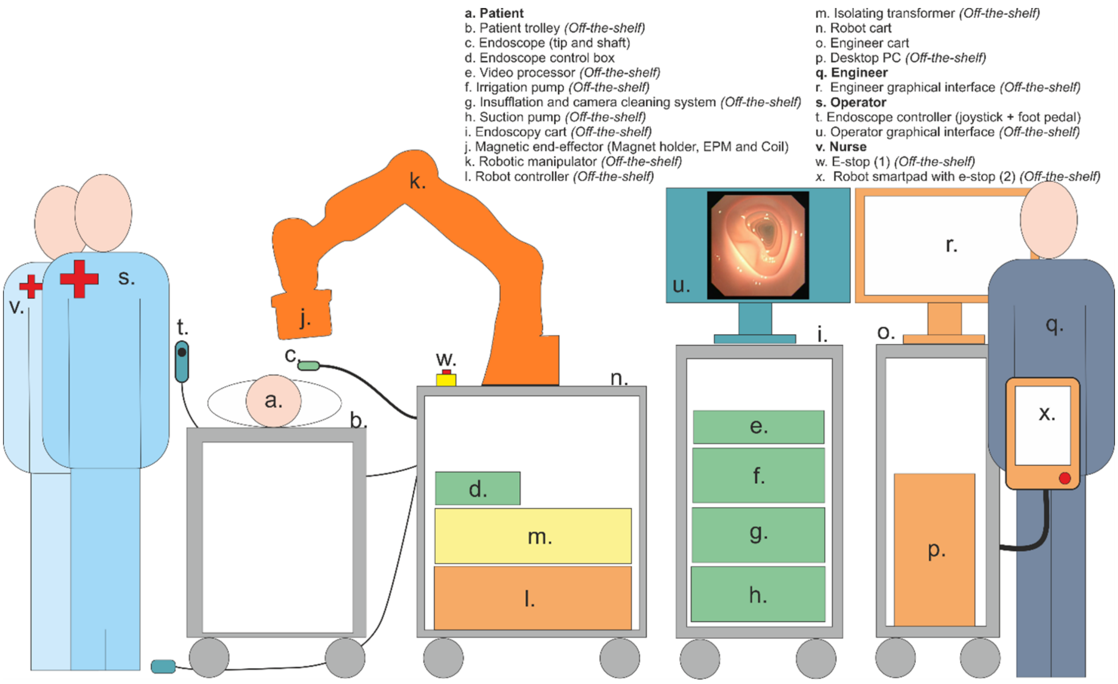

Figure 2.1: Overview of the MFE system (source: STORM Lab UK).

dedicated circuit facilitating seamless communication between the capsule and the MFE software.

The robotic system comprises a 7-axis collaborative robotic manipulator meticulously crafted for medical purposes by KUKA. This manipulator offers dual modes of operation: direct control by the physician through a specialized joystick interface or autonomous execution of pre-defined paths through programming. At its end effector, a custom-designed magnetic system is integrated, facilitating precise localization and proficient actuation functionalities. In essence, this magnetic system encompasses:

- A neodymium iron boron (NdFeB) cylindrical permanent magnet with axial magnetization and remanence of 1.48 T. This potent magnet is securely housed within a precisely crafted 3D printed enclosure. This magnet functions as the primary actuation source, exerting a compelling magnetic field that propels the capsule along its designated trajectory. The magnet imparts a propulsive force, maintaining alignment with the capsule's movement, provided that the distance from the endoscopic tip remains within an optimal range. As this distance increases, the magnetic force between the External Permanent Magnet (EPM) and Internal Permanent Magnet (IPM) within the capsule diminishes.

- An electromagnetic coil, that is constructed using 24 AWG ($R_{int} = 7\Omega$) wire, meticulously wound into 160 turns arranged across 2 interlocking layers. This coil, with a diameter of 180 mm and a length of 40 mm, is ingeniously secured within a supplementary 3D printed framework for optimal stability and precision.

Figure 2.2 shows the cylindrical external permanent magnet and the electromagnetic coil.

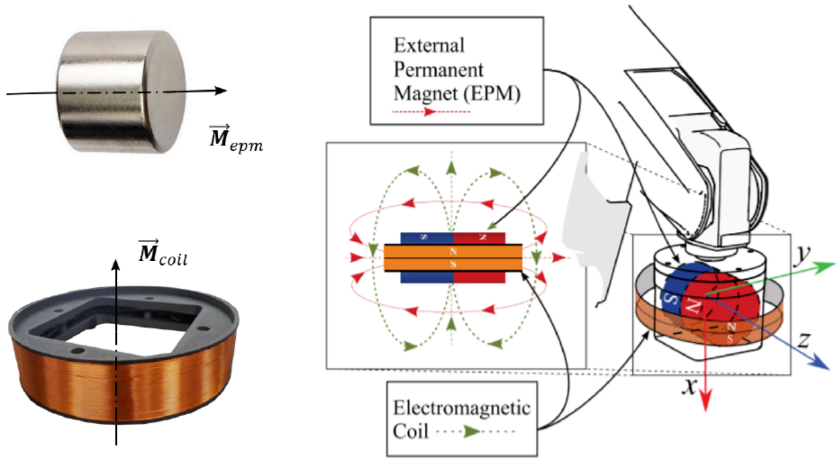

Figure 2.2: Representation of EPM and coil [5].

Transitioning to the endoscopic tip, which boasts dimensions of 20 mm in diameter and 22 mm in length, it is outfitted with a soft tether that not only accommodates conventional endoscopic practices but also orchestrates the seamless exchange of data between the embedded sensors and the processing unit. The capsule's design encompasses an array of essential components, including a camera for precise vision, an integrated water nozzle that adeptly irrigates the inspection area and the camera lens concurrently, a strategically positioned LED to provide illuminating clarity, and a dedicated instrument channel that empowers proficient execution of biopsy procedures.

Given the reliance on magnetic direct propulsion for the application, the capsule itself is ingeniously outfitted with a small, axially magnetized cylindrical NdFeB permanent magnet, the Internal Permanent Magnet (IPM), boasting a remanence of 1.48 T. The IPM's spatial context is carefully considered, surrounded by six Hall effect sensors meticulously positioned to effectively emulate the presence of two triaxial Hall sensors, thoughtfully spaced at a consistent interval. The sensors are placed in order to prevent saturation due to the IPM magnetic field. Importantly, it is imperative to note that any potential biases introduced by the IPM are subsequently rectified from the magnetic field measurements. This process ensures the precise detection of B_{EPM} and B_{coil}, consequently contributing to accurate and uncompromised results. Furthermore, a 6-DOF Inertial Measurement Unit (IMU) is integrated inside the capsule. This IMU boasts a 3D digital accelerometer, engineered to accommodate a wide-ranging full-scale acceleration spectrum of up to ±16 g, alongside a 3D digital gyroscope with an angular rate capacity reaching up to ±2000 degrees per second. This sophisticated sensor configuration delivers invaluable data concerning linear accelerations and angular velocities, critically contributing to the capsule's precise localization. While the IMU yields digital values, readily available for computational processes, the output from the six Hall effect sensors operates within the analog domain. To bridge this technological divide and facilitate digital conversion, a 16-bit Analog-to-Digital Converter (ADC) has been incorporated into the application's architecture. The architecture of the endoscope is shown in the Figure 2.3.

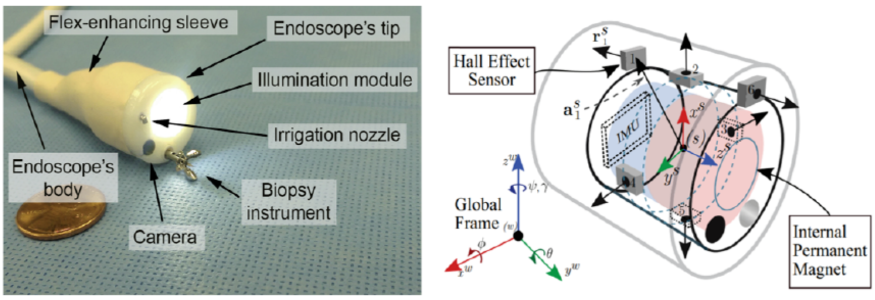

Figure 2.3: Endoscope architecture [5].

In conclusion, in the hardware architecture of the MFE there is also an electronic circuit, composed of a STM Nucleo development board and of a driver circuit. This integrated circuitry serves a multi-fold purpose: orchestrating the signal processing techniques utilizing the data harnessed from the Hall effect sensors and IMU; subsequent to processing, channeling this data via a USB cable to the processing unit, where they are used in ROS for precise magnetic localization; and finally, generating the essential square wave signal for the oscillating magnetic field of the coil. The block diagram of the MFE is shown in Figure 2.4.

2.2 Localization algorithm

The localization subsystem within the MFE has a precise objective: to calculate both the position and orientation of the endoscope tip relative to a fixed reference frame positioned at the center of the robot base. Among the various subsystems of the MFE, the localization process stands out as the most intricate. It is composed

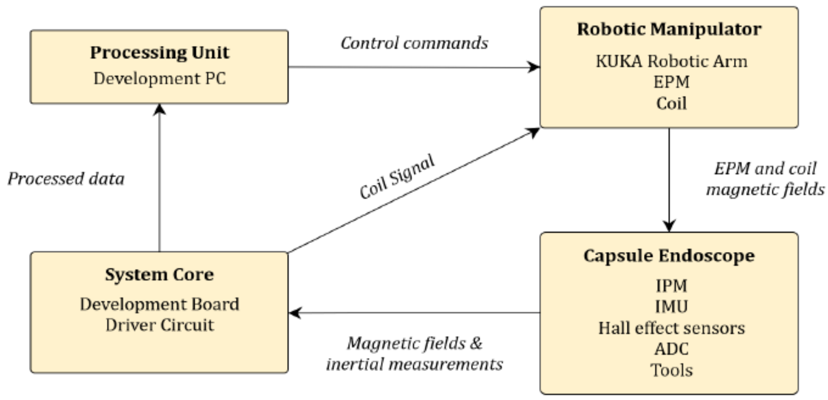

Figure 2.4: Block diagram of the MFE [5].

of a significant number of elements. In essence, its core concept revolves around harnessing the magnetic field generated by the EPM. This magnetic field serves as a foundation for determining the endoscope's pose with respect to the EPM. Subsequently, the robot kinematic is used to localize the endoscope with respect to a fixed frame. However, practical implementation introduces several intricate challenges:

- the orientation of the endoscope is required as well;
- the localization process must exhibit robustness in the face of spikes and disturbances;
- the field generated by the EPM has a plane of singularity, in which the field has the same magnitude in an infinite number of points (see Figure 2.5). In fact, in the plane passing through the center of the EPM, the field assumes the same values for every point at a given distance from the center;
- the localization process must generate results at a frequency sufficient to enable effective closed-loop control of the endoscope's movements.

In the realm of pose estimation, Di Natali et al. [17] crafted an ingenious algorithm capitalizing on the axial symmetry inherent in cylindrical magnets. This innovative approach facilitated the establishment of a real-time 6-DOF pose estimation system. Subsequently, they introduced an even more computationally efficient iterative algorithm in a later work [18], outpacing an update rate exceeding 100 Hz.

A comprehensive examination of the workspace of the real-time pose estimation methods mentioned earlier [17] [18] reveals the presence of singularities within specific regions of the workspace, which consequently result in the deterioration of

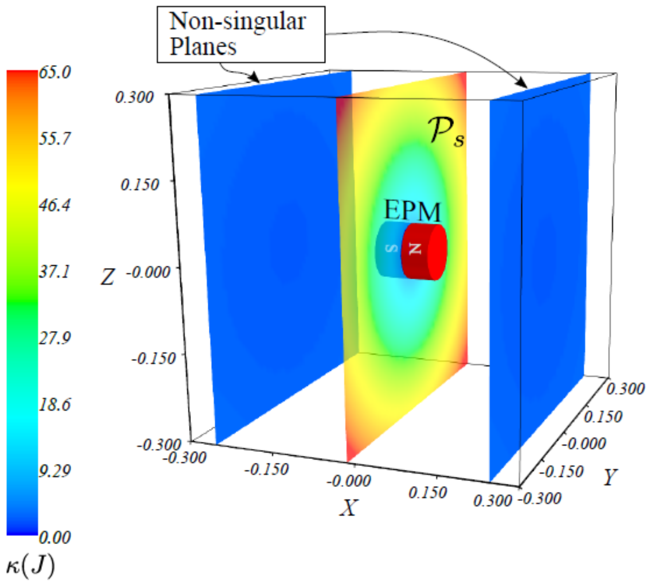

Figure 2.5: Regions of magnetic field singularity as indicated by high condition numbers of the Jacobian matrix [14].

estimation capability. These algorithms are predicated on the assumption that a bijective mapping exists between all workspace positions and magnetic field vectors for a given configuration of the EPM. Due to this, it is posited that alterations in the magnetic field consistently correspond to changes in position. However, this foundational assumption is debunked by Taddese et al. [14], particularly in the context of the singularity plane of the EPM. This plane is the plane normal to the dipole moment and intersects the magnet's center (see Figure 2.5). In various instances of robotically guided magnetic capsule endoscopy, it is imperative for the capsule to maintain a nominal position within this specific region throughout clinical procedures. Regrettably, this constraint serves as a hindrance to the prospective clinical deployment of these devices. Taddese et al. [14] pioneer a groundbreaking hybrid system that ingeniously merges static and time-varying magnetic field sources. This innovative approach culminates in a magnetic pose estimation method for robotically guided magnetic capsule endoscopy that is not only robust but also holds significant promise for clinical viability. The system consisting of EPM and coil was presented earlier in this chapter and is depicted in Figure 2.2.

2.2.1 Hybrid magnetic field

Enhancing the system involves the integration of an electromagnetic coil strategically designed to produce a weak time-varying magnetic field. This coil is affixed to the EPM in a configuration that ensures the orthogonal alignment of their respective dipole moments. This ingeniously orchestrated synergy between the EPM's static field and the coil's evolving magnetic field facilitates the simultaneous derivation of an extra set of equations. This augmented framework, as demonstrated by Taddese et al. [14], empowers the solution for the capsule's position and yaw angle. The strategic juxtaposition of the EPM and the electromagnetic coil ensures that within the singularity region of the EPM, the magnetic field generated by the coil consistently maintains orthogonality to the EPM's magnetic field. Contrastingly, if the coil were stationed at a fixed position, such as being embedded within the surgical table, the magnetic fields of the EPM and the coil could potentially align during magnetic manipulation. In the event of such alignment within the EPM's singularity region, the number of available equations for solving the inverse problem would be diminished. Consequently, the challenge posed by the singularity issue would persist unabated.

Within a defined workspace, the dynamic magnetic field is calibrated to achieve detectability by the magnetic field sensors within the capsule, all while avoiding the imposition of sufficient force and torque to induce physical perturbations in the capsule's pose. A time-varying signal is employed to distinctly measure the magnetic fields emanating from both the EPM and the coil. This approach stands in stark contrast to the utilization of two static magnetic fields, which, due to the principle of superposition governing their interaction, would preclude the ability to make separate measurements; two static magnetic fields would also lead to a reduction in the count of available equations, thereby diminishing the overall effectiveness of the approach.

The application of Goertzel's tone detection algorithm [19] [20] serves as the conduit for extracting both the magnitude and phase information of the time-varying signal acquired for each sensor. These extracted values are seamlessly compiled into a vector, thereby enabling to seamlessly treat the coil as an additional permanent magnet positioned at the identical origin as the EPM.

Taddese et al. [14] rigorously scrutinize the algebraic equations inherent to the hybrid system, with the primary objective of ascertaining the presence of any singularities that could potentially lead to an infinite array of solutions in the inverse problem of finding the pose given magnetic field measurements. Interestingly, this analysis compellingly demonstrates that the introduction of an orthogonal supplementary magnet furnishes an adequate amount of information. This newly acquired information effectively empowers a nonlinear solver to attain a unique solution.

In the majority of instances, the system presents an over-determined configuration, facilitating the resolution of unknown variables. Nevertheless, owing to the inherent symmetry of magnetic fields, the system of equations can yield multiple solutions, but always in finite number. These multiple solutions are distinctly situated in separate and non-overlapping sectors of the workspace, thereby permitting the selection of an appropriate solution based on the capsule's previous poses.

2.2.2 Main components of the algorithm

Localization inputs and outputs

The internal sensors of the endoscope, previously described, allow to have the following data as inputs to the localization algorithm:

- linear acceleration of the endoscope on three axes;
- angular velocities of the endoscope on three axes;
- magnetic field values perceived by the endoscope on three axes.

The six Hall effect sensors are strategically oriented to provide dual readings for each principal axis within the endoscope's local reference frame.

The robot establishes a connection to the control system through ROS, periodically publishing the pose (comprising position and orientation) of the end effector with respect to the robot's base.

The localization output is a ROS topic encompassing the endoscope's pose. This topic encompasses the following elements:

- endoscope position relative to the robot base;
- endoscope orientation relative to the robot base.

Estimation of roll and pitch

In applications featuring a floating device endowed with 6-DOF, the orientation determination of said object typically involves a fusion of inertial measurements and sensing the Earth's magnetic field, a field known for its established orientation. This approach stems from the inherent influence of roll and pitch angles on inertial measurements (reflecting the direction of gravity), while remaining unaffected by the yaw angle [21]. To accurately compute the yaw angle, the Earth's magnetic field is routinely leveraged. This essential computation is complemented by the gyro's contributions, encapsulating the angular velocities around all three axes.

The problem has nine inputs and three outputs. For a dependable orientation calculation, the Mahoney filter [22] stands out as the prevailing approach. This filtering technique revolves around a PI feedback loop, seamlessly assimilating the data originating from both the IMU and the magnetic field sensors. The outcome is a consistently stable output. A visual representation of the Mahoney filter is presented in Figure 2.6.

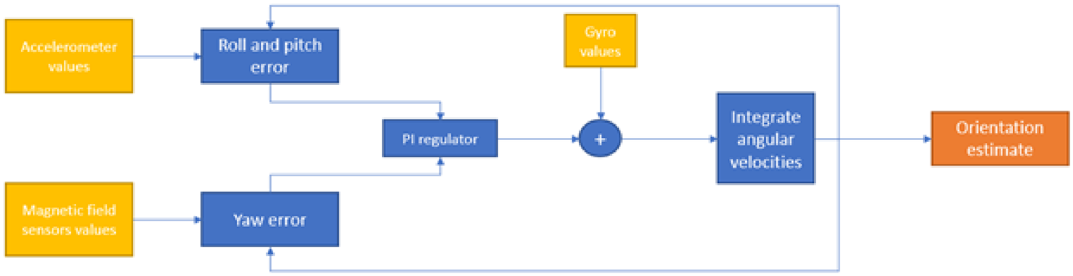

Figure 2.6: Block diagram of the Mahoney filter (source: STORM Lab UK).

In the context of the MFE, the utilization of Earth's magnetic field for yaw computation is rendered unfeasible because the field generated by the EPM is several orders of magnitude bigger. Consequently, a customized iteration of the Mahony filter is embraced, one that takes into account the EPM's orientation to effectively address this challenge.

The Mahoney filter yields the following outputs:

- a dependable estimation of roll and pitch angles;
- an initial approximation of the yaw angle, which serves as a starting point for the subsequent stage.

Estimation of position and yaw

The preceding stage furnishes two out of the six state variables necessary for endoscope localization. The remaining quartet of states awaiting determination comprise position (x, y, and z) relative to the robot base, along with the yaw angle. The Goertzel filter is able to efficiently compute the magnitude and phase of the two magnetic fields. Thanks to this, there are six inputs to the localization problem: $[x_{EPM}, y_{EPM}, z_{EPM}]$ and $[x_{coil}, y_{coil}, z_{coil}]$, which are the magnetic field values of the EPM and of the coil.

Endoscope localization is executed through the utilization of a Particle Filter (PF), a statistical tool proficient in the estimation of a system's states by absorbing observations over time. This approach is often used in estimation problems in which the process has statistical characteristics and the measures dominate the system, in contrast to Kalman filters that prioritize system dynamics. Central to the PF is a set of particles, constituting a particle cloud, wherein each particle encapsulates a state vector and corresponds to a specific likelihood. With each input measurement, both state and likelihood are subjected to updates. The particle distribution can be weighted based on their respective likelihoods, or alternatively, the particle with the highest likelihood may be selected as the output. In the context of the MFE, a subset of particles surpassing a predetermined likelihood threshold is considered. The outcome of the localization process is derived from this subset, specifically by calculating the average value within it.

For assimilating the data, the PF necessitates a model of the magnetic field produced by a cylindrical magnet characterized by a specified magnetic moment, a parameter that is established for both the EPM and the coil. While the magnetic dipole model is conventionally employed to calculate forces and torques exerted on the endoscope, its accuracy falls short in meeting the required performance benchmarks, particularly when dealing with close inter-magnetic distances. Consequently, the generalized complete elliptic integral model is adopted. This model is chosen due to its superior ability to furnish accurate results, particularly in scenarios featuring tight magnetic proximity. To expedite the identification process, the model is employed to construct a comprehensive map of the fields generated by both the EPM and the coil. This mapping exercise covers a quarter of the workspace, encompassing distances up to 30 cm. Subsequently, searches are conducted within this map. In cases where the PF necessitates computations beyond the scope of the pre-computed workspace, the integral is explicitly solved.

In the subsequent paragraph the results obtained by Taddese et al. [14] for the just-presented localization algorithm are presented.

2.2.3 Results obtained with the PF algorithm

Taddese et al. [14] rigorously assessed the pose estimation algorithm through a comprehensive experimental validation encompassing both static and dynamic scenarios. In the static condition tests, precise poses were meticulously set for both the capsule and the EPM. This setup facilitated the computation of average errors for each position, including those situated within the singular regions of the EPM and the coil. In the dynamic tests, the evaluation extended to deliberate movements of either the capsule or the EPM at predefined velocities, aimed at elucidating trajectory errors.

Validation in static conditions

The capsule was carefully situated within a 3D printed housing and firmly affixed to the secondary robot manipulator. This manipulator was intentionally positioned in a precisely known pose relative to the primary robot. In the initial series of static tests, the EPM underwent a spiral trajectory, tracing the surface of a hemisphere while maintaining a consistent distance from the capsule (see Figure 2.7). This encompassed six distinct tests, each involving hemispheres with varying radii ranging from 150 mm to 200 mm. The decision to cap the maximum radius at 200 mm was a deliberate measure, ensuring the tests remained confined to regions characterized by clinically relevant forces and torques applied to the capsule.

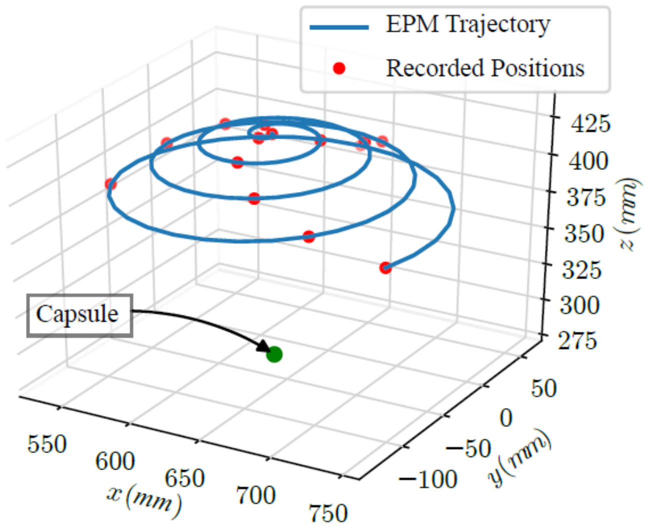

Figure 2.7: Static validation experiments: spiral trajectory. The red dots are the positions where the EPM was stopped [14].

The results of the experiment are shown in Figure 2.8.

Radius of hemisphere (mm)	Δx (mm)	Δy (mm)	Δz (mm)	$\Delta\phi$ (°)	$\Delta\theta$ (°)	$\Delta\psi$ (°)
150	1.04 ± 1.42	3.67 ± 1.63	2.87 ± 1.05	0.93 ± 0.67	-0.95 ± 1.03	-4.73 ± 0.31
160	1.39 ± 1.42	3.81 ± 1.62	2.65 ± 1.00	1.00 ± 0.62	-1.05 ± 0.88	-5.06 ± 0.25
170	1.42 ± 1.39	3.97 ± 1.66	2.41 ± 0.92	1.00 ± 0.61	-1.09 ± 0.67	-5.62 ± 0.16
180	1.71 ± 1.42	4.19 ± 1.69	2.15 ± 0.94	1.02 ± 0.59	-0.86 ± 0.57	-5.62 ± 0.14
190	1.87 ± 1.40	4.32 ± 1.72	1.80 ± 0.91	1.05 ± 0.54	-0.84 ± 0.43	-5.65 ± 0.11
200	1.97 ± 1.38	4.35 ± 1.71	1.55 ± 0.88	1.11 ± 0.50	-0.84 ± 0.33	-5.66 ± 0.09

Figure 2.8: Mean error and its standard deviation of pose estimates for static tests along a spiral trajectory [14].

A larger positional error was encountered along the y-axis, potentially attributed to the fact that the capsule was in the singularity region of the EPM for a subset of the 25 points on the hemisphere. This occurrence led to a reduction in the count of constraining equations responsible for mapping poses to magnetic field vectors. Given that the singularity plane of the EPM in this specific set of trials corresponded to the yz-plane, it is reasonable to anticipate larger errors along the y-axis. Furthermore, the error in the yaw angle surpasses that of the other orientation angles. This phenomenon can be attributed to the yaw being uniquely susceptible to the bias and noise characteristics inherent in the magnetic field sources. In contrast, the remaining two angles were derived from accelerometer measurements.

Validation in dynamic conditions

Validation under dynamic conditions involved the execution of two distinct experiment types. The first, termed the static-dynamic experiment, involved exclusively mobilizing the capsule along a designated trajectory, while the EPM remained stationary. Conversely, the second, termed the dynamic-dynamic experiment (see Figure 2.9), entailed simultaneous movement of both the capsule and the EPM along an identical trajectory while maintaining a consistent relative velocity. In both experiment types, the trajectory was meticulously devised to closely emulate the characteristic curvature of the human colon. Additionally, to establish a baseline of accurate measurements, a secondary robot manipulator was employed. This secondary manipulator was responsible for securely holding and orchestrating the movement of the capsule along the predetermined trajectory, thereby providing reliable ground truth data for comparison.

The results obtained in the two tests are shown in Figures 2.10 and 2.11. Both figures show the excellent results achieved by the localization algorithm.

2.3 Reasoning behind the necessity for a new localization algorithm

The localization algorithm implemented by Taddese et al. [14] yielded excellent results. However, the PF lacks covariance matrices that enable real-time determination of localization accuracy. Hence, a primary objective of this thesis work is to identify specific parameters that facilitate real-time evaluation of localization correctness.

Furthermore, even though the average errors found are minimal, sporadic instances of drift do arise, where the estimated pose from the localization algorithm diverges from the true pose. As a response to this challenge, a parallel effort has been initiated to develop an alternative localization algorithm. The overarching objective is to harness the strengths of both the PF and the new algorithm, amalgamating their respective positive attributes. This strategic fusion is envisioned to yield an algorithm of enhanced reliability and robustness.

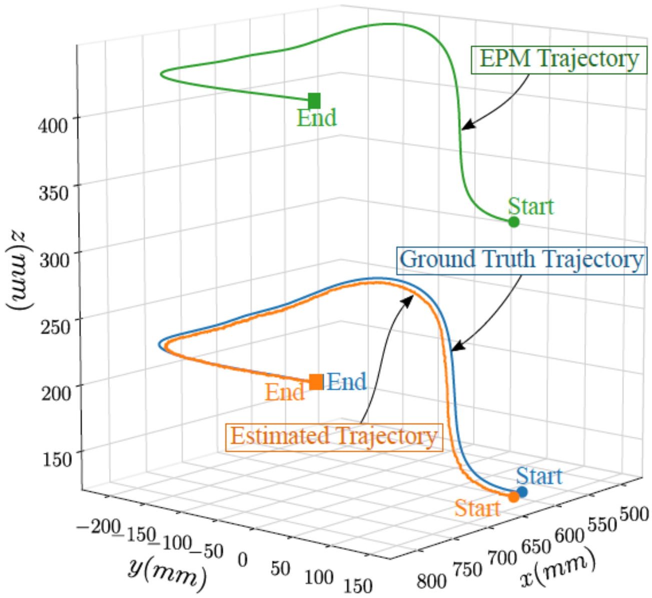

Figure 2.9: Dynamic-dynamic test: plot of the trajectories of the EPM and the capsule (10 mm/s) [14].

Speed (mm/s)	Δx (mm)	Δy (mm)	Δz (mm)	$\Delta\phi$ (°)	$\Delta\theta$ (°)	$\Delta\psi$ (°)
10	-3.39 ± 6.76	-4.84 ± 5.23	4.06 ± 1.91	-0.96 ± 2.30	0.29 ± 1.73	-0.37 ± 2.84
25	-1.98 ± 7.70	-5.07 ± 5.67	4.49 ± 1.92	-1.75 ± 1.88	0.08 ± 1.55	-0.20 ± 2.79
50	0.70 ± 12.05	-3.33 ± 10.01	4.79 ± 2.74	-3.10 ± 2.14	-1.65 ± 3.44	-0.13 ± 2.69

Figure 2.10: Mean error and its standard deviation of pose estimates for static-dynamic tests [14].

2.4 Estimation algorithms for localization - state of the art

Localization is the main focus of the thesis project. The MFE's localization subsystem acts to determine the endoscope tip's position and orientation with respect to a fixed reference frame (RF) positioned in the middle of the robot base. Figure 2.12 shows the global RF.

To gain a comprehensive understanding of the most suitable algorithm for accurately estimating the system's state (position and orientation), a thorough theoretical analysis of multiple algorithms is essential. Considering that there are no linear Gaussian systems in the real world, and our system is not either, algorithms based on nonlinear, non-Gaussian (NLNG) estimation must be analyzed.

Speed (mm/s)	Δx (mm)	Δy (mm)	Δz (mm)	$\Delta\phi$ (°)	$\Delta\theta$ (°)	$\Delta\psi$ (°)
10	-2.05 ± 5.00	-1.60 ± 3.76	1.60 ± 0.57	-1.76 ± 1.15	0.07 ± 1.80	-0.27 ± 2.65
25	-1.39 ± 5.56	-1.50 ± 3.95	1.35 ± 0.65	-2.14 ± 1.45	-0.09 ± 1.96	-0.17 ± 2.60
50	-2.59 ± 5.44	-1.77 ± 5.63	1.16 ± 0.75	-3.01 ± 2.00	-1.44 ± 3.76	-0.08 ± 2.68

Figure 2.11: Mean error and its standard deviation of pose estimates for dynamic-dynamic tests [14].

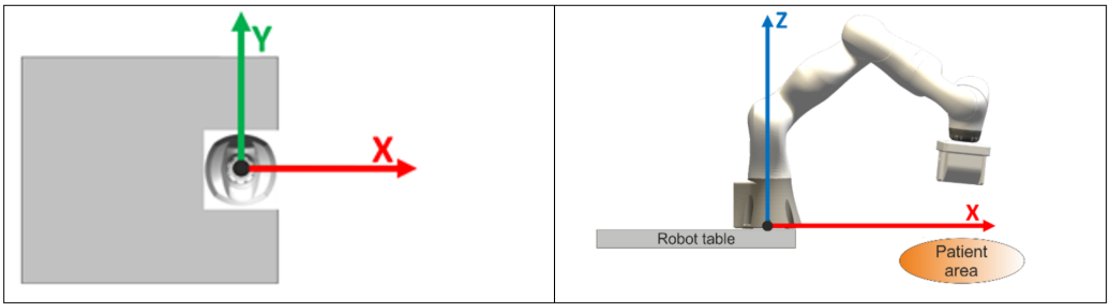

Figure 2.12: The global RF.

Three estimators for non-linear systems will be analyzed in this section:

- Particle Filter.
- Extended Kalman Filter.
- Unscented Kalman Filter.

The following notation will be used to ensure clarity and consistency in discussing the various concepts and elements:

- Normal letters (a, b, c, ...) denote scalars, bold ($\mathbf{a}$, $\mathbf{b}$, $\mathbf{c}$, ...) denote vectors, and uppercase (A, B, C, ...) denotes matrices.
- Subscripts (x_a) denote discrete time.
- Conditional subscripts ($x_{a|b}$) denote the variable x at time a, given measurements up to time b.
- Letters with a hat ($\hat{a}$, $\hat{b}$, $\hat{c}$, ...) are estimated values affected by a certain degree of uncertainty.
- Letter k identifies the discrete time instant at which that variable is evaluated.

2.4.1 Particle Filter

The Particle Filter (PF) is the algorithm currently used for localization and will be analyzed in this section from a theoretical point of view.

PF, also known as Sequential Monte Carlo methods (SMC), represents a class of recursive Bayesian state estimation techniques that find frequent application in object tracking and localization tasks. In the PF, the posterior distribution, $p(\mathbf{x}_k|\mathbf{z}_{1:k})$, of the state $\mathbf{x}_k$ at time k conditioned on a time series of measurement $\mathbf{z}_{1:k} = \{z_i, i = 1,2, ..., k\}$ is represented by a set of particles, which are assigned a weight, w_k^i.

PF is able to overcome limiting assumptions made by other state estimation techniques, such as Kalman Filters, where process and measurement models are linear, and noise distributions are Gaussian. This is due to to the nonparametric representation of the probability density function (PDF) and the use of Monte Carlo techniques [9].

PF Algorithm

The following are the main phases of the PF [23].

1. Draw M samples from the joint density comprising the prior and the motion noise:
$$\begin{bmatrix} \hat{\mathbf{x}}_{k-1,m} \\ \mathbf{w}_{k,m} \end{bmatrix} \leftarrow p(\mathbf{x}_{k-1}|\hat{\mathbf{x}}_0, \mathbf{v}_{1:k-1}, \mathbf{y}_{1:k-1})p(\mathbf{w}_k), \tag{2.1}$$
where $\mathbf{v}$ is the prior information, $\mathbf{y}$ are the measurements, $\mathbf{x}$ is the state, $\mathbf{w}$ is the weight associated with the particle m.

2. Prediction phase: generate a prediction of the posterior PDF using $\mathbf{v}_k$, and the nonlinear motion model:
$$\hat{\mathbf{x}}_{k,m} = f(\hat{\mathbf{x}}_{k-1,m}, \mathbf{v}_k, \mathbf{w}_{k,m}). \tag{2.2}$$
All the predicted particles together approximate the density:
$$p(\mathbf{x}_k|\hat{\mathbf{x}}_0, \mathbf{v}_{1:k}, \mathbf{y}_{1:k-1}). \tag{2.3}$$

3. Correction phase: correct the posterior PDF using the measurements $\mathbf{y}_k$. Two steps must be followed in this phase:
   - Assign a weight to each particle based on the divergence between the desired posterior and the predicted posterior for each particle:
$$\mathbf{w}_{k,m} = \frac{p(\hat{\mathbf{x}}_{k,m}|\hat{\mathbf{x}}_0, \mathbf{v}_{1:k}, \mathbf{y}_{1:k})}{p(\hat{\mathbf{x}}_{k,m}|\hat{\mathbf{x}}_0, \mathbf{v}_{1:k}, \mathbf{y}_{1:k-1})} = \eta p(\mathbf{y}_k|\hat{\mathbf{x}}_{k,m}), \tag{2.4}$$

where η is a normalization constant. This is typically done by simulating an expected sensor reading using the nonlinear observation model:

$$\hat{\mathbf{y}}_{k,m} = g(\hat{\mathbf{x}}_{k,m}, 0). \tag{2.5}$$

It is therefore assumed $p(\mathbf{y}_k|\hat{\mathbf{x}}_{k,m}) = p(\mathbf{y}_k|\hat{\mathbf{y}}_{k,m})$, where the right-hand side is a known density.

- Resample the posterior based on the weight assigned to each predicted posterior particle:

$$\hat{\mathbf{x}}_{k,m} \xleftarrow{\text{resample}} \{\hat{\mathbf{x}}_{k,m}, \mathbf{w}_{k,m}\}. \tag{2.6}$$

One of the aims of the thesis project is to implement a new localization algorithm, so two other methods are discussed in the following sections.

2.4.2 Extended Kalman Filter

The Extended Kalman Filter (EKF) continues to hold its ground as a prevalent choice for estimation and data fusion in various domains, proving particularly effective for systems with moderate nonlinearity and non-Gaussian characteristics.

EKF Algorithm

First of all, it is necessary to limit the belief function for $\mathbf{x}_k$ to be Gaussian [23]:

$$p(\mathbf{x}_k|\hat{\mathbf{x}}_0, \mathbf{v}_{1:k}, \mathbf{y}_{0:k}) = \mathcal{N}(\hat{\mathbf{x}}_k, \hat{P}_k), \tag{2.7}$$

where $\hat{\mathbf{x}}_k$ and $\hat{P}_k$ are respectively the mean and the covariance. Then, it is assumed that the noise variables $\mathbf{w}_k$ and $\mathbf{n}_k$ ($\forall k$) are Gaussian as well:

$$\mathbf{w}_k \sim \mathcal{N}(0, Q_k), \tag{2.8}$$

$$\mathbf{n}_k \sim \mathcal{N}(0, R_k). \tag{2.9}$$

The state and measurement equations are the following:

$$\mathbf{x}_k = f(\mathbf{x}_{k-1}, \mathbf{v}_k) + \mathbf{w}_k, \tag{2.10}$$

$$\mathbf{y}_k = g(\mathbf{x}_k) + \mathbf{n}_k. \tag{2.11}$$

Considering that the functions $f(\cdot)$ and $g(\cdot)$ are nonlinear, it is not possible to compute the integral in the Bayes filter in closed form, so it is necessary to linearized:

$$f(\mathbf{x}_{k-1}, \mathbf{v}_k, \mathbf{w}_k) \approx \hat{\mathbf{x}}_k + F_{k-1}(\mathbf{x}_{k-1} - \hat{\mathbf{x}}_{k-1}) + \mathbf{w}'_k, \tag{2.12}$$

$$g(\mathbf{x}_k, \mathbf{n}_k) \approx \hat{\mathbf{y}}_k + G_k(\mathbf{x}_k - \hat{\mathbf{x}}_k) + \mathbf{n}'_k, \tag{2.13}$$

where, for the state:

$$\hat{\mathbf{x}}_k = f(\hat{\mathbf{x}}_{k-1}, \mathbf{v}_k, 0), \tag{2.14}$$

$$F_{k-1} = \left.\frac{\partial f(\mathbf{x}_{k-1}, \mathbf{v}_k, \mathbf{w}_k)}{\partial \mathbf{x}_{k-1}}\right|_{\hat{\mathbf{x}}_{k-1}, \mathbf{v}_k, 0}, \tag{2.15}$$

$$\mathbf{w}'_k = \left.\frac{\partial f(\mathbf{x}_{k-1}, \mathbf{v}_k, \mathbf{w}_k)}{\partial \mathbf{w}_k}\right|_{\hat{\mathbf{x}}_{k-1}, \mathbf{v}_k, 0} \mathbf{w}_k, \tag{2.16}$$

and for the measurement:

$$\hat{\mathbf{y}}_k = g(\hat{\mathbf{x}}_k, 0), \tag{2.17}$$

$$G_k = \left.\frac{\partial g(\mathbf{x}_k, \mathbf{n}_k)}{\partial \mathbf{x}_k}\right|_{\hat{\mathbf{x}}_k, 0}, \tag{2.18}$$

$$\mathbf{n}'_k = \left.\frac{\partial g(\mathbf{x}_k, \mathbf{n}_k)}{\partial \mathbf{n}_k}\right|_{\hat{\mathbf{x}}_k, 0} \mathbf{n}_k. \tag{2.19}$$

The equations that describe the EKF are the following:

1. Prediction phase:

$$\hat{P}_k = F_{k-1}\hat{P}_{k-1}F_{k-1}^T + Q'_k, \tag{2.20}$$

$$\hat{\mathbf{x}}_k = f(\hat{\mathbf{x}}_{k-1}, \mathbf{v}_k, 0). \tag{2.21}$$

2. Kalman gain:

$$K_k = \hat{P}_k G_k^T (G_k \hat{P}_k G_k^T + R'_k)^{-1}. \tag{2.22}$$

3. Correction phase:

$$\hat{P}_k = (1 - K_k G_k)\hat{P}_k, \tag{2.23}$$

$$\hat{\mathbf{x}}_k = \hat{\mathbf{x}}_k + K_k(\mathbf{y}_k - g(\hat{\mathbf{x}}_k, 0)), \tag{2.24}$$

where

$$Q'_k = E[\mathbf{w}'_k \mathbf{w}'^T_k], \tag{2.25}$$

$$R'_k = E[\mathbf{n}'_k \mathbf{n}'^T_k]. \tag{2.26}$$

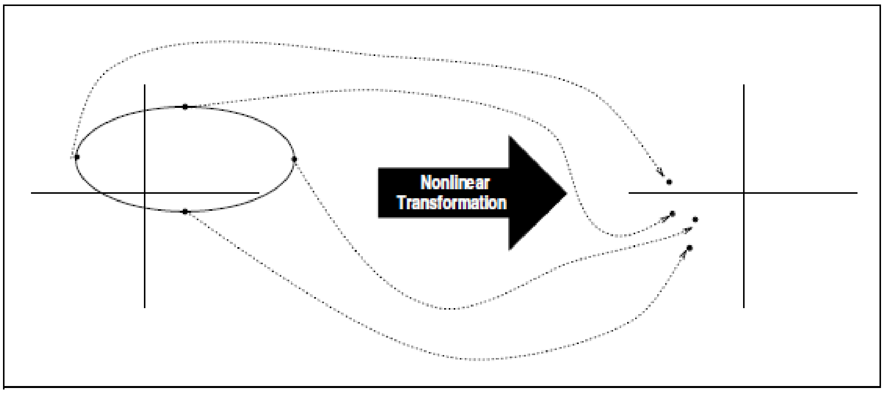

Figure 2.13: The unscented transform [24].

2.4.3 Unscented Kalman Filter

The unscented transformation presents a technique for computing the statistics of a random variable when subjected to a nonlinear transformation. This method is based on the insightful notion that approximating a Gaussian distribution is more feasible compared to approximating an arbitrary nonlinear function or transformation (see Figure 2.13).

A set of sigma points are selected, with mean $\bar{\mathbf{x}}$ and sample covariance P_{xx}. The nonlinear function is applied to each point in turn to yield a cloud of transformed points with mean and covariance $\bar{\mathbf{y}}$ and P_{yy}.

The main difference with respect to Monte Carlo methods is that the sampling process is not governed by random selection; instead, it follows a precise and deterministic algorithm. As the challenges of statistical convergence are not a concern, it becomes possible to capture high-order information about the distribution with a remarkably small number of points [24].

UKF Algorithm

The state and measurement equations are the following:

$$\mathbf{x}_{k+1} = f(\mathbf{x}_k, \mathbf{v}_k), \tag{2.27}$$

$$\mathbf{y}_k = g(\mathbf{x}_k, \mathbf{n}_k). \tag{2.28}$$

The following are the main steps for the Unscented Kalman Filter (UKF) [25]:

1. Definition of sigma points and weights: if N is the dimension of the state, $2N + 1$ sigma points are needed. The following equations show how to obtain sigma points and their associated weights:

$$\mathcal{X}_0 = \bar{\mathbf{x}}, \tag{2.29}$$

$$\mathcal{X}_i = \bar{\mathbf{x}} + (\sqrt{(N+\lambda)P_{xx}})_i, i = 1, ..., N, \tag{2.30}$$

$$\mathcal{X}_i = \bar{\mathbf{x}} - (\sqrt{(N+\lambda)P_{xx}})_{i-N}, i = N+1, ...,2N, \tag{2.31}$$

$$w_0 = \frac{\lambda}{N+\lambda}, \tag{2.32}$$

$$w_i = \frac{1}{2(N+\lambda)}, \tag{2.33}$$

where $\lambda = 3 - N$.

2. Initialization:

$$\hat{\mathbf{x}}_0 = E[\mathbf{x}_0], \tag{2.34}$$

$$P_{xx0} = E[(\mathbf{x}_0 - \hat{\mathbf{x}}_0)(\mathbf{x}_0 - \hat{\mathbf{x}}_0)^T], \tag{2.35}$$

$$\hat{\mathbf{x}}_0^a = E[\mathbf{x}^a] = [\hat{\mathbf{x}}_0^T \quad 0 \quad 0]^T, \tag{2.36}$$

$$P_{xx0}^a = E[(\mathbf{x}_0^a - \hat{\mathbf{x}}_0^a)(\mathbf{x}_0^a - \hat{\mathbf{x}}_0^a)^T] = \begin{bmatrix} P_0 & 0 & 0 \\ 0 & P_v & 0 \\ 0 & 0 & P_n \end{bmatrix}. \tag{2.37}$$

3. Prediction phase, where the state is predicted:

$$\mathcal{X}_{k|k-1}^x = f[\mathcal{X}_{k-1}^x, \mathcal{X}_{k-1}^v], \tag{2.38}$$

$$\hat{\mathbf{x}}_k^- = \sum_{i=0}^{2N} w_i \mathcal{X}_{i,k|k-1}^x, \tag{2.39}$$

$$P_{xxk}^- = \sum_{i=0}^{2N} w_i [\mathcal{X}_{i,k|k-1}^x - \hat{\mathbf{x}}_k^-][\mathcal{X}_{i,k|k-1}^x - \hat{\mathbf{x}}_k^-]^T. \tag{2.40}$$

4. Correction phase, where the state is corrected, taking into account measurements:

$$\mathcal{Y}_{k|k-1} = g[\mathcal{X}_{k|k-1}^x, \mathcal{X}_{k-1}^n], \tag{2.41}$$

$$\hat{\mathbf{y}}_k^- = \sum_{i=0}^{2N} w_i \mathcal{Y}_{i,k|k-1}, \tag{2.42}$$

$$P_{yyk} = \sum_{i=0}^{2N} w_i [\mathcal{Y}_{i,k|k-1} - \hat{\mathbf{y}}_k^-][\mathcal{Y}_{i,k|k-1} - \hat{\mathbf{y}}_k^-]^T, \tag{2.43}$$

$$P_{xyk} = \sum_{i=0}^{2N} w_i [\mathcal{X}_{i,k|k-1} - \hat{\mathbf{x}}_k^-][\mathcal{Y}_{i,k|k-1} - \hat{\mathbf{y}}_k^-]^T, \tag{2.44}$$

$$\mathcal{K} = P_{xyk} P_{yyk}^{-1}, \tag{2.45}$$

$$\hat{\mathbf{x}}_k = \hat{\mathbf{x}}_k^- + \mathcal{K}(\mathbf{y}_k - \hat{\mathbf{y}}_k^-), \tag{2.46}$$

$$P_{xxk} = P_{xxk}^- - \mathcal{K} P_{yyk} \mathcal{K}^T. \tag{2.47}$$

Where: $\mathbf{x}^a = \begin{bmatrix}\mathbf{x}^T & \mathbf{v}^T & \mathbf{n}^T\end{bmatrix}^T$, $\mathcal{X}^a = \begin{bmatrix}(\mathcal{X}^x)^T & (\mathcal{X}^v)^T & (\mathcal{X}^n)^T\end{bmatrix}^T$, P_v is the process noise covariance, P_n is the measurement noise covariance.

2.4.4 Best algorithm selection

As mentioned above, in the case of non-linear systems, the EKF linearises the system equations. In particular, the EKF uses Gaussian Random Variables (GRV) to approximate the state distribution, which is then analytically propagated through the first-order linearization of the nonlinear system. As a result, the EKF can be seen as providing first-order approximations to the optimal terms. Additionally, when the system equations are linearized, the EKF does not account for the uncertainty in the underlying random variable. This is because the first-order Taylor series linearization expands the nonlinear equations just around a single point and ignores the spread (uncertainty) of the prior random variable. These approximations may result in significant errors in the true posterior mean and covariance of the transformed (Gaussian) random variable (RV), which may lead to suboptimal performance and occasionally filter divergence [26].

In the UKF, a superior approach is used to linearize the nonlinear function. Instead of relying on a truncated Taylor-series expansion at a single point, it has opted for a more effective method. This involves linearizing the function through linear regression, considering r points (sigma points) sampled from the prior distribution of the state RV. These points are matched with their corresponding true nonlinear functional evaluations. By incorporating the statistical properties of the prior RV, the expected linearization error is significantly reduced compared to the error resulting from a truncated Taylor-series linearization [26].

The selection of sigma-points should be done in a manner that they capture the most important statistical properties of the prior random variable x. Because of this, for non-linear systems the UKF performs better than the EKF and this can be seen very well in Figure 2.14.

Considering the highly non-linear nature of the system under investigation, the decision was made to employ a UKF algorithm for localization, as expounded in subsequent chapters. This choice is additionally motivated by the requirement to calculate Jacobians for both the state function and measurement function to develop an EKF algorithm. The problem is that obtaining the Jacobian function of measurements is an exceedingly intricate task in our case, which again justifies the use of the UKF over the EKF.

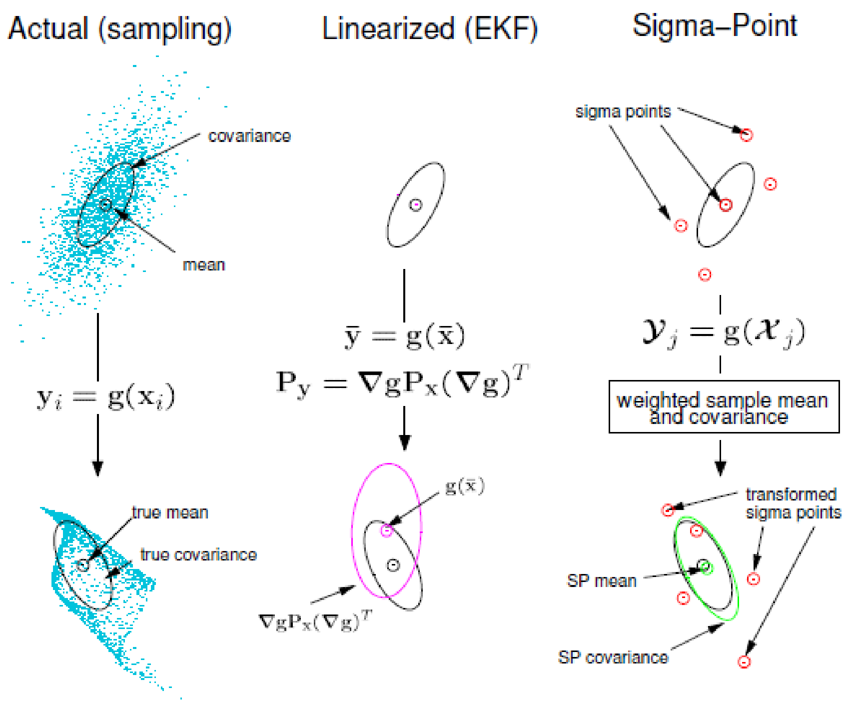

Figure 2.14: Example of the sigma-point approach for mean and covariance propagation: A) actual, B) EKF (first-order linearization), c) UKF (sigma-point approach) [26].

Chapter 3

Real-time Estimation of Localization Correctness

Taddese et al. [14] introduced a new system for estimating poses that combines a permanent magnet and an electromagnet (see Fig. 3.1). The system demonstrated impressive results in static tests, with average errors of less than 5 mm in any single position axis and 6° in any orientation angle. By implementing the Particle Filter (PF) algorithm in parallel, the system achieved an average update rate of 100 Hz. The system surpassed the necessary workspace requirements, which had a radius of 150 mm, due to the larger size of the External Permanent Magnet (EPM), utilization of multiple magnetic field sources, and the higher sampling rate employed during signal acquisition.

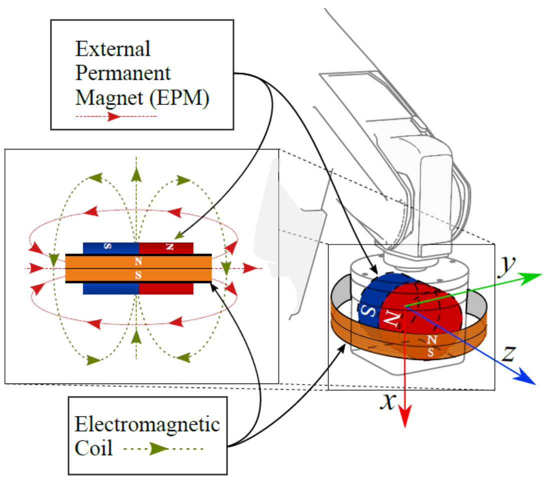

Figure 3.1: EPM augmented with an electromagnetic coil.

Although the PF algorithm has proven to be very successful, there are several motivations for developing certain parameters to estimate the correctness of the localization in real-time:

- Drift phenomenon: in certain scenarios, a phenomenon known as drift can occur, where the estimated position of the endoscope continues to diverge with respect to the true position.

- Calibration errors: errors can arise from neglecting to calibrate the endoscope prior to use or employing an incorrect calibration file. In such cases, drift may not be present, but the localization estimate becomes erroneous. Detecting this error is challenging, as there are no apparent indicators of localization issues, unlike with drift.

- Lack of covariance matrices: the PF algorithm lacks covariance matrices that aid in real-time error determination. The absence of these matrices poses a challenge when assessing localization errors promptly and accurately.

In order to facilitate real-time evaluation of localization correctness, a comprehensive exploration of various parameters was undertaken. These parameters were carefully identified to establish a robust framework for assessing the correctness of localization in different scenarios. To ensure reliability and effectiveness, a multi-phased approach was adopted. The initial phase involved conducting meticulous tests to ascertain the interrelationships between different parameters. This process aimed to establish how these parameters should be interconnected and how their values could be combined to yield meaningful insights into the quality of localization. Additionally, specific thresholds were defined to discern between good and bad localization. Moving forward, a second validation phase was implemented to rigorously examine and confirm the effectiveness of the identified parameters and thresholds. This phase was essential in verifying the reliability and accuracy of the chosen criteria. By subjecting the system to diverse scenarios and meticulously analysing the results, any potential limitations or discrepancies were addressed, ensuring the overall robustness of the evaluation framework. Finally, the culmination of this extensive investigation led to the integration of the code into the PF algorithm. By incorporating the identified parameters and thresholds, the PF algorithm was enhanced to deliver real-time estimation of the correctness of localization. This integration enabled prompt and continuous evaluation, allowing users to dynamically monitor and assess the accuracy of the system's localization output.

3.1 Parameters

To evaluate in real-time the correctness of localization, three distinct parameters have been meticulously identified. The significance and nature of these parameters are expounded upon below.

3.1.1 Effective Sample Size

The definition of the Effective Sample Size (ESS) parameter is as follows:

$$ESS = \frac{1}{\sum_{n=1}^{N} \bar{w}_n^2}, \tag{3.1}$$

where N is the total number of particles (in our case $N = 10000$), and $\bar{w}_n$ is the normalized weights:

$$\bar{w}_n = \frac{w_n}{\sum_{i=1}^{N} w_i}, n = 1, ..., N. \tag{3.2}$$

The ESS takes into account the weights w assigned to the particles and is an important measure of the efficiency of Monte Carlo methods. ESS can take values from 1 to N and is used in the Particle Filter algorithm to decide when to do resampling:

- $ESS = 1$ means that all the weight is assigned to one particle;
- $ESS = N$ means that the weights are equally distributed among the N particles.

3.1.2 Weighted mean Distance

The Weighted mean Distance (WD) is defined as follows:

$$WD = \frac{\sum_{n=1}^{N} w_n \cdot \|x_{mean} - x_n\|}{w_{tot}}, \tag{3.3}$$

where w_n is the weight associated with particle n, x_{mean} is the mean value assumed by the state, taking into account all particles and all weights associated with them, x_n is the state associated with particle n, w_{tot} is the sum of all weights.

WD is the weighted average (with respect to particle weights) of the distance between the particle values and the calculated mean.

3.1.3 Weighted mean Square Distance

The Weighted mean Square Distance ($WD2$) is defined as follows:

$$WD2 = \frac{\sum_{n=1}^{N} w_n \cdot \|x_{mean} - x_n\|^2}{w_{tot}}, \tag{3.4}$$

where w_n is the weight associated with particle n, x_{mean} is the mean value assumed by the state, taking into account all particles and all weights associated with them, x_n is the state associated with particle n, w_{tot} is the sum of all weights.

$WD2$ is the weighted average (with respect to particle weights) of the squared distance between the particle values and the calculated mean.

3.2 Scenarios

To thoroughly test and validate the parameters, a comprehensive set of seven distinct scenarios has been identified. These scenarios have been specifically chosen to ensure robust examination and validation of the parameters under various conditions.

1. Stationary situation – No singularity: the endoscope remains in a fixed position and is not aligned with the plane of singularity. The localization is expected to be correct.

2. Stationary situation – Singularity plane: the endoscope remains in a fixed position and is aligned with the plane of singularity. Due to the presence of the coil, the localization is expected to be correct.

3. Coil off – No singularity: the endoscope is in a fixed position. The coil, which is initially switched on, is switched off. It is expected that after a transient in which the localization is not good, it will stabilize.

4. Coil off – Singularity plane: the endoscope is in a fixed position. The coil, which is initially switched on, is switched off. It is expected that localization will not be good as long as the coil remains switched off.

5. Endoscope outside the workspace: the endoscope starts from a position inside the workspace, then exits, then re-enters the workspace. It is expected that when the endoscope is outside, localization is not good.

6. Joystick movement: the EPM, and therefore the endoscope, are moved via joysticks. Localization is expected to be good. This scenario is very important as it represents a real operational situation of the system.

7. Wrong calibration: the endoscope was not calibrated correctly. It is expected that the localization is not good. As mentioned in the introduction, detecting the calibration error is challenging, as there are no apparent indicators of localization issues. It is, therefore, important that the indicators are able to recognize when the calibration is incorrect.

3.3 Test phase

During the test phase, the primary objective is to establish the thresholds for the parameters and determine the methodology for analyzing the parameter data. This includes considerations such as whether the data should be analyzed point by point, if any filtering techniques should be applied, or if the analysis should be performed on blocks of points.

It is important to note that the Particle Filter algorithm has an update time of 0.01 seconds. Consequently, the parameter values are also published at the same frequency, ensuring synchronization between the algorithm's update intervals and the publication of parameter values.

Three tests of 30 seconds each were carried out for each of the seven scenarios. First, the mean value and the mean value of the increase (in absolute value)[1] of the parameters were analyzed (see Fig. 3.2).

The main outcomes of this first analysis are as follows:

- when the coil is deactivated and the endoscope is positioned within the plane of singularity, it is observed that the increases in ESS and $WD2$ are notably higher compared to other scenarios;

- in the presence of an erroneous calibration, the average value of ESS significantly decreases, measuring below 1500, whereas in other cases it typically exceeds 3000. Additionally, the mean value of $WD2$ is considerably low, further highlighting the impact of incorrect calibration on the localization performance.

At this stage, distinct thresholds have been established for the three indicators, taking into consideration the previously computed means. Subsequently, an analysis was conducted to determine the number of points surpassing the defined threshold for each scenario. The results obtained are shown in Appendix A.1.1. Following the completion of this analysis, it has been determined that the parameter $WD2$ exhibits a similar trend to WD, but its absolute values do not provide sufficient

[1]The increase in absolute value of a parameter is the difference, in absolute terms, between the value of the parameter at instant i and its value at instant $i-1$.

	Test Number	Test Name	ESS mean	ESS increase mean	WD mean	WD increase mean	WD2 mean	WD2 increase mean	Comment
1	1	1 Stationary Situation – No Singularity	6361	149,10	0,005800	0,001700	2,60E-05	1,62E-05	
	2	2 Stationary Situation – No Singularity	4649	95,26	0,002600	0,000280	5,62E-06	2,15E-06	
	3	3 Stationary Situation – No Singularity	4983	117,20	0,003500	0,000523	9,53E-06	4,29E-06	
2	4	1 Stationary Situation – Singularity Plane	6680	217,68	0,007400	0,002200	4,55E-05	3,01E-05	
	5	2 Stationary Situation – Singularity Plane	6689	241,52	0,007200	0,002000	4,33E-05	2,54E-05	
	6	3 Stationary Situation – Singularity Plane	6660	229,06	0,007600	0,002300	4,70E-05	3,02E-05	
3	7	1 Coil Off – No Singularity	3399	131,07	0,003700	0,000919	1,25E-05	7,83E-06	
	8	2 Coil Off – No Singularity	3397	135,12	0,004300	0,001200	1,59E-05	9,28E-06	
	9	3 Coil Off – No Singularity	3386	142,18	0,004500	0,001200	1,68E-05	1,01E-05	
4	10	1 Coil Off – Singularity Plane	5434	580,08	0,007400	0,001800	5,82E-05	3,85E-05	When the coil is off and in the plane of singularity, the ESS increase and the WD2 increase are higher than in the other cases
	11	2 Coil Off – Singularity Plane	5403	630,85	0,007800	0,002000	6,24E-05	3,90E-05	
	12	3 Coil Off – Singularity Plane	5367	596,54	0,008400	0,002100	7,20E-05	4,22E-05	
5	13	1 Endoscope Outside The Workspace	7805	384,49	0,024400	0,006200	5,36E-04	3,09E-04	
	14	2 Endoscope Outside The Workspace	6627	600,31	0,019200	0,004600	3,66E-04	1,76E-04	
	15	3 Endoscope Outside The Workspace	6041	145,58	0,010200	0,002100	1,73E-04	8,30E-05	
6	16	1 Joystick Movement	6659	280,52	0,004900	0,000915	2,33E-05	1,17E-05	
	17	2 Joystick Movement	7047	329,94	0,005800	0,001100	3,47E-05	1,67E-05	
	18	3 Joystick Movement	7065	335,60	0,005200	0,000939	2,69E-05	1,28E-05	
7	19	1 Wrong Calibration	692	359,92	0,002300	0,000655	4,42E-06	2,96E-06	When there is a wrong calibration, the average of ESS is less than 1500 (in other cases it is more than 3000). The WD2 mean is also very low
	20	2 Wrong Calibration	1455	487,08	0,002300	0,000705	4,22E-06	2,99E-06	
	21	3 Wrong Calibration	741	690,81	0,002200	0,000776	3,91E-06	3,38E-06	

Figure 3.2: Mean values and mean increases of parameters.

discrimination to identify specific scenarios. Consequently, the subsequent analysis focuses exclusively on the ESS and WD parameters.

To determine the appropriate methodology for analyzing the parameter values and discerning between good and bad localization, three distinct analyses were conducted:

1. Single-point analysis.
2. Low-pass filter analysis.
3. Analysis of sets of points (without filter).

3.3.1 Single-point analysis

The parameter values are analyzed individually, then, point by point, it is defined whether the localization is good or not. After analyzing the results obtained with the different thresholds and combining the indicators in different ways, it was concluded that localization is bad when at least one of the following inequalities occurs:

$$ESS \leq 2500, \tag{3.5}$$
$$ESS \geq 9000, \tag{3.6}$$
$$|ESS_i - ESS_{i-1}| \geq 600, \tag{3.7}$$
$$WD \geq 0.018. \tag{3.8}$$

The results obtained in each scenario using these thresholds and this combination of parameters are analyzed. The percentage of bad localization for each scenario is shown in Table 3.1.

Test number	Test name	% of bad localization
1	Stationary situation – No singularity	0.00%
2	Stationary situation – Singularity plane	2.43%
3	Coil off – No singularity	0.00%
4	Coil off – Singularity plane	45.03%
5	Endoscope outside the workspace	62.31%
6	Joystick movement	13.23%
7	Wrong calibration	90.17%

Table 3.1: Single-point analysis results.

Subsequently, only one of the three tests performed is presented; the other results are shown in Appendix A.1.2.

Stationary situation – No singularity

Figure 3.3 shows the two parameters in test 1. The horizontal red lines represent the thresholds. The evolution of the parameters is shown in green. The blue asterisks represent the result of the localization analysis:

- when the asterisks are above, it means that the localization is bad;
- when asterisks are below, localization is good.

In 100% of the cases the localization was reported as good. This finding accurately reflects the expected reality, considering that in this scenario it is expected good localization.

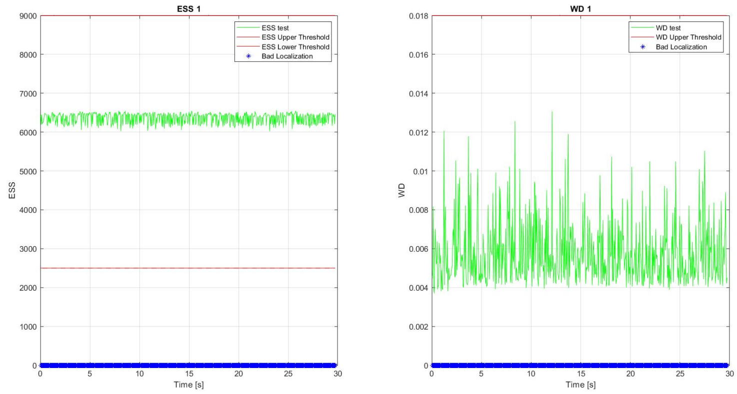

Figure 3.3: Stationary situation – No singularity: ESS and WD parameters, test 1.

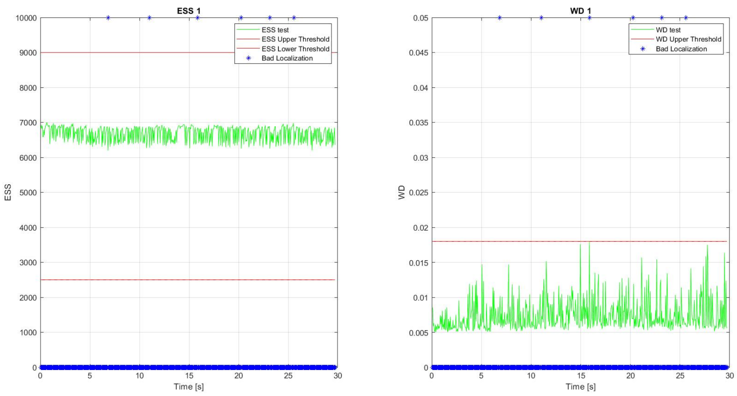

Figure 3.4: Stationary situation – Singularity plane: ESS and WD parameters, test 1.

Stationary situation – Singularity plane

Figure 3.4 shows the two parameters in test 1. In almost all points the localization is reported as good. Due to the presence of the coil, even if the endoscope is in the plane of singularity, the localization is still good, and the parameters indicate this correctly.

Coil off – No singularity

Figure 3.5 shows the two parameters in test 1. At about 4 seconds the coil is switched off. It can be seen that there is an increment of the ESS increase and,

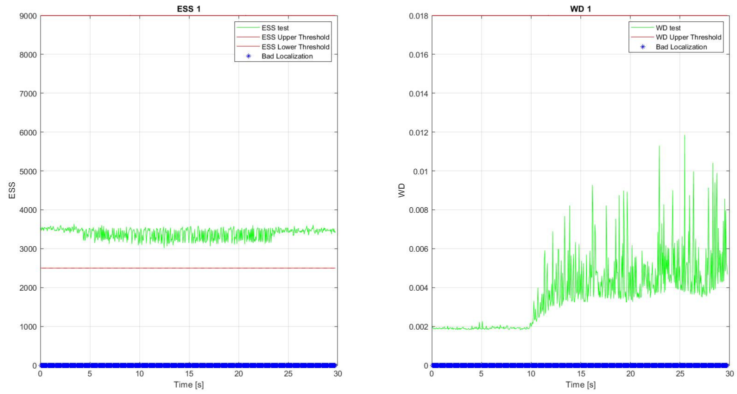

Figure 3.5: Coil off – No singularity: ESS and WD parameters, test 1.

with some delay, an increment in the WD value. However, the change does not allow the thresholds to be exceeded, so the parameters continue to confirm that the localization is good, faithfully following what happens in reality.

Coil off – Singularity plane

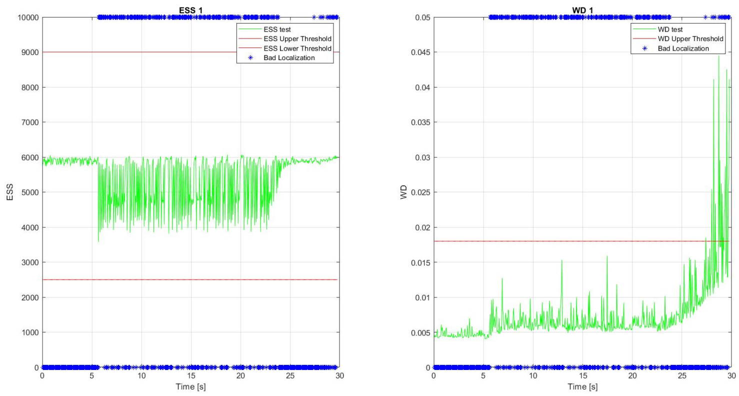

Figure 3.6: Coil off – Singularity plane: ESS and WD parameters, test 1.

Figure 3.6 shows the two parameters in test 1. At about 6 seconds the coil is switched off. It can be seen that there is an increment of the ESS increase and, with some delay, an increment in the WD value. In this scenario, both parameters are important: ESS is able to notice that localization is no longer good as soon as the coil is switched off but stabilizes after a certain period; WD notices the change with a certain delay but is crucial in showing that localization is not good when

ESS stabilizes.

In general, it should turn out that localization is not good for all points after the coil is switched off. In the Figure 3.6 it can be seen that there is a continuous transition between good and bad localization. This is due to the fact that the points are analyzed individually and not as a whole. To solve this problem, blocks of points are analyzed in the following analyses.

Endoscope outside the workspace

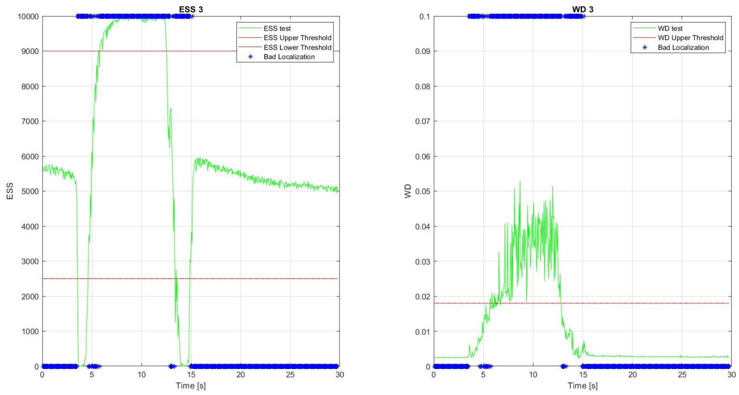

Figure 3.7: Endoscope outside the workspace: ESS and WD parameters, test 3.

Figure 3.7 shows the two parameters in test 3. The endoscope is taken out of the workspace between seconds 4 and 15. During this period of time the parameters clearly show that the localization is not good.

Joystick movement

Figure 3.8 shows the two parameters in test 1. During the test, it was noted that there are some moments when the localization is not stable, i.e., the estimated position continues to oscillate. In these instants, the localization is not good, and this can be seen with the ESS parameter.

Wrong calibration

Figure 3.9 shows the two parameters in test 3. In this scenario, the localization is completely wrong, and this is correctly seen thanks to the ESS parameter, which is almost constantly below the threshold.

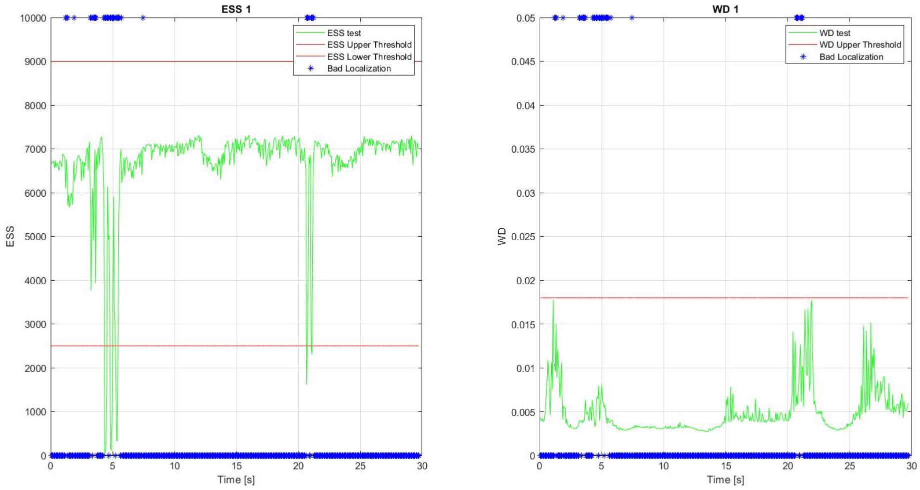

Figure 3.8: Joystick movement: ESS and WD parameters, test 1.

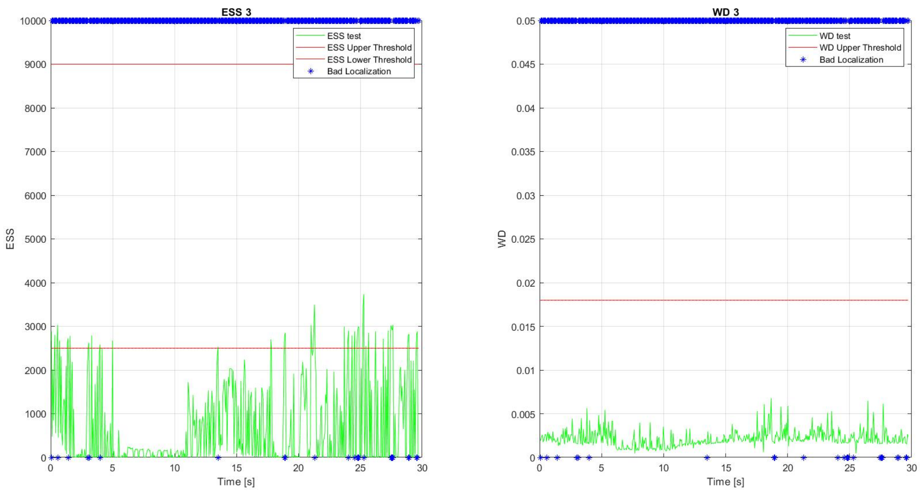

Figure 3.9: Wrong calibration: ESS and WD parameters, test 3.

3.3.2 Low-pass filter analysis

Parameter values are analyzed in blocks of 16 points at a time and are filtered using a low-pass filter (LPF) with $f_{cutoff} = 200Hz$. For each block of points, the localization is defined as bad when at least one of the following inequalities occurs:

$$ESS_{mean} \leq 2500, \tag{3.9}$$
$$ESS_{mean} \geq 9000, \tag{3.10}$$
$$|ESS_{max} - ESS_{min}| \geq 800, \tag{3.11}$$
$$WD_{mean} \geq 0.014. \tag{3.12}$$

By filtering the data, the trend in parameter values changes. This is why the thresholds have been changed from the previous analysis. The percentage of bad localization for each scenario is shown in Table 3.2.

Test number	Test name	% of bad localization
1	Stationary situation – No singularity	0.00%
2	Stationary situation – Singularity plane	0.92%
3	Coil off – No singularity	0.00%
4	Coil off – Singularity plane	60.55%
5	Endoscope outside the workspace	75.93%
6	Joystick movement	29.35%
7	Wrong calibration	95.00%

Table 3.2: Low pass filter analysis results.

In general, it can be said that the percentages obtained more closely reflect reality than in the previous analysis. However, there are two problems:

- by filtering the data, the peaks are dampened, and thus the threshold on the increase loses some value;
- doing an LPF every 16 points has a computational cost.

Subsequently, only one of the three tests performed is presented; the other results are shown in Appendix A.1.3.

Stationary situation – No singularity

Figure 3.10 shows the two parameters in test 1. In this analysis, data filtered through a LPF are shown in black. In 100% of the cases the localization was

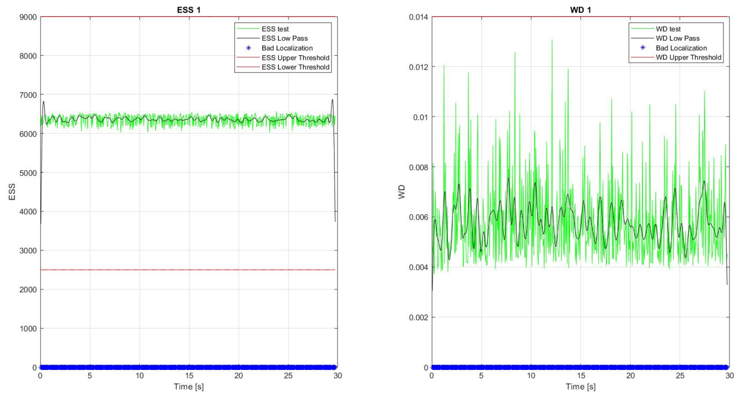

Figure 3.10: Stationary situation – No singularity: ESS and WD parameters, test 1.

reported as good. This finding accurately reflects the expected reality, considering that in this scenario it is expected good localization. Compared to the previous analysis, it can be seen that the filter dampens the peaks.

Stationary situation – Singularity plane

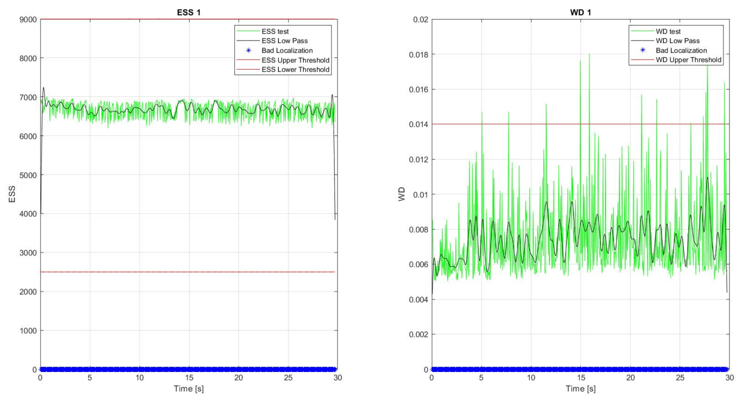

Figure 3.11: Stationary situation – Singularity plane: ESS and WD parameters, test 1.

Figure 3.11 shows the two parameters in test 1. In almost all points the localization is reported as good. Due to the presence of the coil, even if the endoscope is in the plane of singularity, the localization is still good, and the parameters indicate this correctly. Compared to the previous analysis, the percentage of bad localization has decreased. This confirms that analyzing points in blocks and not individually is better.

Coil off – No singularity

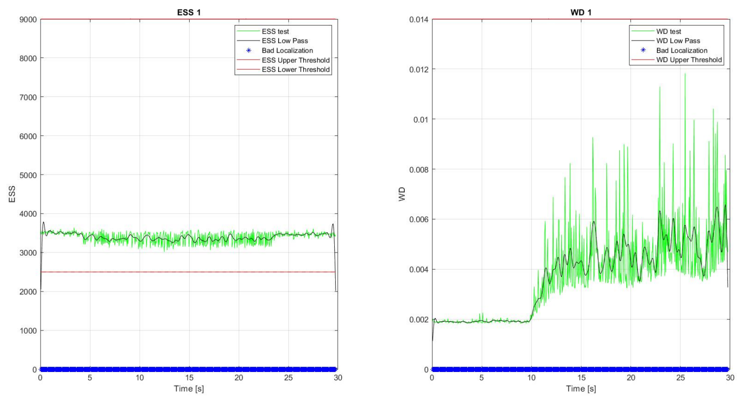

Figure 3.12: Coil off – No singularity: ESS and WD parameters, test 1.

Figure 3.12 shows the two parameters in test 1. At about 4 seconds the coil is switched off. It can be seen that there is an increment of the ESS increase and, with some delay, an increment in the WD value. However, the change does not allow the thresholds to be exceeded, so the parameters continue to confirm that the localization is good, faithfully following what happens in reality.

Coil off – Singularity plane

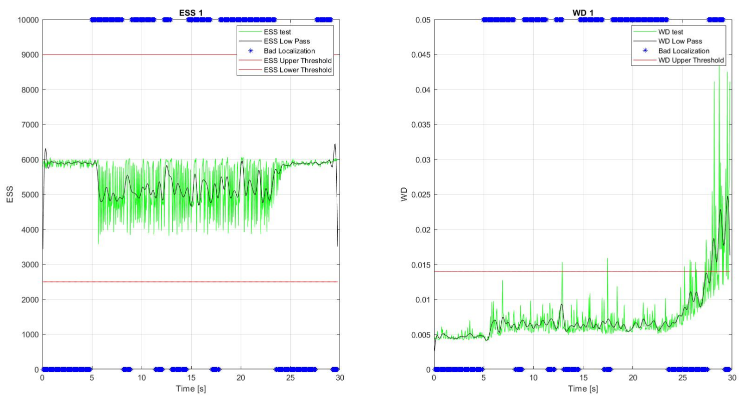

Figure 3.13: Coil off – Singularity plane: ESS and WD parameters, test 1.

Figure 3.13 shows the two parameters in test 1. At about 6 seconds the coil is switched off. It can be seen that there is an increment of the ESS increase and, with some delay, an increment in the WD value.

In general, it should turn out that localization is not good for all points after the coil is switched off. By analyzing the points in blocks and not individually, it allows to increase the percentage of bad localization when the coil is off, improving the result previously found.

Endoscope outside the workspace

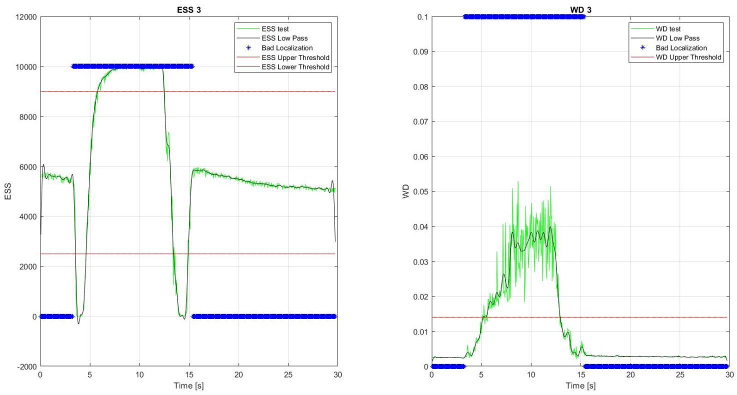

Figure 3.14: Endoscope outside the workspace: ESS and WD parameters, test 3.

Figure 3.14 shows the two parameters in test 3. The endoscope is taken out of the workspace between seconds 4 and 15. During this period of time the parameters clearly show that the localization is not good.

Joystick movement

Figure 3.15 shows the two parameters in test 1. During the test, it was noted that there are some moments when the localization is not stable, i.e., the estimated position continues to oscillate. In these instants, the localization is not good, and this can be seen with the ESS parameter. The analysis of blocks of points allows to capture this phenomenon better.

Wrong calibration

Figure 3.16 shows the two parameters in test 3. In this scenario, the localization is completely wrong, and this is correctly seen thanks to the ESS parameter, which

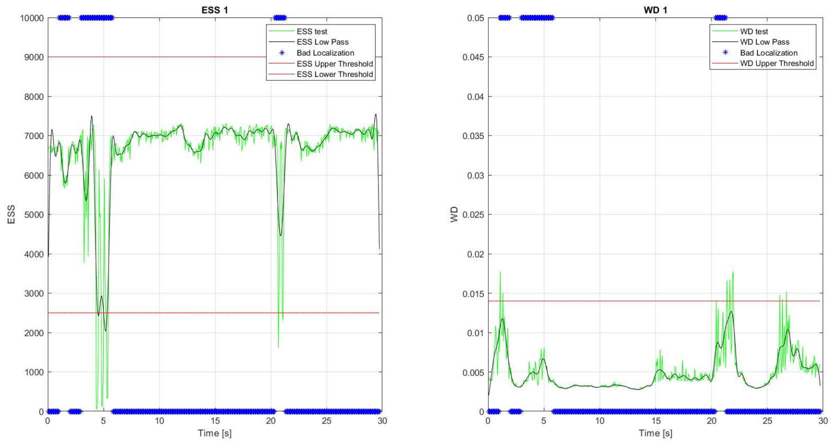

Figure 3.15: Joystick movement: ESS and WD parameters, test 1.

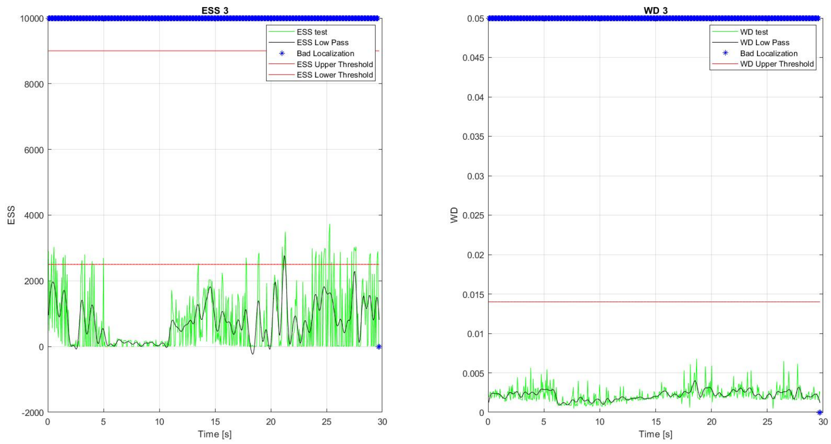

Figure 3.16: Wrong calibration: ESS and WD parameters, test 3.

is almost constantly below the threshold.

3.3.3 Analysis of sets of points (without filter)

Parameter values are analyzed in blocks of 15 points at a time. For each block of points, the localization is defined as bad when at least one of the following inequalities occurs for more than 6 out of 15 points:

$$ESS \leq 2500, \tag{3.13}$$

$$ESS \geq 9000, \tag{3.14}$$

$$|ESS_i - ESS_{i-1}| \geq 600, \tag{3.15}$$

$$WD \geq 0.018. \tag{3.16}$$

The percentage of bad localization for each scenario is shown in Table 3.3.

Test number	Test name	% of bad localization
1	Stationary situation – No singularity	0.00%
2	Stationary situation – Singularity plane	0.00%
3	Coil off – No singularity	0.00%
4	Coil off – Singularity plane	61.54%
5	Endoscope outside the workspace	66.38%
6	Joystick movement	13.27%
7	Wrong calibration	95.33%

Table 3.3: Results of the analysis of sets of points.

The results obtained with this third type of analysis are better than the analysis with the filter for the following reasons:

- the bad localization percentages better respect the reality;
- by not filtering the data, the increase can be appreciated more (the peaks are not dampened);
- there is no high computational cost, considering that a filter is not used.

Subsequently, only one of the three tests performed is presented; the other results are shown in Appendix A.1.4.

Stationary situation – No singularity

Figure 3.17 shows the two parameters in test 1. In 100% of the cases the localization was reported as good. This finding accurately reflects the expected reality, considering that in this scenario it is expected good localization.

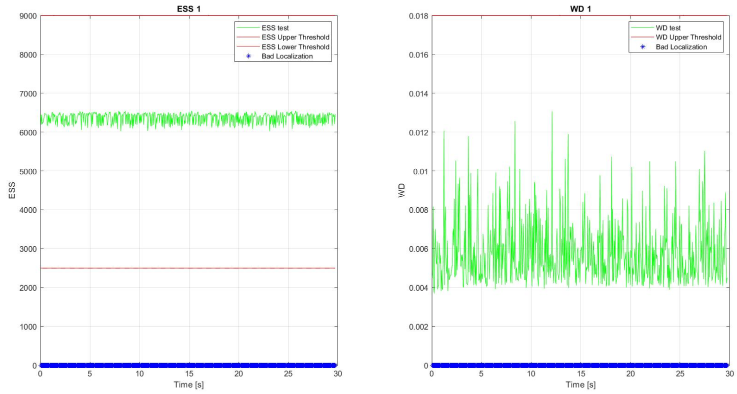

Figure 3.17: Stationary situation – No singularity: ESS and WD parameters, test 1.

Stationary situation – Singularity plane

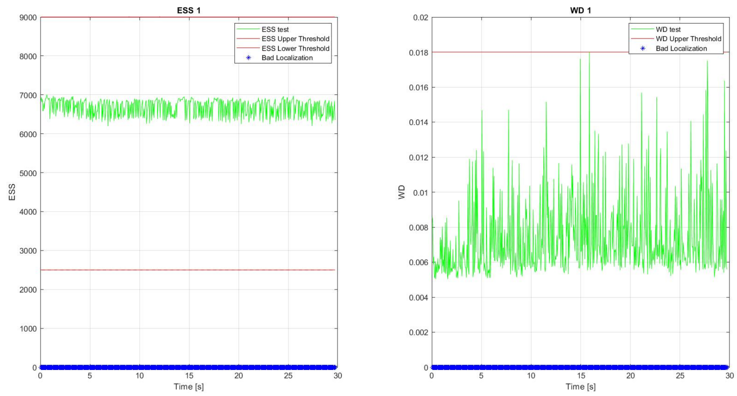

Figure 3.18: Stationary situation – Singularity plane: ESS and WD parameters, test 1.

Figure 3.18 shows the two parameters in test 1. In 100% of the cases the localization was reported as good. This finding accurately reflects the expected reality, considering that in this scenario it is expected good localization.

Coil off – No singularity

Figure 3.19 shows the two parameters in test 1. In 100% of the cases the localization was reported as good. This finding accurately reflects the expected reality, considering that in this scenario it is expected good localization.

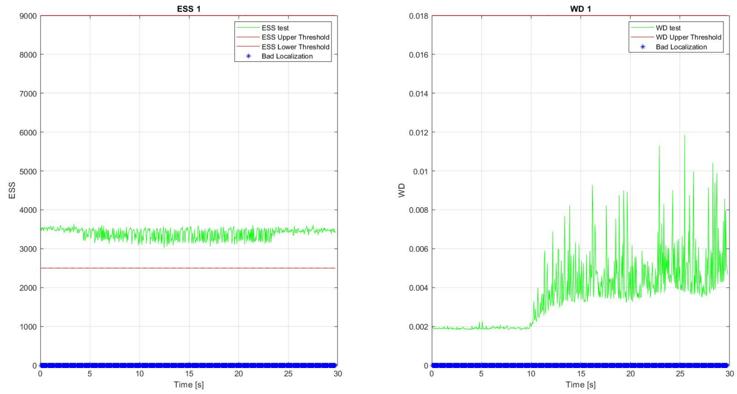

Figure 3.19: Coil off – No singularity: ESS and WD parameters, test 1.

Coil off – Singularity plane

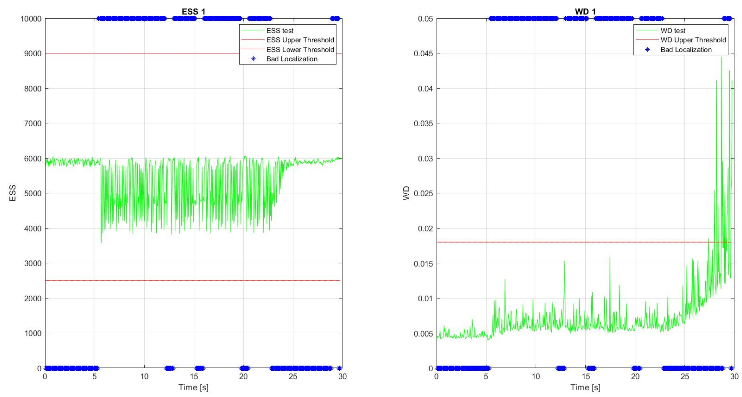

Figure 3.20: Coil off – Singularity plane: ESS and WD parameters, test 1.

Figure 3.20 shows the two parameters in test 1. At about 6 seconds the coil is switched off. It can be seen that there is an increment of the ESS increase and, with some delay, an increment in the WD value.

The result obtained is very similar to that of the analysis with the filter.

Endoscope outside the workspace

Figure 3.21 shows the two parameters in test 3. The endoscope is taken out of the workspace between seconds 4 and 15. During this period of time the parameters clearly show that the localization is not good.

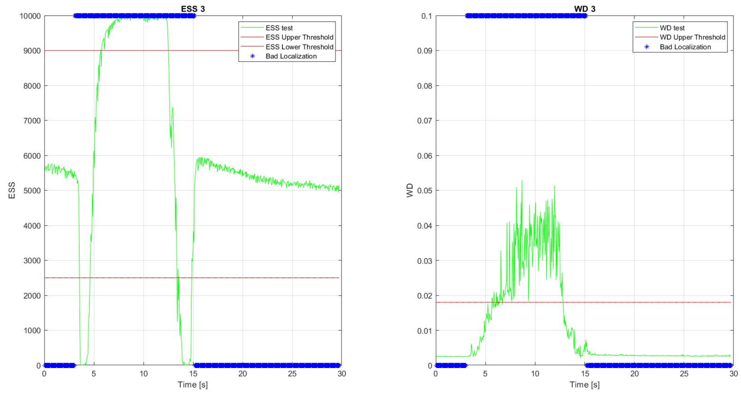

Figure 3.21: Endoscope outside the workspace: *ESS* and *WD* parameters, test 3.

Joystick movement

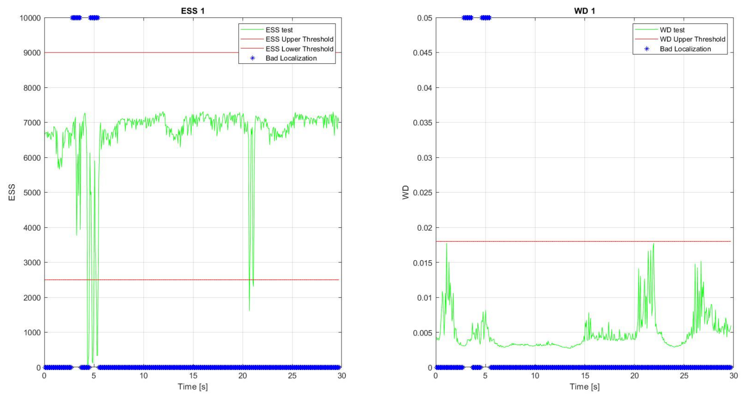

Figure 3.22: Joystick movement: *ESS* and *WD* parameters, test 1.

Figure 3.22 shows the two parameters in test 1. During the test, it was noted that there are some moments when the localization is not stable, i.e., the estimated position continues to oscillate. In these instants, the localization is not good, and this can be seen with the *ESS* parameter. Compared to the analysis with the filter, the points that go under the threshold of *ESS* rapidly are neglected: if the variation is very rapid, it is not considered.

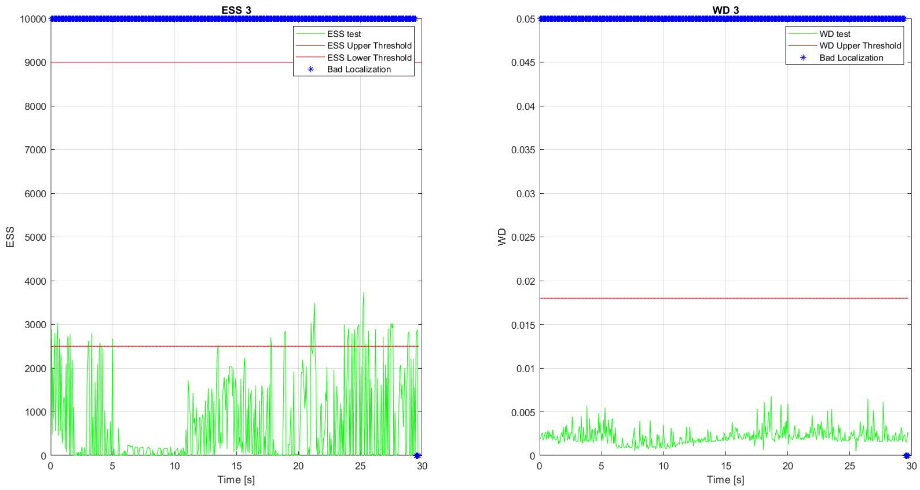

Figure 3.23: Wrong calibration: ESS and WD parameters, test 3.

Wrong calibration

Figure 3.23 shows the two parameters in test 3. In this scenario, the localization is completely wrong, and this is correctly seen thanks to the ESS parameter, which is almost constantly below the threshold.

3.4 Validation phase

The validation phase plays a crucial role in confirming the results obtained during the test phase. Additional experiments were then carried out in the laboratory for each scenario, and it was assessed whether the parameters are able to correctly indicate when the localization is good and when it is not. The last analysis presented, Analysis of sets of points (without filter), was used to analyze the parameter values, considering that it was the analysis that provided the best results in the test phase.

For each scenario, the percentage of the following points was calculated:

- Good Estimation: the estimation of the parameters matches the localization (e.g., the estimation of the parameters says that the localization is not good, and the localization is not good).

- False Positive: parameters estimates indicate that the localization is good, but the localization is not good.

- False Negative: parameters estimates indicate that the localization is not good, but the localization is good.

This phase is divided into two parts: static scenarios analysis and dynamic scenario analysis.

3.4.1 Static scenarios

A ground truth is needed to define whether the parameters correctly indicate if the localization is good or not. In the case of static scenarios, where the endoscope remains fixed in one position, the known position serves as the reference point.

To define whether localization is good or not, a threshold must be set (relative to the known position) beyond which the estimated position is no longer good: if the difference, in absolute value, between the estimated and actual position exceeds the threshold in at least one of the components of the state (x, y, z, yaw angle), it means that the localization is not good.

The selection of the threshold took into account two key factors:

- the variations observed in the stationary scenario, which were considered indicative of good localization;
- the average accuracy of the localization algorithm in static conditions, as determined by Taddese et al. [14].

The thresholds are presented in Table 3.4.

Linear threshold [m]	Angular threshold [°]
0.004	5.00

Table 3.4: Thresholds for the static scenarios.

Three tests of 30 seconds each were carried out for the following static scenarios:

- Stationary situation – No singularity.
- Stationary situation – Singularity plane.
- Coil off – No singularity.
- Coil off – Singularity plane.
- Endoscope outside the workspace.
- Wrong calibration.

Test name	Good Estimation	False Positive	False Negative
Stationary situation – No singularity	100.00%	0.00%	0.00%
Stationary situation – Singularity plane	100.00%	0.00%	0.00%
Coil off – No singularity	76.00%	23.83%	0.17%
Coil off – Singularity plane	87.87%	11.32%	0.80%
Endoscope outside the workspace	92.20%	5.40%	2.40%
Wrong calibration	100.00%	0.00%	0.00%

Table 3.5: Results of the validation phase, static scenarios.

Plots of all tests can be found in Appendix A.2.1. The results obtained, concerning good estimation, false positive and false negative, are shown in Table 3.5.

In general, it can be said that the results obtained are good:

1. Stationary situation – No singularity: it was assumed that localization in the stationary case is good, so obviously a very good result was obtained in this scenario.

2. Stationary situation – Singularity plane: a very good result was also achieved in this scenario.

3. Coil off – No singularity: the elevated occurrence of false positives can be attributed to the position stabilizing towards the end, even though the actual localization is not accurate. However, this issue is not significantly problematic for two main reasons. Firstly, the primary objective is to ensure that the parameters perform effectively during transient phases, considering that in an operational scenario it is unlikely to stay in a stationary position. Furthermore, if one inadvertently fails to activate the coil, it can be easily noticed through alternative means, such as the absence of coil noise.

4. Coil off – Singularity plane: sometimes a good localization is marked when the coil is off (false positive), but in general the estimation is good.

5. Endoscope outside the workspace: the final part where the endoscope is put back into the workspace has not been considered, as it is not possible

to determine exactly what position it is put back into. A good result was achieved.

6. Wrong calibration: a very good result was achieved in this scenario.

3.4.2 Dynamic scenario

In this scenario, the acceleration of the pose estimated by the localization algorithm is used as ground truth to define whether the localization is good. If the acceleration of localization exceeds a certain threshold, it means that the variation is excessive and localization is not good. However, the actual acceleration of the endoscope must also be taken into account because if the acceleration of the endoscope is actually high, it is permissible to have a high acceleration in localization as well.

To determine when localization is not good, it was therefore decided to:

- define a threshold on localization acceleration, above which localization is not good;
- discard all points where the acceleration of the endoscope is actually high.

To determine the threshold of acceleration:

- it was assumed that in the stationary case (good localization) accelerations are below the threshold;
- the accelerations in different stationary cases were calculated;
- a threshold value four times greater than the maximum of the accelerations in the stationary case was chosen.

The threshold is presented in Table 3.6.

Acceleration threshold $[m/s^2]$
0.40

Table 3.6: Thresholds for the dynamic scenario.

A single 120-second test was carried out for the following dynamic scenario:

- Joystick movement.

The plot of the test can be found in Appendix A.2.2.

The results obtained, concerning good estimation, false positive and false negative, are shown in Table 3.7.

Test name	Good Estimation	False Positive	False Negative
Joystick movement	92.48%	0.57%	6.95%

Table 3.7: Results of the validation phase, dynamic scenario.

The result is good. The high number of false negatives is probably due to the fact that in the joystick movement, bad localization is rarely present for some blocks of points. Considering that blocks of 15 points are analyzed at a time to determine whether localization is good, it can happen that points representing good localization end up in the block where bad localization prevails and are therefore marked as bad localization (false negatives). Considering, however, that the percentage of good estimation is over 90%, it can be said that the result obtained is good.

3.5 Considerations on the results obtained

Considering that the validation phase yielded good results, it can be concluded that the identified parameters allow for an accurate determination of whether the localization is good or not. To obtain a real-time estimation of the localization correctness, lines of code were implemented within the localization algorithm that calculate the parameter values and determine, point by point, whether the localization is good or not. The flowchart of the code is represented in Figure 3.24.

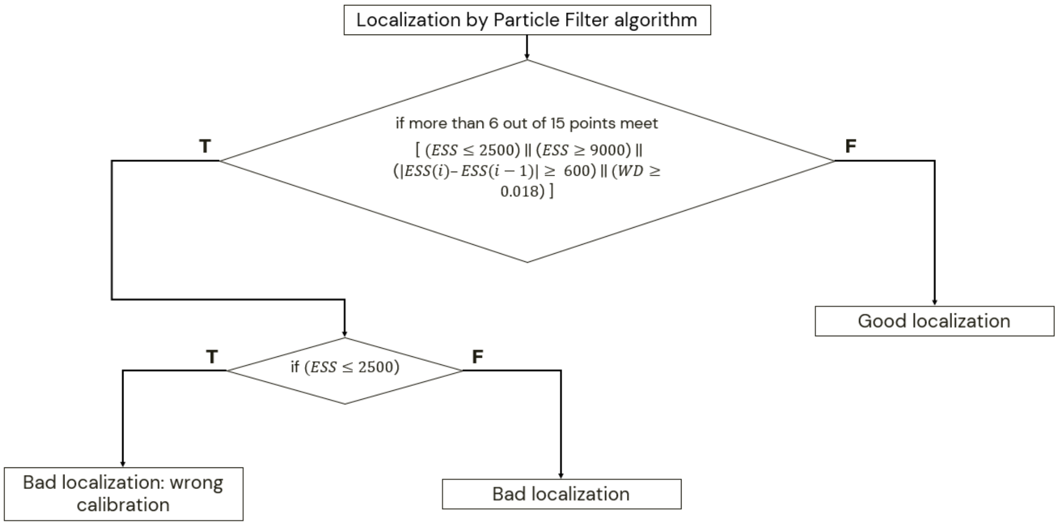

Figure 3.24: Flowchart for the real-time estimation of localization correctness.

As highlighted at the beginning of the chapter, detecting calibration errors poses a challenge, as there are no visible indicators of localization issues. Hence, it was decided not only to indicate when the localization is good or not, but also to specify explicitly, in case of bad localization, whether the issue lies with wrong calibration. Based on the graphs provided for each scenario, it is evident that the ESS parameter falls below the threshold of 2500 primarily when a wrong calibration is present. Therefore, it can be inferred that if the ESS value is below the threshold, there is a high likelihood that the issue is attributed to wrong calibration.

Chapter 4

Unscented Kalman Filter Algorithm

The decision to utilize the Unscented Kalman Filter algorithm for the development of a novel localization algorithm has been previously mentioned. For a comprehensive understanding of the theoretical concepts underlying the Unscented Kalman Filter, please refer to section 2.4. This chapter will delve into the algorithm's implementation details and present the achieved outcomes.

4.1 State variables and covariance matrices

The pose of the endoscope tip is univocally determined by a 3×1 position vector and three Euler Angles, calculated with respect to the world reference system. Concerning the state, taking into account that the Mahoney filter estimates the roll and pitch, the localization algorithm employs a state vector with dimensions of 4×1:

$$x = \begin{bmatrix} p_x \\ p_y \\ p_z \\ \psi \end{bmatrix} \in R^{4\times 1}, \tag{4.1}$$

where p_x, p_y, p_z represent the 3×1 position vector, while ψ represents the yaw. $N = 4$ denotes the dimension of the state-space model.

In the context of the Unscented Kalman Filter, each variable is considered as a Gaussian process, characterized by a mean value and a covariance (or standard deviation). Some covariance matrices were then determined, and the selection of the values associated with the matrices has been based on empirical observations through a trial and error process. It is important to note that higher covariance indicates greater uncertainties associated with the respective variable.

- Initial Process Covariance Matrix: $P_0 = diag([0.1, 0.1, 0.1, 0.1]) \in R^{4\times4}$. This matrix provides insights into the initial uncertainty between the actual states and the estimated ones.

- Process Disturbance Covariance Matrix: $P = diag([0.00015, 0.00015, 0.00015, 0.01]) \in R^{4\times4}$. It provides crucial information regarding the uncertainty impacting the propagation of the states.

- Measurements Covariance Matrix: $Q = diag([0.00001, 0.00001, 0.00001, 0.00001, 0.00001, 0.00001, 0.00001, 0.00001, 0.00001, 0.00001, 0.00001, 0.00001,]) \in R^{12\times12}$. The diagonal elements of this matrix convey valuable information regarding the uncertainties associated with the acquired measurements. These values are dependent on factors such as sensor noise and the mathematical computations employed to obtain the measurements.

4.2 Process model

Using a process model that integrates actuation control inputs has been recognized as a means to achieve superior state estimation. However, in specific applications like magnetically actuated capsule endoscopy, the actual motion of the tracked object can vary significantly from the intended motion due to various environmental factors (such as the capsule getting stuck in a tissue fold or peristalsis). Consequently, constructing an accurate motion model becomes challenging in such scenarios (see Figure 4.1).

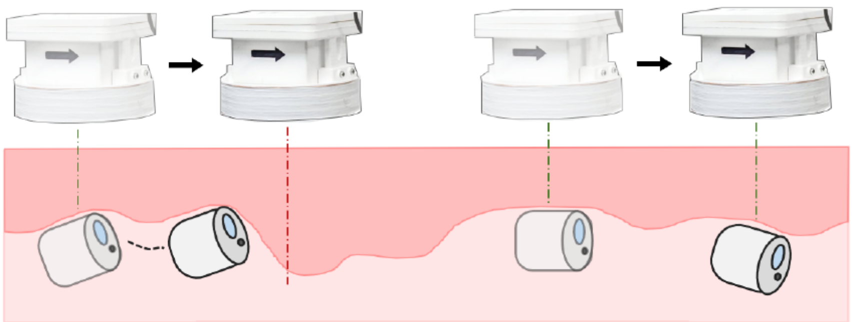

Figure 4.1: Environmental factors, such as tissue folds, can cause different actuation responses from the capsule despite applying the same EPM displacement [5].

For this reason, it was decided to use the random walk process model, considering that Taddese et al. have demonstrated that it is sufficient to localize the endoscope [14]:

$$f_k(\mathbf{x}_{k-1}^i, \mathbf{v}_{k-1}^i) = \mathbf{x}_{k-1}^i + \mathbf{v}_{k-1}^i, \tag{4.2}$$

where

$$\mathbf{v}_{k-1}^i \sim \mathcal{N}(0, P) \tag{4.3}$$

is a sample from a normal distribution, and P is the Process Disturbance Covariance Matrix described above.

4.3 Measurement model

The system uses six single-axis Hall effect sensors positioned in the capsule (see Figure 4.2) so as to approximate two triaxial sensors. It is used a signal processing technique to separately measure the magnetic fields from the EPM and the electromagnetic coil (for more information on the system, see the paper by Taddese et al. [14]).

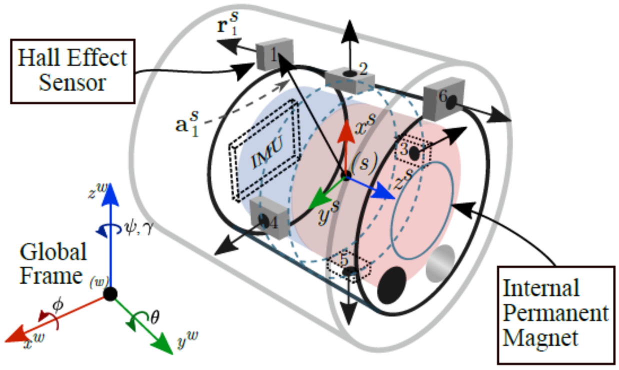

Figure 4.2: The six Hall effect magnetic field sensors and the inertial measurement unit (IMU) found inside the capsule [14].

Knowing the relative position vector, $\mathbf{a}_i^s$, of each Hall sensor with respect to the center of the capsule, the sensor output is calculated by projecting the magnetic field at each Hall sensor in the direction of the sensor's normal vector, $\mathbf{r}_i^s$:

$$b_{E_i}^s = \mathbf{r}_i^{s^T} R_E^s B_E(T_s^E(\mathbf{x}_k^w)\mathbf{a}_i^s), \quad i = 1,2,...,6 \tag{4.4}$$

$$b_{C_i}^s = \mathbf{r}_i^{s^T} R_E^s B_C(T_s^E(\mathbf{x}_k^w)\mathbf{a}_i^s), \quad i = 1,2,...,6 \tag{4.5}$$

where T_s^E: $\mathbb{R}^3 \times \mathbb{S}^1 \rightarrow \mathbb{SE}(3)$ is the homogeneous transformation of the capsule's frame with respect to the EPM frame given by:

$$T_s^E(\mathbf{x}^w) = T_w^E T_s^w(\mathbf{x}^w), \tag{4.6}$$

where T_w^E is the transformation of the world frame with respect to the EPM frame (see Figure 4.3), which is assumed to be known thanks to the forward kinematics of the robot manipulator, while $T_s^w(\mathbf{x}^w)$ is composed of a rotation part, $R_z(\gamma)\tilde{R}_s^w$, and a translation part ($[x_x, x_y, x_z]$).

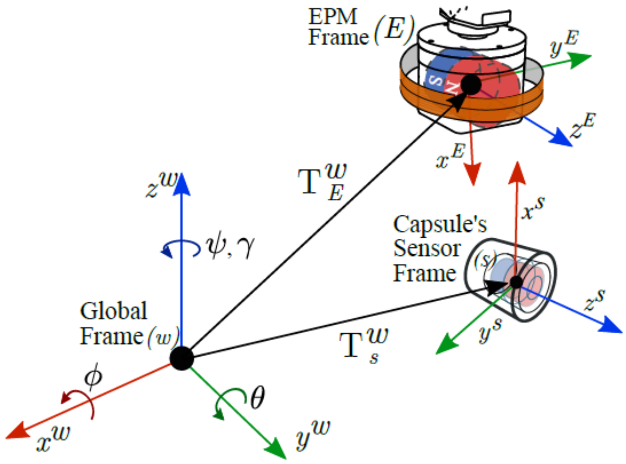

Figure 4.3: Coordinate frames of the magnetic pose estimation system showing the global frame (w), the capsule's sensor frame (s) and the EPM frame (E) [14].

The accuracy of the pose estimate is directly influenced by the selection of a magnetic field model for B_E and B_C. It was chosen to use the generalized complete elliptic integral:

$$C(k_c, p, c, s) = \int_0^{\pi/2} \frac{c\,cos^2\varphi + s\,sin^2\varphi}{(cos^2\varphi + p\,sin^2\varphi)\sqrt{cos^2\varphi + k_c^2\,sin^2\varphi}}\,d\varphi, \tag{4.7}$$

which can be efficiently solved numerically using the Bulirschs algorithm [27]. Considering an electromagnetic coil with radius a, length $2b$, current I and turns per unit length n, the magnetic field components in cylindrical coordinates (ρ, φ, z) are [14]:

$$b_\rho = B_o[\alpha_+ C(k+,1,1,-1) - \alpha_- C(k,1,1,1)], \tag{4.8}$$

$$b_\varphi = 0, \tag{4.9}$$

$$b_z = \frac{B_o a}{a+\rho}[\beta_+ C(k+,\eta^2,1,\eta) - \beta_- C(k_-,\eta^2,1,\eta)], \tag{4.10}$$

where

$$\eta = \frac{a-\rho}{a+\rho}, \tag{4.11}$$

$$B_o = \frac{\mu_0}{\pi} nI, \tag{4.12}$$

$$\alpha_{\pm} = \frac{a}{\sqrt{z_{\pm}^2 + (\rho + a)^2}}, \tag{4.13}$$

$$k_{\pm} = \sqrt{\frac{z_{\pm}^2 + (a - \rho)^2}{z_{\pm}^2 + (a + \rho)^2}}, \tag{4.14}$$

$$z_{\pm} = z \pm b. \tag{4.15}$$

Considering a permanent magnet with the same dimension, the magnetic remanence is:

$$B_r = \mu_0 n I, \tag{4.16}$$

and so B_o becomes:

$$B_o = \frac{B_r}{\pi}. \tag{4.17}$$

The measurement model is crucial because, thanks to it, after predicting the state with the process model, it is possible to calculate the magnetic field values as sensed by the sensors. By making the difference between the calculated magnetic field values and those actually sensed by the sensors, it is possible to estimate the localization error.

4.4 Algorithm explanation

The algorithm is mainly divided into three parts:

1. Initialization: where the state and covariance matrices are initialized.

2. Prediction: where the state is predicted using the process model.

3. Correction: where the predicted state is corrected using the magnetic field values from the sensors and the magnetic field values calculated using the measurement model.

4.4.1 Initialization

- For each of the four variables that make up the state, the initial value is randomly chosen within the workspace.

- The three covariance matrices described earlier are then initialized: Initial Process Covariance Matrix, Process Disturbance Covariance Matrix, and Measurements Covariance Matrix.

4.4.2 Prediction

- As presented in Chapter 2.4, for each state variable, $2N + 1$ sigma points (with $N = 4$ in our case) are defined, along with their corresponding weights.
- The random walk process model is applied to all sigma points, and using the previously calculated weights, the predicted state is then computed. Also the predicted state covariance is calculated.

4.4.3 Correction

- Through the measurement model, the predicted measurement sigma points are computed. Using the weights associated with the sigma points, the predicted measurement vector is calculated.
- The predicted measurement covariance and the cross-covariance matrices are calculated.
- Finally, the state is estimated, taking into account the predicted state and the difference between the magnetic field values perceived by the sensors and the predicted measurement vector.

4.5 Test phase

Given that the Particle Filter algorithm has demonstrated excellent performance under static conditions [14], to evaluate the new localization algorithm, it was tested under similar static conditions. The obtained values were then compared with those obtained using the Particle Filter algorithm.

Several tests were carried out. The results of a 120-second test are shown below (see Figures 4.4 and 4.5).

In terms of position, the mean errors of the UKF with respect to the PF are depicted in Table 4.1. In general, it can be said that the errors obtained are very

Δx $[m]$	Δy $[m]$	Δz $[m]$
0.004	0.000	0.004

Table 4.1: Mean errors of the UKF with respect to the PF.

low, on the order of a few millimeters. From the graphical analysis (see Figure 4.4), it is evident that the UKF yields more stable results compared to the PF. However, it is worth noting that the UKF occasionally converges to a position that deviates

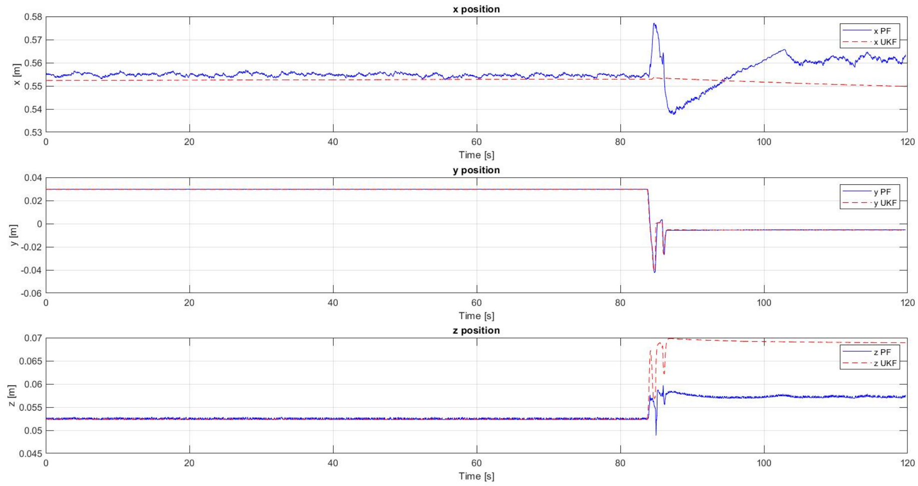

Figure 4.4: Localization estimation under static conditions; comparison between PF and UKF for the position.

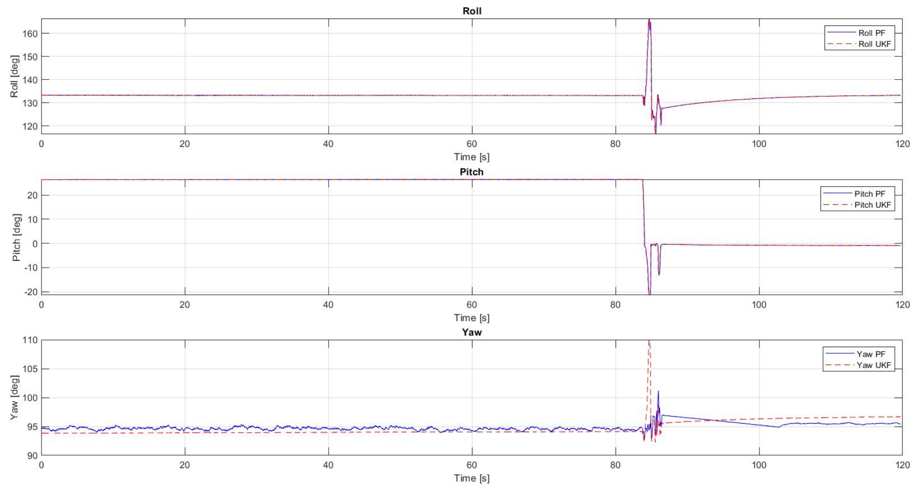

Figure 4.5: Localization estimation under static conditions; comparison between PF and UKF for the orientation.

from the PF's estimate. This behavior could be attributed to the fact that UKF occasionally settles in local minima during the estimation process.

In terms of orientation, the mean errors of the UKF with respect to the PF are depicted in Table 4.2. The errors are very small, and this is also clearly visible in Figure 4.5.

$\Delta\phi$ [°]	$\Delta\theta$ [°]	$\Delta\psi$ [°]
0.000	0.000	0.772

Table 4.2: Mean errors of the UKF with respect to the PF.

In conclusion, after this initial analysis, it can be said that the main advantage of the UKF, compared to the PF, is that it gives a more stable result; the disadvantage is that it sometimes takes longer to find the correct pose and it sometimes gets stuck in relative minima.

However, considering that, as presented in Chapter 3, parameters have been defined to indicate in real-time whether the PF is performing well or poorly, in case the PF is performing well, it is possible to use the result of the PF to guide the UKF. The UKF algorithm was modified as follows. Before the prediction phase, it checks whether the PF is performing well. If it is, the algorithm verifies if the three state variables that define the position, estimated by the UKF, are within a proximity of the corresponding variables estimated by the PF. If they are not, they are forced to stay within the proximity of the PF. By doing so, the estimation obtained from the PF is leveraged to quickly find the estimation of the UKF, which can be different and potentially even better than that of the PF.

To determine the size of the proximity range around the PF, three tests were conducted, which are described below.

4.5.1 Determination of proximity range

Three different ranges in which the UKF has to stay, compared to the PF, were tested, and the results were analyzed.

The first range tested is ±5 mm: the position values estimated by the UKF must have a maximum distance of 5 mm to the values estimated by the PF; if this is not the case, the UKF algorithm is forced to stay within the PF's range. The mean errors of the UKF with respect to the PF obtained for this case are shown in Table 4.3, and the trends of the estimated variables are shown in Figures 4.6 and 4.7.

Δx $[m]$	Δy $[m]$	Δz $[m]$	$\Delta\phi$ [°]	$\Delta\theta$ [°]	$\Delta\psi$ [°]
0.003	0.001	0.003	0.000	0.000	2.939

Table 4.3: Mean errors of the UKF with respect to the PF. Proximity range of ±5 mm.

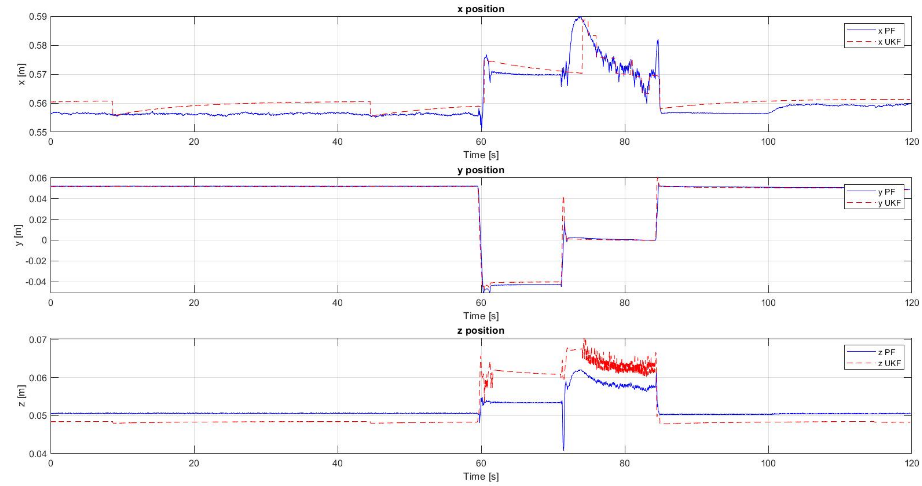

Figure 4.6: Proximity range of ±5 mm. Comparison between PF and UKF for the position.

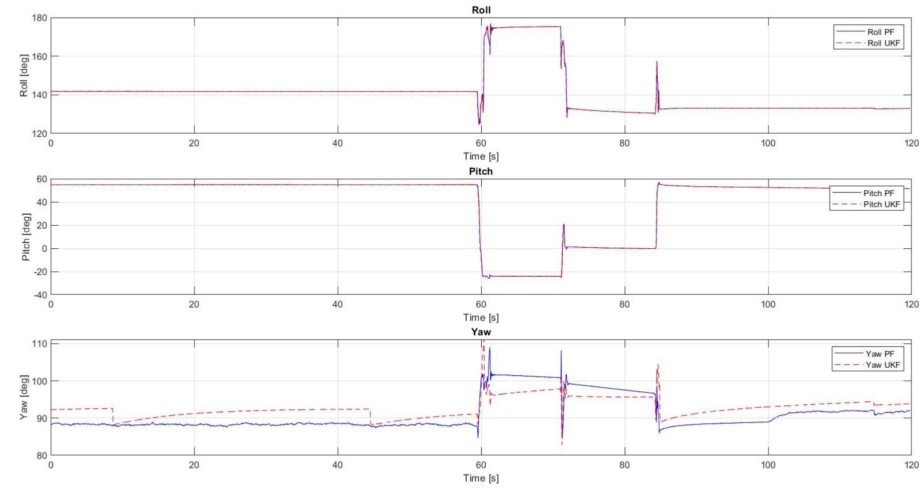

Figure 4.7: Proximity range of ±5 mm. Comparison between PF and UKF for the orientation.

The second range tested is ±10 mm: the position values estimated by the UKF must have a maximum distance of 10 mm to the values estimated by the PF; if this is not the case, the UKF algorithm is forced to stay within the PF's range. The mean errors of the UKF with respect to the PF obtained for this case are shown in Table 4.4, and the trends of the estimated variables are shown in Figures 4.8 and

4.9.

Δx $[m]$	Δy $[m]$	Δz $[m]$	$\Delta \phi$ [°]	$\Delta \theta$ [°]	$\Delta \psi$ [°]
0.003	0.001	0.003	0.000	0.000	3.741

Table 4.4: Mean errors of the UKF with respect to the PF. Proximity range of ±10 mm.

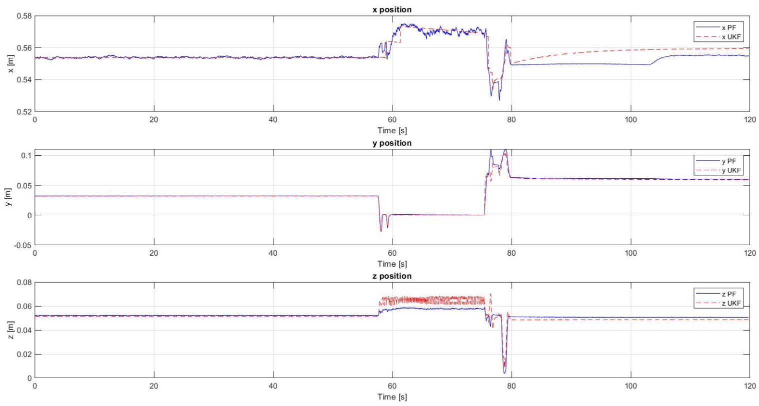

Figure 4.8: Proximity range of ±10 mm. Comparison between PF and UKF for the position.

The third range tested is ±15 mm: the position values estimated by the UKF must have a maximum distance of 15 mm to the values estimated by the PF; if this is not the case, the UKF algorithm is forced to stay within the PF's range. The mean errors of the UKF with respect to the PF obtained for this case are shown in Table 4.5, and the trends of the estimated variables are shown in Figures 4.10 and 4.11.

Δx $[m]$	Δy $[m]$	Δz $[m]$	$\Delta \phi$ [°]	$\Delta \theta$ [°]	$\Delta \psi$ [°]
0.003	0.001	0.003	0.083	0.057	0.576

Table 4.5: Mean errors of the UKF with respect to the PF. Proximity range of ±15 mm.

With regard to the mean errors in the tables, the results obtained in the three cases are very similar. Regarding the trend of the estimated variables, it can be

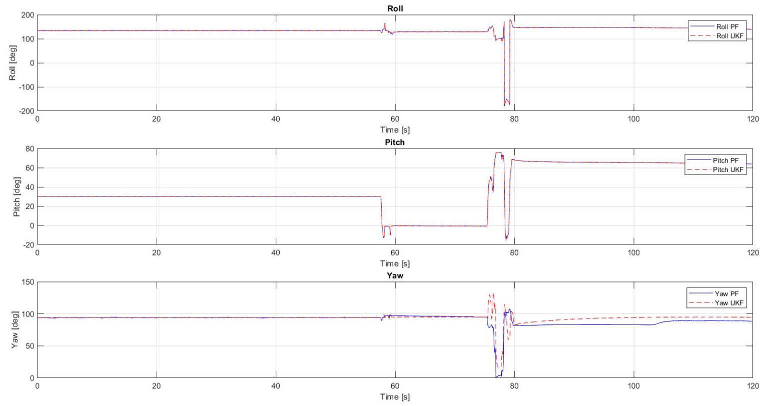

Figure 4.9: Proximity range of ±10 mm. Comparison between PF and UKF for the orientation.

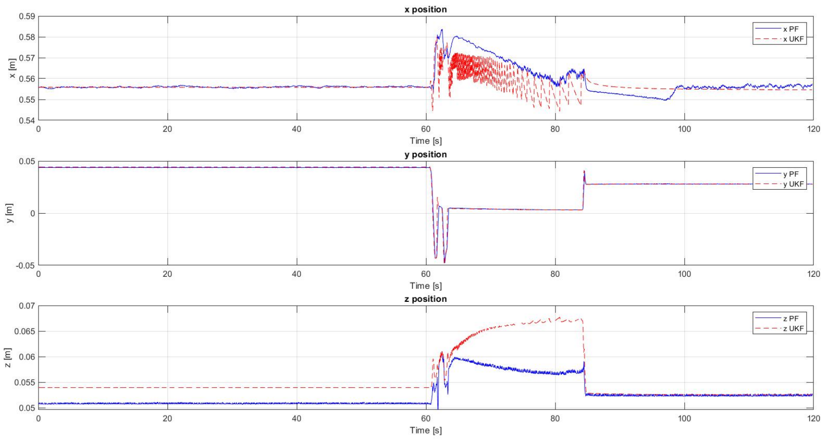

Figure 4.10: Proximity range of ±15 mm. Comparison between PF and UKF for the position.

stated that the greater the range, the greater the risk of having unstable situations for the UKF: the variable estimated by the UKF tends to move out of the range of the PF continually. This can be seen very well for the x position of the third case (see Figure 4.10). For this reason, the range ±15 mm is discarded. To decide which of the other two ranges is the best, the results obtained for PF by Taddese et al. [14] are used: it is true that most of the errors obtained for PF are less than 5 mm (which is why the ±5 mm range was also tested), but there are cases where the error was greater than 5 mm (but still less than 10 mm). Therefore, in order to avoid that the range within which the UKF has to stay, in relation to the PF, is

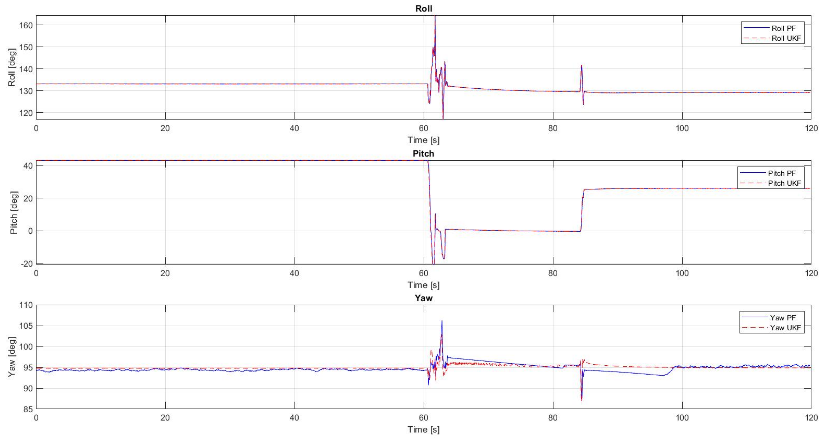

Figure 4.11: Proximity range of ±15 mm. Comparison between PF and UKF for the orientation.

less than the error of the PF, the range ±10 mm was chosen.

4.6 Validation phase

The following experiment was carried out to validate the new localization algorithm (see Figure 4.12). The endoscope was fixed at a known position (our ground truth) by means of a mount. In this way, the EPM can move around the endoscope without changing its position. For each test, six positions were identified to place the EPM. For each position, the mean error of the estimated position relative to the ground truth and its standard deviation were calculated.

Considering that the localization algorithm is validated when the endoscope is in a fixed position, the tests that are performed are static. However, taking into account that under operational conditions the endoscope moves at very low speed, it is possible to approximate the operational situation as a sum of stationary points. For this reason, it is possible to validate the algorithm using a static test.

In all tests performed, the position of the endoscope is as presented in Table 4.6. This position, and all those presented later, are positions with respect to the global reference system (see Figure 2.12).

4.6.1 First test

As mentioned above, the EPM was placed in six different locations. The positions of the EPM, in the global reference system, can be found in Table 4.7, while their

Figure 4.12: Set-up of the validation experiment.

x [m]	y [m]	z [m]
0.650	-0.333	0.092

Table 4.6: Endoscope position (ground truth).

graphic representation, with respect to the position of the endoscope, can be found in Figure 4.13.

EPM position number	x [m]	y [m]	z [m]
1	0.573	-0.243	0.218
2	0.648	-0.243	0.218
3	0.722	-0.243	0.218
4	0.722	-0.267	0.208
5	0.648	-0.267	0.208
6	0.573	-0.267	0.208

Table 4.7: EPM position, first test.

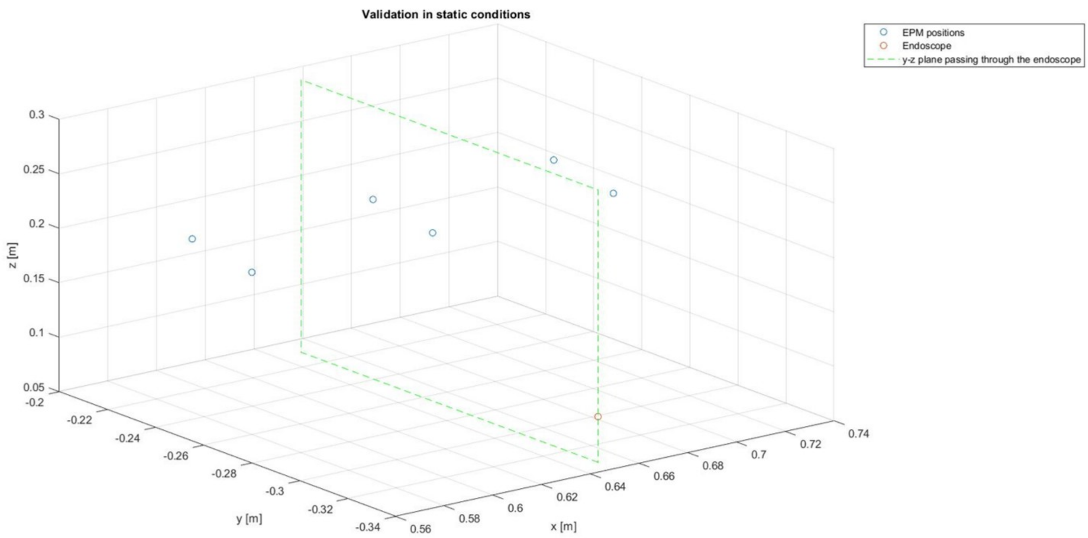

Figure 4.13: Positions of the endoscope and of the EPM, first test.

The mean error and its standard deviation between the estimation given by the PF and the UKF with respect to ground truth were calculated. The results obtained for each EPM position are shown in Tables 4.8 and 4.9.

EPM position number	Δx $[mm]$	Δy $[mm]$	Δz $[mm]$
1	1.53 ± 0.07	3.11 ± 0.13	1.28 ± 0.11
2	6.21 ± 0.06	2.54 ± 0.05	1.20 ± 0.06
3	8.80 ± 0.06	5.38 ± 0.14	4.40 ± 0.08
4	2.92 ± 0.20	6.97 ± 0.29	3.32 ± 0.18
5	4.09 ± 0.20	2.09 ± 0.04	4.37 ± 0.03
6	3.71 ± 0.11	5.35 ± 0.24	0.15 ± 0.10

Table 4.8: First test results for PF.

The average of the results obtained at the six points for the two algorithms is shown in Tables 4.10 and 4.11.

To better visualize the errors, the graph in Figure 4.14 was created. The results obtained with the UKF algorithm are comparable with those of the PF. Considering that the PF algorithm used is now employed by the company that implemented it to perform colonoscopy experiments on humans, and considering that the errors of the UKF are comparable with those of the PF, it can be concluded that the results obtained with the new localization algorithm (UKF) are excellent. In general, it

EPM position number	Δx $[mm]$	Δy $[mm]$	Δz $[mm]$
1	5.12 ± 0.67	3.54 ± 2.01	9.33 ± 2.06
2	0.70 ± 0.01	0.29 ± 0.19	6.73 ± 2.00
3	4.32 ± 2.73	11.63 ± 3.03	1.16 ± 0.88
4	2.27 ± 1.72	13.13 ± 2.20	7.85 ± 3.06
5	5.43 ± 0.15	0.12 ± 0.02	1.81 ± 0.04
6	3.87 ± 0.22	14.72 ± 0.91	4.11 ± 0.23

Table 4.9: First test results for UKF.

Δx $[mm]$	Δy $[mm]$	Δz $[mm]$
4.54 ± 0.12	4.24 ± 0.15	2.45 ± 0.09

Table 4.10: Overall results of the first test, for the PF.

Δx $[mm]$	Δy $[mm]$	Δz $[mm]$
3.62 ± 0.92	7.24 ± 1.39	5.17 ± 1.38

Table 4.11: Overall results of the first test, for the UKF.

can be said that the PF algorithm performed slightly better than the UKF, as is clear from the Figure 4.14.

The results obtained for PF are in line with those obtained by Taddese et al. [14]. The slight difference is due to the following reasons:

- the system used to perform the experiment is slightly different;
- the type of experiment is different, as in Taddese's experiment a second manipulator robot is used to hold the endoscopic capsule in a fixed position;
- in Taddese's experiment, the second robot is also used to precisely calculate the position of the endoscope (ground truth). In the validation experiment presented in this chapter, the ground truth was calculated manually and is therefore affected by a small uncertainty.

4.6.2 Second test

A second test was carried out to evaluate the performance of the new algorithm in the case of the endoscope being in the singularity plane of the EPM. The EPM was

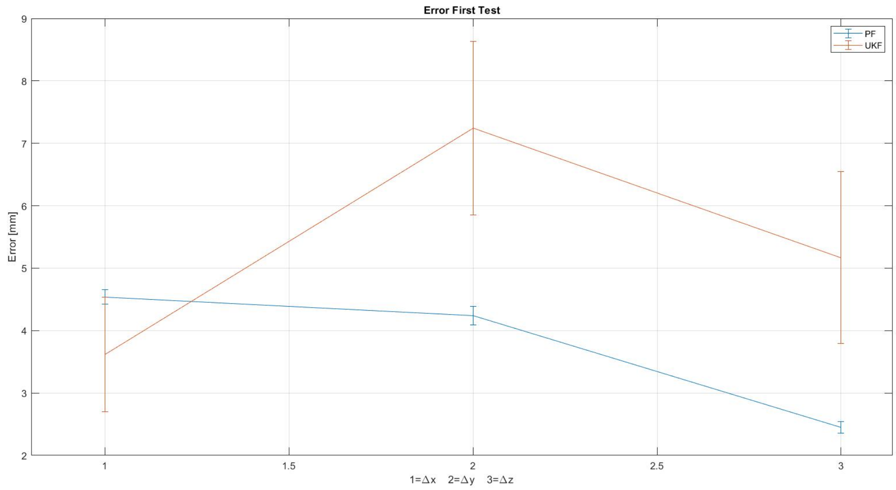

Figure 4.14: Error plot, first test.

then placed in six different points, and in each position its singularity plane passed through the endoscope. The positions of the EPM, in the global reference system, can be found in Table 4.12, while their graphic representation, with respect to the position of the endoscope, can be found in Figure 4.15.

EPM position number	x $[m]$	y $[m]$	z $[m]$
1	0.650	-0.333	0.207
2	0.650	-0.333	0.230
3	0.650	-0.333	0.253
4	0.650	-0.279	0.253
5	0.650	-0.279	0.230
6	0.650	-0.279	0.207

Table 4.12: EPM position, second test.

The mean error and its standard deviation between the estimation given by the PF and the UKF with respect to ground truth were calculated. The results obtained for each EPM position are shown in Tables 4.13 and 4.14.

The average of the results obtained at the six points for the two algorithms is shown in Tables 4.15 and 4.16.

To better visualize the errors, the graph in Figure 4.16 was created. The results obtained with the UKF algorithm are comparable with those of the PF. Again, the PF algorithm performed slightly better than the UKF.

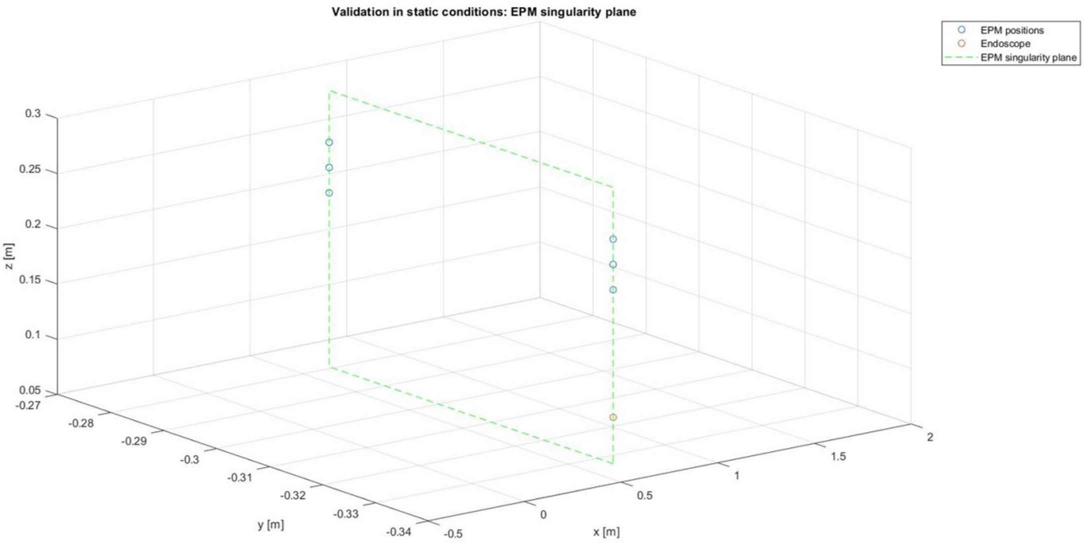

Figure 4.15: Positions of the endoscope and of the EPM, second test.

EPM position number	Δx $[mm]$	Δy $[mm]$	Δz $[mm]$
1	32.65 ± 1.67	2.34 ± 0.02	1.93 ± 0.46
2	26.38 ± 1.99	2.02 ± 0.03	0.37 ± 0.30
3	20.77 ± 1.32	1.78 ± 0.03	0.53 ± 0.16
4	8.78 ± 0.55	0.04 ± 0.03	5.10 ± 0.08
5	8.84 ± 0.61	0.31 ± 0.04	5.33 ± 0.06
6	11.74 ± 0.86	0.10 ± 0.07	5.44 ± 0.09

Table 4.13: Second test results for PF.

EPM position number	Δx $[mm]$	Δy $[mm]$	Δz $[mm]$
1	34.22 ± 3.31	2.36 ± 0.03	10.86 ± 2.44
2	34.43 ± 3.70	2.33 ± 0.01	8.38 ± 0.50
3	24.47 ± 3.17	1.92 ± 0.03	7.95 ± 2.57
4	13.73 ± 2.95	3.51 ± 0.40	3.16 ± 2.12
5	13.01 ± 3.03	3.55 ± 0.44	3.34 ± 1.39
6	8.86 ± 0.18	1.97 ± 0.01	2.34 ± 0.04

Table 4.14: Second test results for UKF.

Δx $[mm]$	Δy $[mm]$	Δz $[mm]$
18.19 ± 1.17	1.10 ± 0.04	3.12 ± 0.19

Table 4.15: Overall results of the second test, for the PF.

Δx $[mm]$	Δy $[mm]$	Δz $[mm]$
21.45 ± 2.72	2.61 ± 0.15	6.01 ± 1.51

Table 4.16: Overall results of the second test, for the UKF.

As expected, the error is increased compared to the previous test: along the x-direction, the error is about 2 cm for both algorithms. As demonstrated by Taddese et al. [14], from a theoretical point of view, the presence of the coil allows regions of singularity to be eliminated. In fact, by integrating an electromagnetic coil into the system that generates a weak time-varying magnetic field, and connecting it to the EPM such that their dipole moments are orthogonal, the two magnetic fields can be used simultaneously to obtain an additional set of equations that permit solving for the position and yaw angle of the capsule. Taddese et al. [14] have achieved excellent results even when the endoscope is in the plane of singularity of the EPM. The problem is that, in our case, the system used is different. Furthermore, uncertainties in the components used (magnets, sensors, magnetic field model, ...) make the real system different from the ideal one. All these factors influence the error. Finally, it must be remembered, as mentioned above, that the experiment performed is different. It can therefore be concluded that the high error in the x-direction, when the endoscope is in the singularity plane of the EPM, is due to the limitations of the system.

4.6.3 Consideration regarding orientation

Considering the type of testing done in the validation phase, it was not possible to calculate the error associated with the orientation estimation, as it was not possible to have a ground truth for the orientation. However, the error of the orientation estimated by the UKF versus that of the PF was calculated and the results (mean error and standard deviation) for all tests shown above are in Table 4.17.

Considering that the difference in the orientation estimation between the two algorithms is very small, it is possible to assume as results for the orientation of the UKF those obtained by Taddese et al. [14] for the PF.

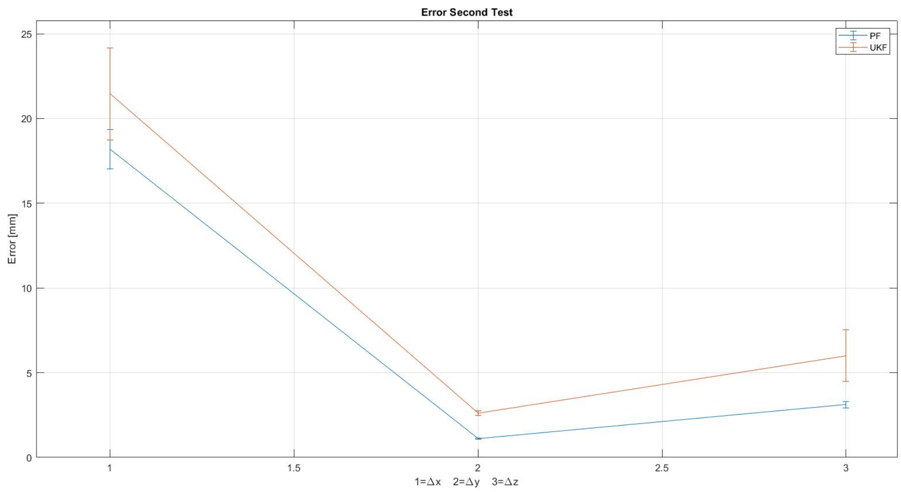

Figure 4.16: Error plot, second test.

$\Delta\phi$ [°]	$\Delta\theta$ [°]	$\Delta\psi$ [°]
0.00 ± 0.00	0.00 ± 0.00	4.11 ± 0.81

Table 4.17: UKF versus PF orientation error.

Chapter 5

Overall Localization Algorithm

As elaborated in the preceding chapter, the new localization algorithm (UKF) has demonstrated outcomes on par with the previous algorithm (PF). This implies that with the MFE system, the lower limit for localization error has probably been reached. The limit is therefore caused by the system itself and not by the localization algorithm.

The concluding phase of this project involves the fusion of the two developed algorithms, strategically extracting the strengths of each, in pursuit of a unified localization algorithm. This chapter will elucidate the process of merging the two algorithms and present the outcomes obtained during the validation experiment.

5.1 Combination of the two algorithms

As seen in the previous chapter, the results of the two algorithms are comparable, but in general the PF obtained slightly lower errors than the UKF. For this reason, the PF was used as the basis of the overall localization algorithm.

The UKF estimate is only used when the UKF gives better results than the PF. In general, when analyzing the performance of the variables estimated by the UKF, it was noted that the UKF gives excellent results, even better than the PF, when:

- is stable, i.e. when it is not continuously forced to be around the PF;
- the value of the estimated variable is close to that of the variable estimated by the PF, i.e., when the distance is less than or equal to 6 mm.

These two points are evident in Figures 5.1 and 5.2, which show the estimation of one of the state variables by the PF (blue line), the UKF (green line) versus ground truth (red line). From the figures, it can be seen that in these cases, the UKF's estimate is close to that of the PF, is very stable and in fact its error with respect to ground truth is lower than that of the PF.

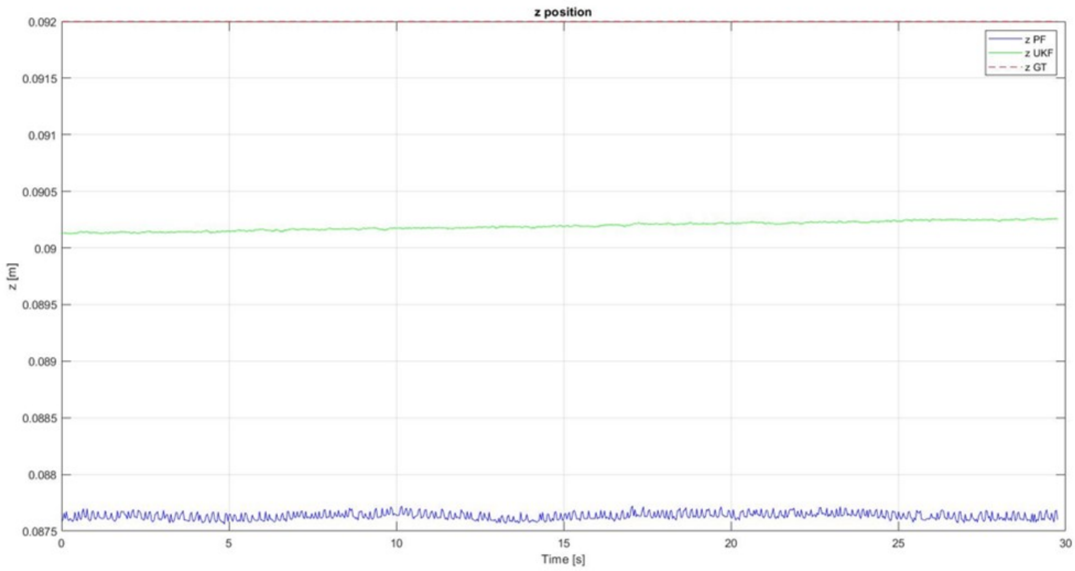

Figure 5.1: Position estimation along the z-direction; comparison between PF and UKF algorithms.

Both PF and UKF are therefore present in the overall localization algorithm. Both filters estimate the state, but, in general, the state estimated by the PF is used as the final state in the overall algorithm. However, if the UKF is stable and gives a result close to that of the PF (difference less than or equal to 6 mm), the state estimated by the UKF is used. From a practical point of view, in order to assess whether the estimate of the UKF is stable, a counter is implemented that decreases if the state variable under consideration is not forced to be in the proximity of the corresponding state variable of the PF. If this happens for a certain period of time, the counter goes below a certain threshold, and this means that the estimated variable is stable.

The code and the full explanation of the UKF localization algorithm implemented within the PF algorithm, including the choice of which of the two estimated states to use, can be found in Appendix B.

5.2 Validation experiment

The same validation experiment as in the previous chapter was carried out for the overall localization algorithm. The endoscope was fixed at a known position (our

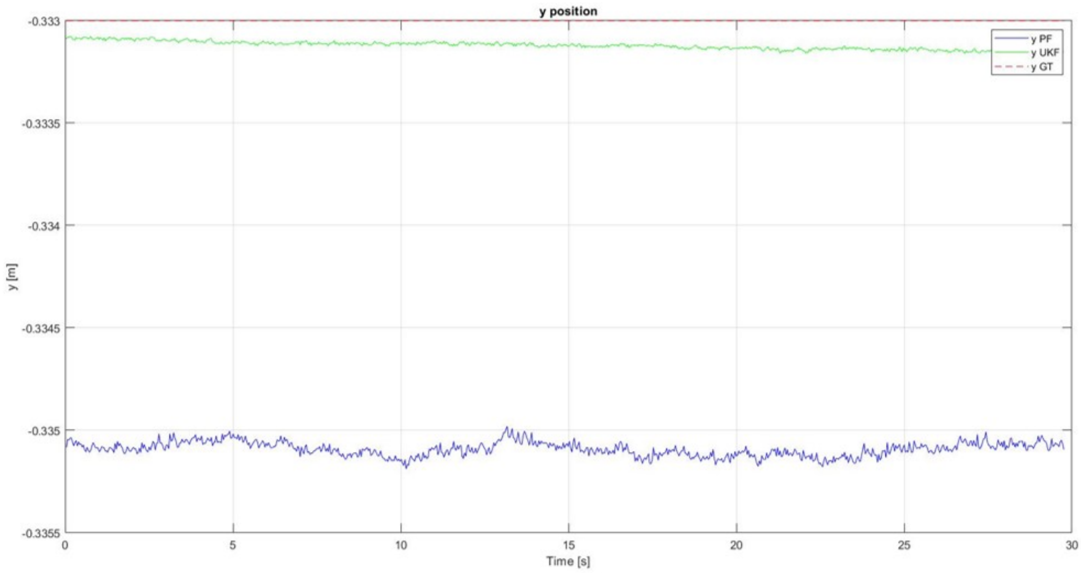

Figure 5.2: Position estimation along the y-direction; comparison between PF and UKF algorithms.

ground truth) by means of a mount. Six positions were identified to place the EPM. For each position, the mean error of the estimated position relative to the ground truth and its standard deviation were calculated. The position of the endoscope in the global reference system is as presented in Table 5.1.

x $[m]$	y $[m]$	z $[m]$
0.650	-0.333	0.092

Table 5.1: Endoscope position (ground truth).

The positions of the EPM in the global reference system are the same as in the first test of the previous chapter and can be found in Table 5.2, while their graphic representation, with respect to the position of the endoscope, can be found in Figure 5.3.

The mean error and its standard deviation of the estimation given by the overall algorithm with respect to ground truth were calculated. The results obtained for each EPM position are shown in Table 5.3.

The average of the results obtained in the six points by the overall algorithm is presented in Table 5.4 and is compared with the results obtained by the PF in the first test of the previous chapter.

EPM position number	x $[m]$	y $[m]$	z $[m]$
1	0.573	-0.243	0.218
2	0.648	-0.243	0.218
3	0.722	-0.243	0.218
4	0.722	-0.267	0.208
5	0.648	-0.267	0.208
6	0.573	-0.267	0.208

Table 5.2: EPM position, validation experiment.

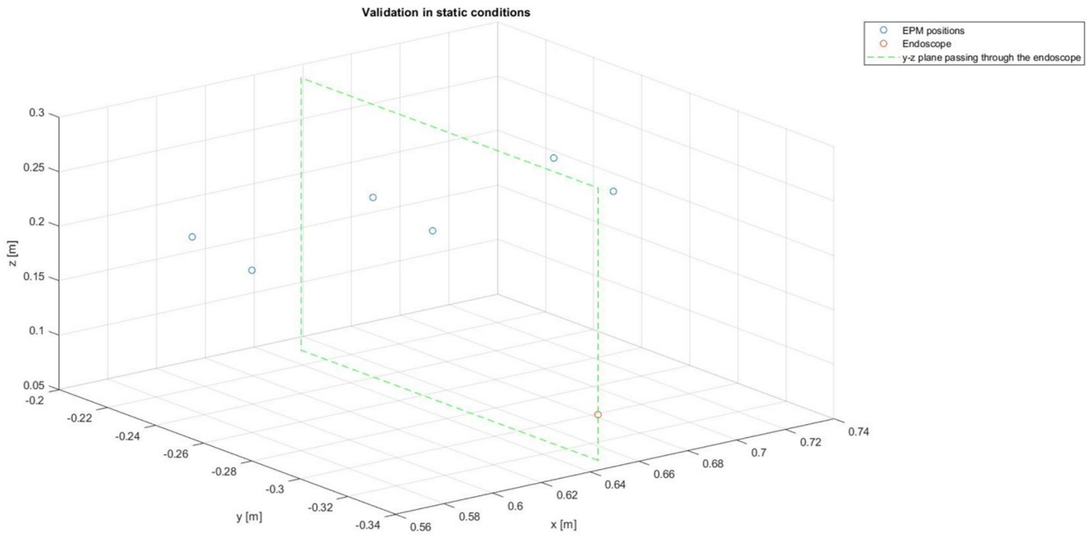

Figure 5.3: Positions of the endoscope and of the EPM, validation experiment.

EPM position number	Δx $[mm]$	Δy $[mm]$	Δz $[mm]$
1	0.47 ± 0.55	3.97 ± 0.31	3.45 ± 0.22
2	2.03 ± 0.70	1.00 ± 1.66	4.42 ± 0.04
3	1.03 ± 0.57	4.13 ± 1.39	0.27 ± 0.16
4	1.53 ± 0.20	0.61 ± 0.16	0.21 ± 0.13
5	6.81 ± 0.10	4.88 ± 0.01	1.35 ± 0.03
6	7.11 ± 0.72	1.97 ± 0.26	5.22 ± 0.59

Table 5.3: Validation experiment results.

Algorithm type	Δx $[mm]$	Δy $[mm]$	Δz $[mm]$
Overall algorithm	3.16 ± 0.47	2.76 ± 0.63	2.49 ± 0.20
PF (first test, previous chapter)	4.54 ± 0.12	4.24 ± 0.15	2.45 ± 0.09

Table 5.4: Comparison of the results obtained from the overall algorithm and from the PF algorithm.

To better visualize the errors, the graph in Figure 5.4 was created. As is clear from both the figure and the table, the overall algorithm's results exhibit a slight improvement over those obtained with the PF alone. This leads to the conclusion that by harnessing the combined capabilities of both the PF and the UKF, it becomes feasible to enhance the localization beyond what can be achieved solely with the PF.

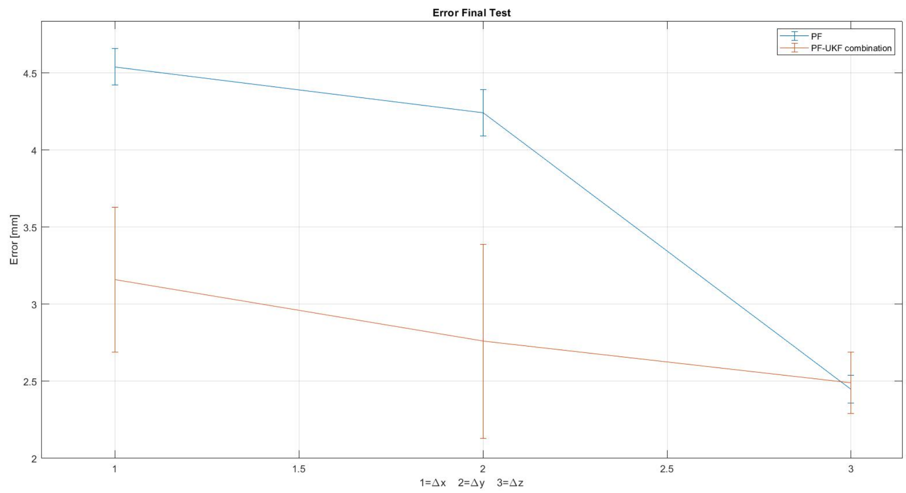

Figure 5.4: Error plot, comparison of the results obtained from the overall algorithm and from the PF algorithm.

Chapter 6

Future Works and Conclusion

6.1 Future works

Given that the errors resulting from both localization algorithms, PF and UKF, are comparable, it is possible to state that the lower limit of error has been attained and is fundamentally contingent on the system's intrinsic characteristics.

In pursuit of refining localization, any attempts to achieve further enhancements would necessitate altering the system. Two prospective avenues for future development are as follows:

1. changing the position of the coil;
2. using an external magnetic sensor array.

Regarding the position of the coil, it could be considered to put the coil in a fixed position (e.g., on the robot cart). The main benefits of this development are the following two:

- no power is brought into the robot, and it also avoids putting electronics in the robot;
- there is no permanent magnet inside the coil and, therefore, no noise.

As a secondary consequence, the end effector is much simpler and can be disassembled more easily. This solution would therefore certainly improve the product. However, it would need to be assessed how the localization changes. In the solution of Taddese et al. [14], the magnetic fields of the coil and of the EPM are always orthogonal, and this allows the solution of problems in the singularity plane of the

EPM. If, on the other hand, the coil is in a fixed position, it is possible for the two magnetic fields to align, and, if this happens in the singularity plane of the EPM, the number of equations to solve the inverse problem is reduced, and thus the singularity problem persists. In order to implement this proposal, it is first necessary to assess how the accuracy of localization changes with the new system and eventually make changes to the localization algorithm.

The use of an external magnetic sensor array will be explained in detail in the next section.

6.1.1 Localization using an external magnetic sensor array

Li et al. [28] present a groundbreaking localization approach for active capsule endoscopy, which uniquely merges external magnetic field sensing and internal inertial sensing. This innovative combination enables the accurate 6-DOF pose estimation of a magnetic capsule robot for the first time. The method integrates an inertial measurement unit within the capsule, coupled with an external magnetic sensor array, to achieve precise and real-time localization without the need for complex capsule structures, actuator modifications, or the implementation of specific motions of the magnets. Consequently, this technique facilitates accurate and efficient capsule localization within a vast workspace.

Figure 6.1 shows the solution implemented by Li et al. [28]. The procedure begins with the patient swallowing a capsule, followed by positioning on an examination bed that features a large sensor array. Adjacent to the bed, a robotic arm equipped with an actuator, comprising a motor and a spherical magnet, is employed. This actuator rotates over the capsule, which houses a magnetic ring for propelling it using an adaptive strategy. Simultaneously, real-time tracking of the capsule is achieved through an optimally activated subarray of sensors.

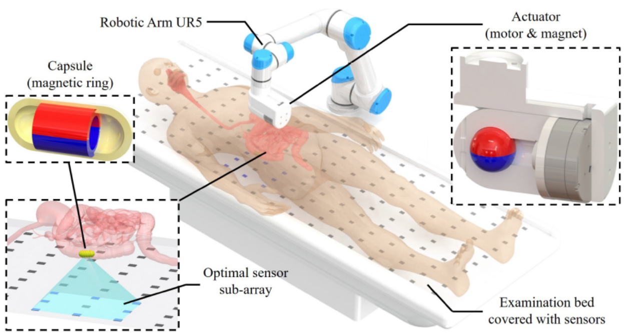

Figure 6.1: Overall design of the system implemented by Li et al. [28] and its application scenario [29].

The sensor array, shown in Figure 6.2, makes it possible to calculate the magnetic field, which is the sum of the magnetic field of the capsule, of the actuator, and of the Earth. Thus, by subtracting the actuator and Earth magnetic field from the total magnetic field, the magnetic field of the capsule can be found. At this point, the difference between the capsule's measured and theoretical magnetic fields can be minimized to find the position and yaw angle. To uniquely determine the position of the capsule, at least two sensors are needed, as shown in Figure 6.2.b.

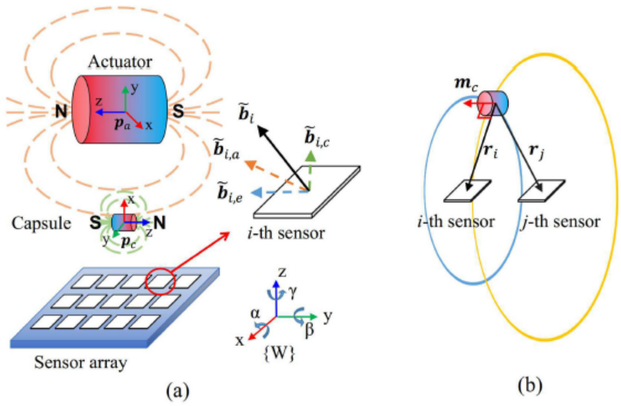

Figure 6.2: (a) Illustration of the localization model. (b) Illustration of the singularity of position estimation [28].

This solution could lead to an improvement in localization. The main problem is that for this development, the MFE system would have to be changed considerably, and therefore a lot of time is required for its implementation.

6.2 Conclusion

Colorectal cancer stands as a significant global health concern, ranking as the third most prevalent malignancy and the second most deadly cancer. Early detection of cancer plays a pivotal role in improving the chances of survival, and colonoscopy stands as one of the most prevalent screening procedures. The STORM Lab team developed an innovative Magnetic Flexible Endoscopy system, that play a crucial role in clinical investigations and research studies pertaining to the navigation and examination of the human colon, specifically in the context of colonoscopy. Accurate estimation of the capsule's pose is crucial for magnetic actuation systems to effectively apply the required forces and torques. For this reason, a localization algorithm (Particle Filter algorithm) was implemented by STORM Lab.

In this work, two parameters, ESS and WD, were developed and combined in order to determine the real-time accuracy of the localization algorithm. This investigation was carried out for the following reasons: drift phenomena rarely occur; calibration errors may happen; the PF algorithm lacks elements to determine whether the estimate made is accurate. The combination of the two parameters was tested in seven different scenarios, and the results obtained in the validation phase make it possible to state that the accuracy of localization can be determined in real-time using these parameters. Subsequently, a novel localization algorithm was developed using the Unscented Kalman Filter. The outcomes yielded by this algorithm are comparable with those obtained using the PF algorithm. In a strategic fusion, the UKF and PF algorithms were integrated to harness the strengths of each, culminating in final errors that are lower than those arising from the PF algorithm alone. This leads to the conclusion that by harnessing the combined capabilities of both the PF and the UKF, it becomes feasible to enhance the localization beyond what can be achieved solely with the PF.

Bibliography

[1] Yue Xi and Pengfei Xu. «Global colorectal cancer burden in 2020 and projections to 2040.» In: *Translational oncology* 14.10 (2021) (cit. on p. 2).

[2] Kimberly D. Miller et al. «Cancer treatment and survivorship statistics, 2016.» In: *CA: a cancer journal for clinicians* 66.4 (2016), pp. 271–289 (cit. on p. 2).

[3] Ahmedin Jemal et al. «Global patterns of cancer incidence and mortality rates and trends.» In: *Cancer epidemiology, biomarkers & prevention* 19.8 (2010), pp. 1893–1907 (cit. on p. 2).

[4] Lindsey A. Torre et al. «Global cancer statistics, 2012.» In: *CA: a cancer journal for clinicians* 65.2 (2015), pp. 87–108 (cit. on p. 2).

[5] Luca Audino. *Design and development of a real-time localisation algorithm for the magnetic manipulation of the Magnetic Flexible Endoscope.* Politecnico di Torino, 2020 (cit. on pp. 3, 10–12, 56).

[6] Shalanda A. Bynum et al. «Unwillingness to participate in colorectal cancer screening: examining fears, attitudes, and medical mistrust in an ethnically diverse sample of adults 50 years and older.» In: *American journal of health promotion* 26.5 (2012), pp. 295–300 (cit. on p. 3).

[7] Levin J. Sliker and Gastone Ciuti. «Flexible and capsule endoscopy for screening, diagnosis and treatment.» In: *Expert review of medical devices* 11.6 (2014), pp. 649–666 (cit. on p. 3).

[8] Piotr R. Slawinski et al. «Emerging issues and future developments in capsule endoscopy.» In: 17.1 (2015), pp. 40–46 (cit. on p. 3).

[9] Addisu Zerihun Taddese. *Magnetic Pose Estimation and Robotic Manipulation of Magnetically Actuated Capsule Endoscopes.* Vanderbilt University, 2018 (cit. on pp. 4, 22).

[10] Chao Hu et al. «A cubic 3-axis magnetic sensor array for wirelessly tracking magnet position and orientation.» In: *IEEE Sensors Journal* 10.5 (2010), pp. 903–913 (cit. on pp. 5, 6).

[11] Chao Hu et al. «Locating intra-body capsule object by three-magnet sensing system.» In: *IEEE sensors journal* 16.13 (2016), pp. 5167–5176 (cit. on pp. 5, 6).

[12] Anton Plotkin et al. «A new calibration procedure for magnetic tracking systems.» In: *IEEE Transactions on Magnetics* 44.11 (2008), pp. 4525–4528 (cit. on pp. 5, 6).

[13] Mehmet Turan et al. «A deep learning based 6 degree-of-freedom localization method for endoscopic capsule robots.» In: *arXiv preprint* arXiv:1705.05435 (2017) (cit. on pp. 5, 6).

[14] Addisu Zerihun Taddese et al. *Enhanced real-time pose estimation for closed-loop robotic manipulation of magnetically actuated capsule endoscopes.* Vol. 37.8. The International journal of robotics research, 2018, pp. 890–911 (cit. on pp. 5–7, 13, 14, 17–21, 29, 50, 56–58, 60, 65, 69, 72, 79).

[15] Federico Bianchi et al. «Localization strategies for robotic endoscopic capsules: a review.» In: *Expert review of medical devices* 16.5 (2019), pp. 381–403 (cit. on p. 6).

[16] Katie M. Popek et al. *Localization method for a magnetic capsule endoscope propelled by a rotating magnetic dipole field.* IEEE International Conference on Robotics and Automation, 2013 (cit. on pp. 5, 6).

[17] Christian Di Natali et al. «Real-time pose detection for magnetic medical devices.» In: *IEEE Transactions on Magnetics* 49.7 (2013), pp. 3524–3527 (cit. on p. 12).

[18] Christian Di Natali et al. «Jacobian-based iterative method for magnetic localization in robotic capsule endoscopy.» In: *IEEE Transactions on Robotics* 32.2 (2016), pp. 327–338 (cit. on p. 12).

[19] Gerald Goertzel. «An algorithm for the evaluation of finite trigonometric series.» In: *American Math. Monthly* 65 (1958), pp. 34–35 (cit. on p. 14).

[20] Clay S. Turner. «Recursive discrete-time sinusoidal oscillators.» In: *IEEE Signal Processing Magazine* 20.3 (2003), pp. 103–111 (cit. on p. 14).

[21] Manon Kok et al. «Using inertial sensors for position and orientation estimation.» In: *arXiv preprint* arXiv:1704.06053 (2017) (cit. on p. 15).

[22] Mark Euston et al. «A complementary filter for attitude estimation of a fixed-wing UAV.» In: *IEEE/RSJ international conference on intelligent robots and systems* (2008) (cit. on p. 15).

[23] Timothy D. Barfoot. *State estimation for robotics.* Cambridge University Press, 2022 (cit. on pp. 22, 23).

[24] Simon J. Julier and Jeffrey K. Uhlmann. «New extension of the Kalman filter to nonlinear systems.» In: *Signal processing, sensor fusion, and target recognition VI* Vol. 3068. Spie (1997) (cit. on p. 25).

[25] Eric A. Wan and Rudolph Van Der Merwe. «The unscented Kalman filter for nonlinear estimation.» In: *Proceedings of the IEEE 2000 Adaptive Systems for Signal Processing, Communications, and Control Symposium* Cat. No. 00EX373 (2000) (cit. on p. 25).

[26] R. V. D. Merwe and Eric Wan. «Sigma-point Kalman filters for probabilistic inference in dynamic state-space models.» In: *Diss. PhD Thesis, the faculty of the OGI School of Science & Engineering at Oregon Health & Science University* (2004) (cit. on pp. 27, 28).

[27] Norman Derby and Stanislaw Olbert. «Cylindrical magnets and ideal solenoids.» In: *American Journal of Physics* 78.3 (2010), pp. 229–235 (cit. on p. 58).

[28] Keyu Li et al. «External and internal sensor fusion based localization strategy for 6-dof pose estimation of a magnetic capsule robot.» In: *IEEE Robotics and Automation Letters* 7.3 (2022), pp. 6878–6885 (cit. on pp. 80, 81).

[29] Yangxin Xu et al. «Adaptive simultaneous magnetic actuation and localization for WCE in a tubular environment.» In: *IEEE Transactions on Robotics* 38.5 (2022), pp. 2812–2826 (cit. on p. 80).

Appendix A

Real-time Estimation of Localization Correctness

A.1 Test phase

A.1.1 Threshold evaluation

After identifying different thresholds for each indicator, the points exceeding the threshold for each scenario are calculated. The results are depicted in the following figures. The total number of points for a test is about 530/600.

	Test Number	Test Name	ESS_lower_th1 (th = 1500)	ESS_lower_th2 (th = 2000)	ESS_lower_th3 (th = 2500)	ESS_increase_above_th1 (th = 500)	ESS_increase_above_th2 (th = 550)	ESS_increase_above_th3 (th = 600)
1	1	1 Stationary Situation – No Singularity	0	0	0	0	0	0
	2	2 Stationary Situation – No Singularity	0	0	0	0	0	0
	3	3 Stationary Situation – No Singularity	0	0	0	0	0	0
2	4	1 Stationary Situation – Singularity Plane	0	0	0	46	17	5
	5	2 Stationary Situation – Singularity Plane	0	0	1	61	30	21
	6	3 Stationary Situation – Singularity Plane	0	0	0	53	26	12
3	7	1 Coil Off – No Singularity	0	0	0	1	0	0
	8	2 Coil Off – No Singularity	0	0	0	0	0	0
	9	3 Coil Off – No Singularity	0	0	0	1	0	0
4	10	1 Coil Off – Singularity Plane	0	0	0	237	232	228
	11	2 Coil Off – Singularity Plane	0	0	0	259	254	248
	12	3 Coil Off – Singularity Plane	0	0	0	262	255	248
5	13	1 Endoscope Outside The Workspace	41	46	48	101	98	93
	14	2 Endoscope Outside The Workspace	40	46	55	183	178	171
	15	3 Endoscope Outside The Workspace	44	46	49	39	36	32
6	16	1 Joystick Movement	8	11	13	46	40	37
	17	2 Joystick Movement	9	13	19	71	67	61
	18	3 Joystick Movement	12	12	14	70	67	63
7	19	1 Wrong Calibration	452	520	548	117	103	97
	20	2 Wrong Calibration	256	295	370	164	150	142
	21	3 Wrong Calibration	407	451	485	225	216	206

Figure A.1: Results for the *ESS* parameter.

	Test Number	Test Name	WD_above_th1 (th = 0,014)	WD_above_th2 (th = 0,016)	WD_above_th3 (th = 0,018)	WD_increase_above_th1 (th = 0,005)	WD_increase_above_th2 (th = 0,008)	WD_increase_above_th3 (th = 0,012)
1	1	1 Stationary Situation – No Singularity	0	0	0	24	1	0
	2	2 Stationary Situation – No Singularity	0	0	0	0	0	0
	3	3 Stationary Situation – No Singularity	0	0	0	0	0	0
2	4	1 Stationary Situation – Singularity Plane	13	4	1	61	17	0
	5	2 Stationary Situation – Singularity Plane	11	4	3	46	12	2
	6	3 Stationary Situation – Singularity Plane	11	4	1	61	17	0
3	7	1 Coil Off – No Singularity	0	0	0	11	2	0
	8	2 Coil Off – No Singularity	0	0	0	7	2	0
	9	3 Coil Off – No Singularity	0	0	0	10	0	0
4	10	1 Coil Off – Singularity Plane	33	23	16	47	25	15
	11	2 Coil Off – Singularity Plane	37	30	21	60	28	9
	12	3 Coil Off – Singularity Plane	58	44	37	65	31	12
5	13	1 Endoscope Outside The Workspace	390	374	367	223	144	96
	14	2 Endoscope Outside The Workspace	263	219	194	176	95	46
	15	3 Endoscope Outside The Workspace	150	144	134	81	59	36
6	16	1 Joystick Movement	10	5	0	19	6	0
	17	2 Joystick Movement	26	19	14	29	8	1
	18	3 Joystick Movement	7	3	3	25	6	0
7	19	1 Wrong Calibration	0	0	0	3	0	0
	20	2 Wrong Calibration	0	0	0	4	0	0
	21	3 Wrong Calibration	0	0	0	1	0	0

Figure A.2: Results for the WD parameter.

	Test Number	Test Name	WD2_above_th1 (th = 0,00015)	WD2_above_th2 (th = 0,0002)	WD2_above_th3 (th = 0,00025)	WD2_lower_th1 (th = 5,5*10^-6)	WD2_lower_th2 (th = 5*10^-6)	WD2_lower_th3 (th = 4,5*10^-6)	WD2_increase_above_th1 (th = 3*10^-5)	WD2_increase_above_th2 (th = 3,5*10^-5)	WD2_increase_above_th3 (th = 4*10^-5)
1	1	1 Stationary Situation – No Singularity	0	0	0	8	6	5	95	70	50
	2	2 Stationary Situation – No Singularity	0	0	0	461	451	429	0	0	0
	3	3 Stationary Situation – No Singularity	0	0	0	112	93	74	0	0	0
2	4	1 Stationary Situation – Singularity Plane	10	5	0	6	5	2	208	176	157
	5	2 Stationary Situation – Singularity Plane	7	5	2	1	1	1	156	127	107
	6	3 Stationary Situation – Singularity Plane	7	5	1	207	175	163	80	16	1
3	7	1 Coil Off – No Singularity	0	0	0	230	226	220	33	26	23
	8	2 Coil Off – No Singularity	0	0	0	95	88	75	32	26	18
	9	3 Coil Off – No Singularity	0	0	0	12	11	8	43	28	22
4	10	1 Coil Off – Singularity Plane	38	24	18	7	6	4	125	103	89
	11	2 Coil Off – Singularity Plane	44	31	27	6	4	4	164	142	124
	12	3 Coil Off – Singularity Plane	68	45	33	5	4	3	155	138	127
5	13	1 Endoscope Outside The Workspace	377	375	353	8	6	5	431	411	399
	14	2 Endoscope Outside The Workspace	234	220	186	4	4	3	368	351	329
	15	3 Endoscope Outside The Workspace	145	145	115	215	157	103	146	143	140
6	16	1 Joystick Movement	6	6	0	39	24	19	48	43	35
	17	2 Joystick Movement	26	20	11	16	14	12	74	64	58
	18	3 Joystick Movement	8	4	2	27	20	14	61	52	47
7	19	1 Wrong Calibration	0	0	0	441	405	378	3	2	2
	20	2 Wrong Calibration	0	0	0	417	404	388	1	0	0
	21	3 Wrong Calibration	0	0	0	430	416	392	9	4	1

Figure A.3: Results for the $WD2$ parameter.

A.1.2 Single-point analysis

Below are depicted the plots of the two indicators for the tests not shown above.

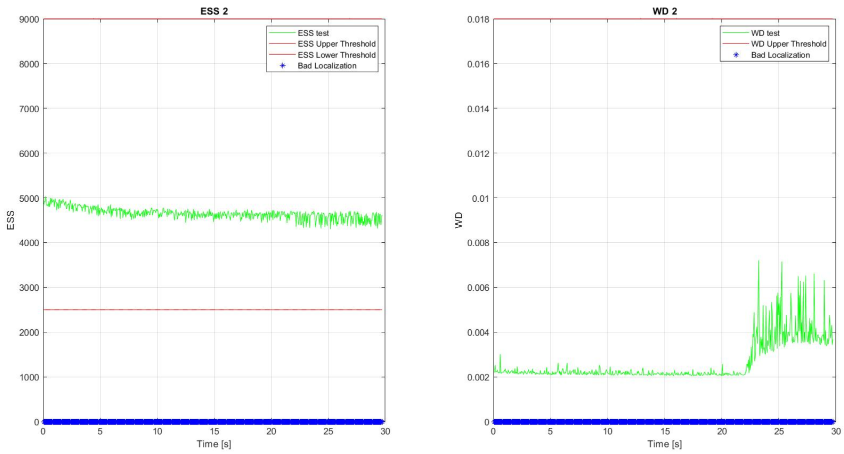

Figure A.4: Stationary situation – No singularity: ESS and WD parameters, test 2.

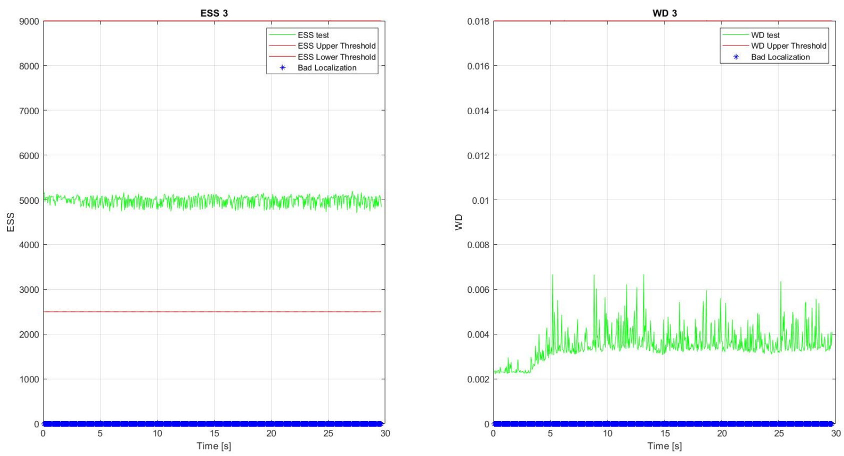

Figure A.5: Stationary situation – No singularity: ESS and WD parameters, test 3.

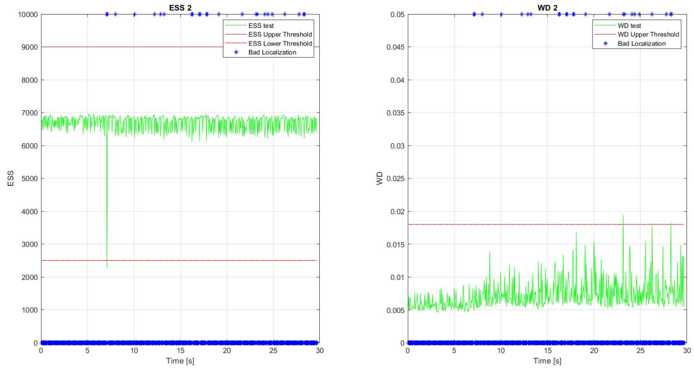

Figure A.6: Stationary situation – Singularity plane: ESS and WD parameters, test 2.

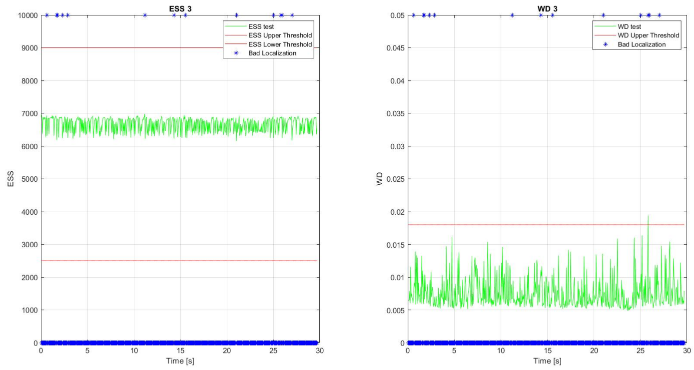

Figure A.7: Stationary situation – Singularity plane: ESS and WD parameters, test 3.

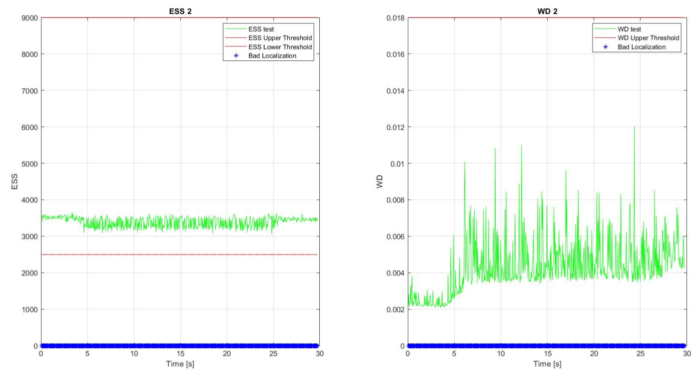

Figure A.8: Coil off – No singularity: ESS and WD parameters, test 2.

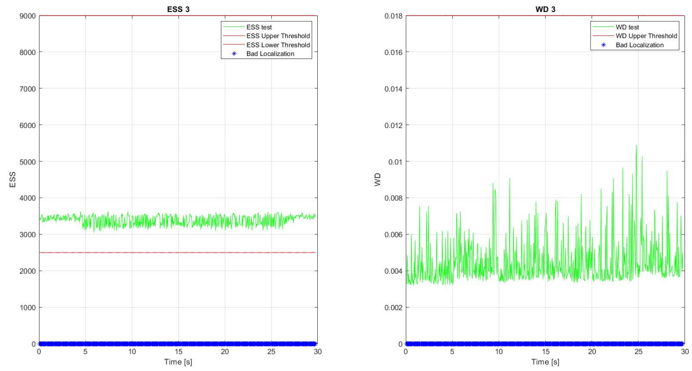

Figure A.9: Coil off – No singularity: ESS and WD parameters, test 3.

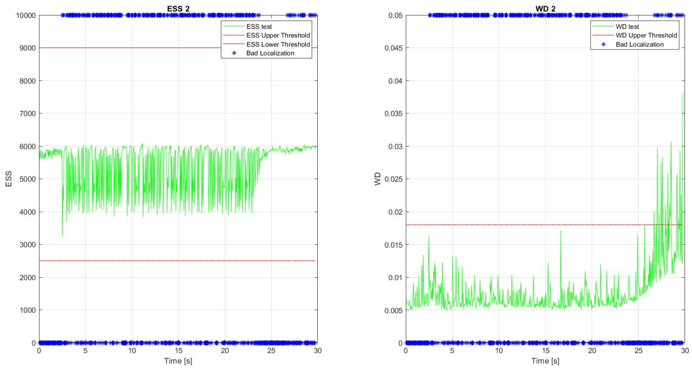

Figure A.10: Coil off – Singularity plane: ESS and WD parameters, test 2.

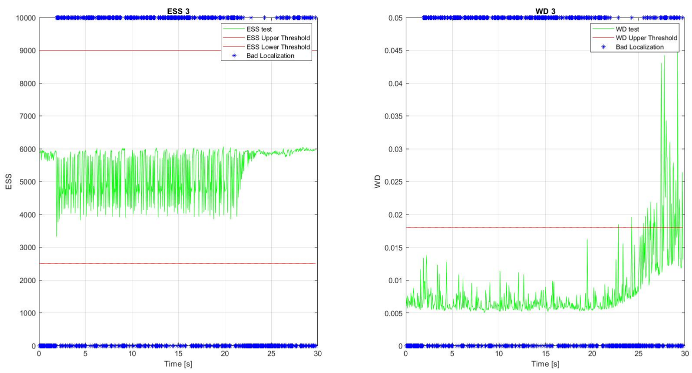

Figure A.11: Coil off – Singularity plane: ESS and WD parameters, test 3.

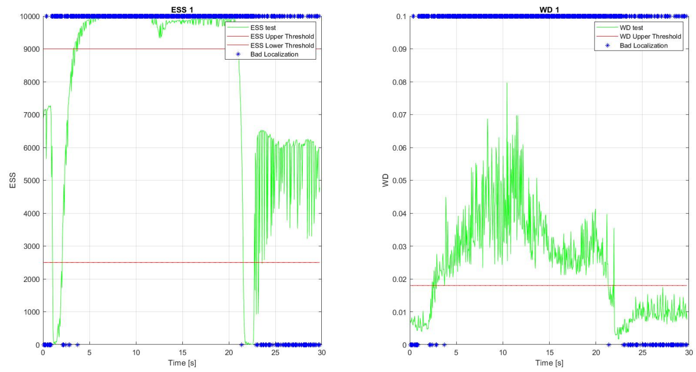

Figure A.12: Endoscope outside the workspace: ESS and WD parameters, test 1.

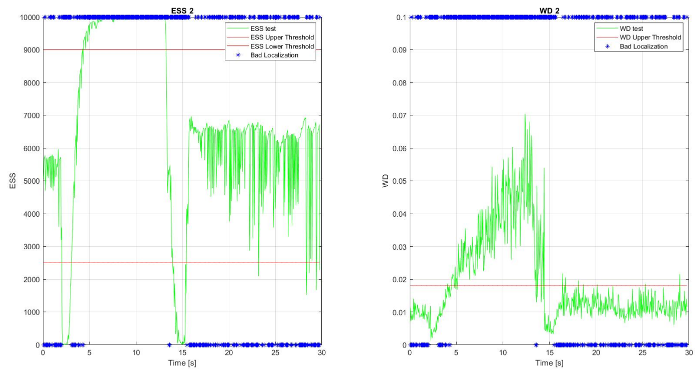

Figure A.13: Endoscope outside the workspace: ESS and WD parameters, test 2.

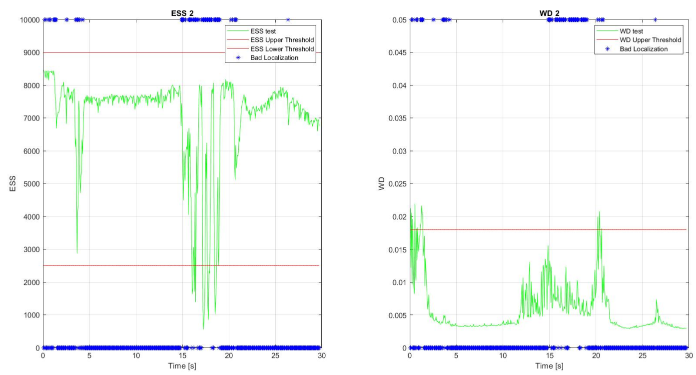

Figure A.14: Joystick movement: ESS and WD parameters, test 2.

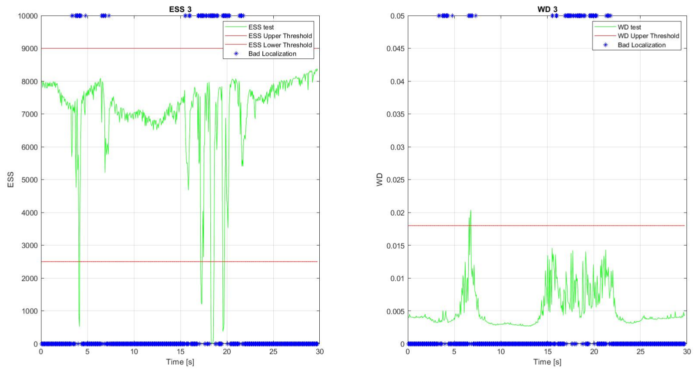

Figure A.15: Joystick movement: ESS and WD parameters, test 3.

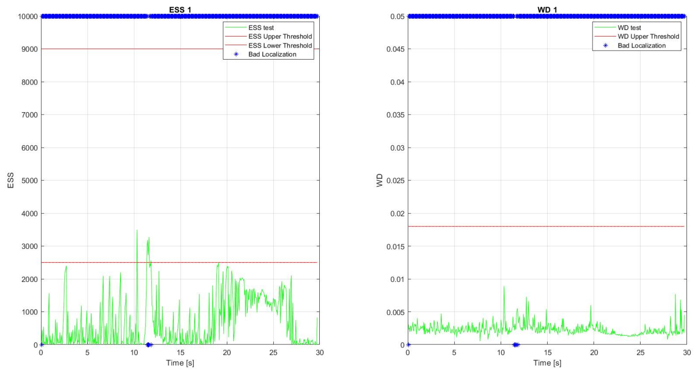

Figure A.16: Wrong calibration: ESS and WD parameters, test 1.

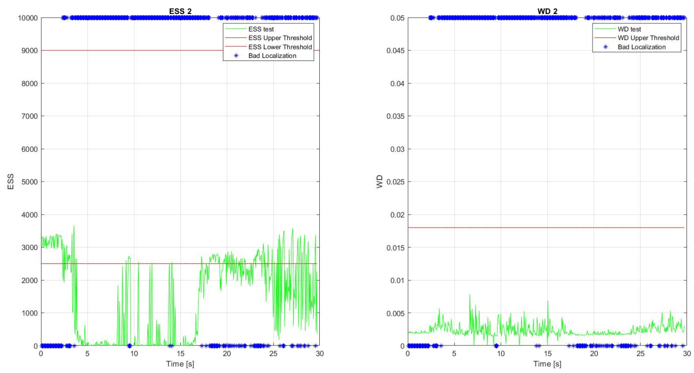

Figure A.17: Wrong calibration: ESS and WD parameters, test 2.

A.1.3 Low-pass filter analysis

Below are depicted the plots of the two indicators for the tests not shown above.

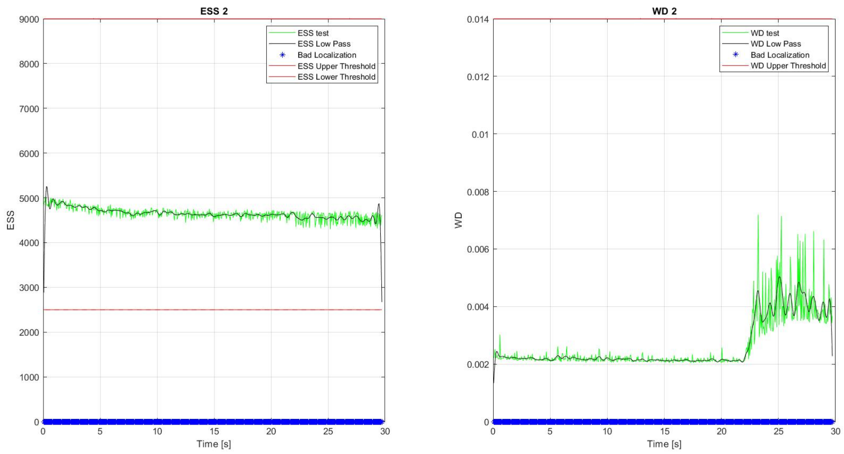

Figure A.18: Stationary situation – No singularity: ESS and WD parameters, test 2.

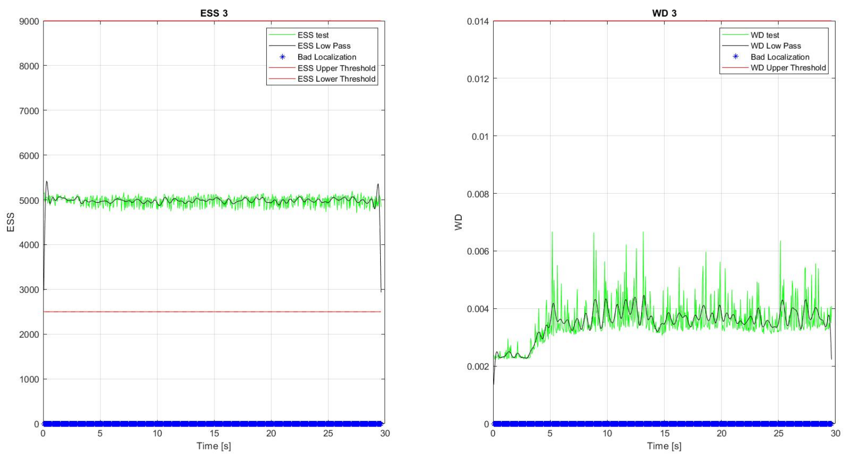

Figure A.19: Stationary situation – No singularity: ESS and WD parameters, test 3.

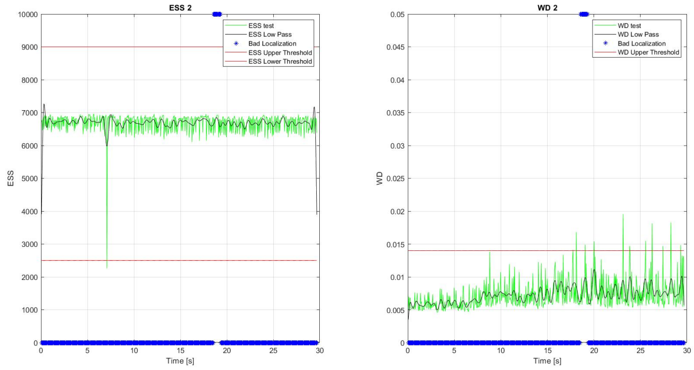

Figure A.20: Stationary situation – Singularity plane: ESS and WD parameters, test 2.

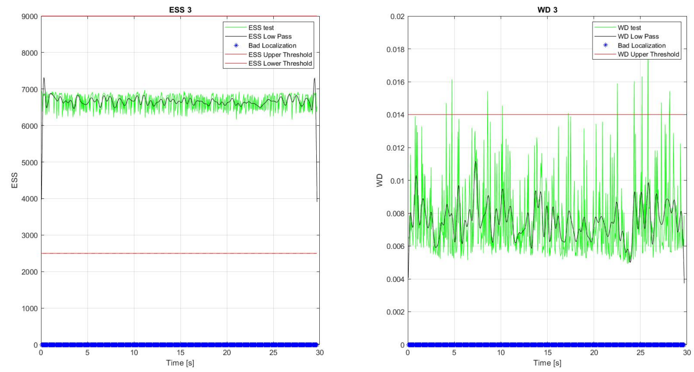

Figure A.21: Stationary situation – Singularity plane: ESS and WD parameters, test 3.

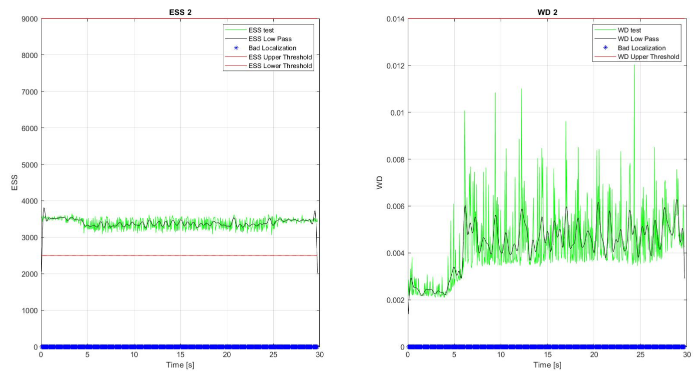

Figure A.22: Coil off – No singularity: ESS and WD parameters, test 2.

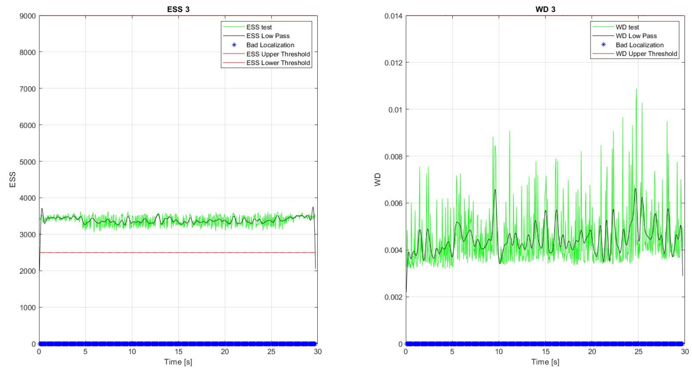

Figure A.23: Coil off – No singularity: ESS and WD parameters, test 3.

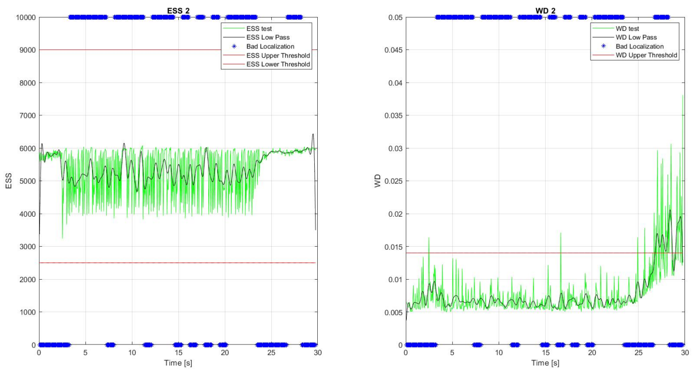

Figure A.24: Coil off – Singularity plane: ESS and WD parameters, test 2.

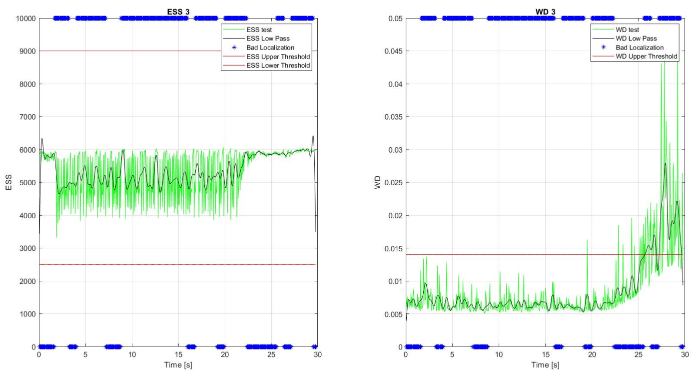

Figure A.25: Coil off – Singularity plane: ESS and WD parameters, test 3.

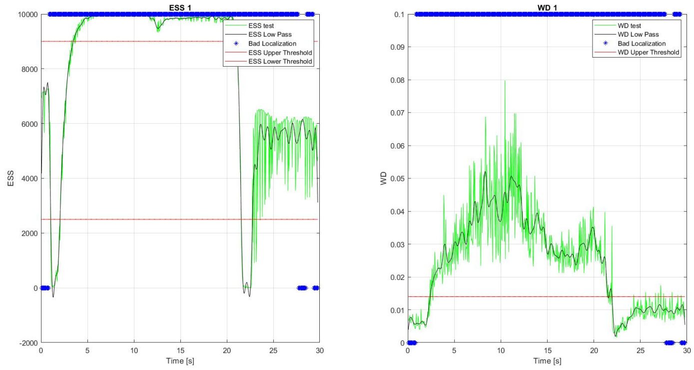

Figure A.26: Endoscope outside the workspace: ESS and WD parameters, test 1.

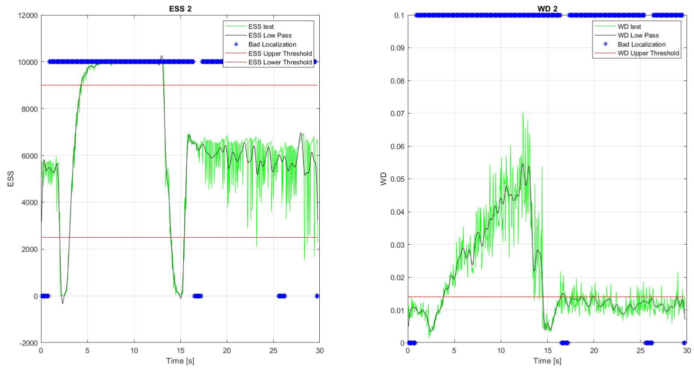

Figure A.27: Endoscope outside the workspace: ESS and WD parameters, test 2.

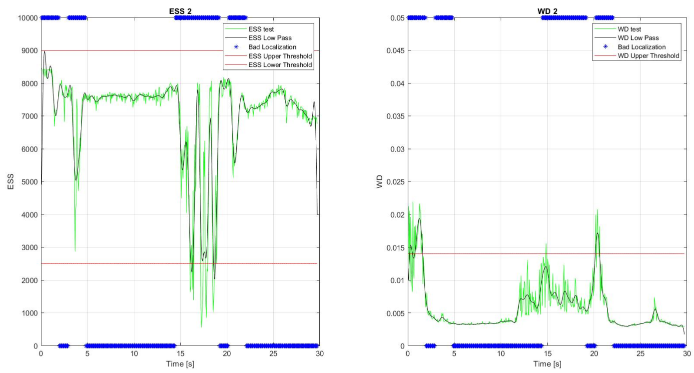

Figure A.28: Joystick movement: ESS and WD parameters, test 2.

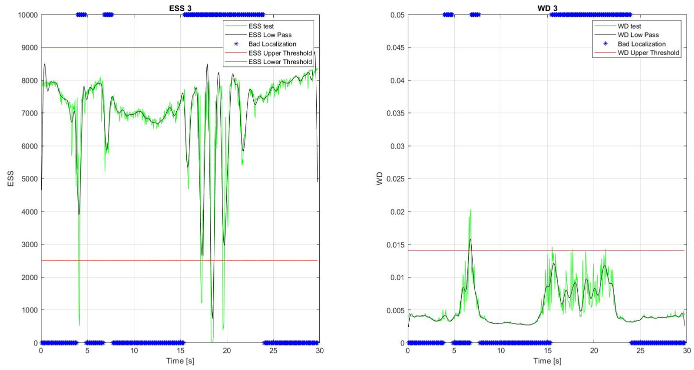

Figure A.29: Joystick movement: ESS and WD parameters, test 3.

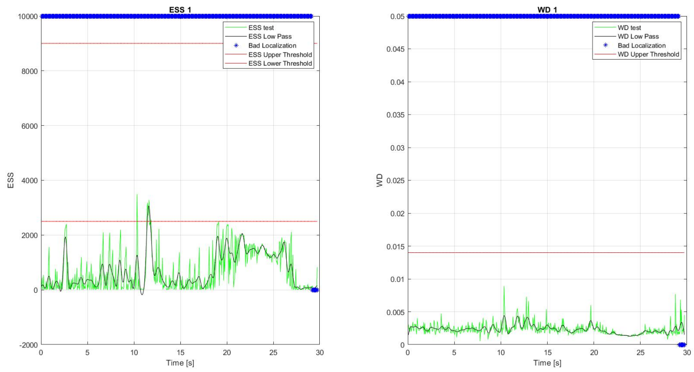

Figure A.30: Wrong calibration: ESS and WD parameters, test 1.

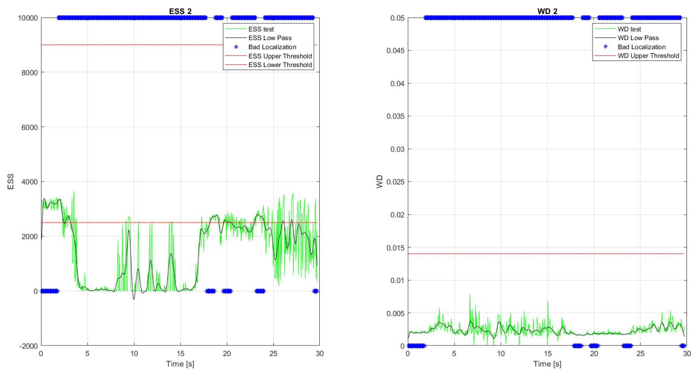

Figure A.31: Wrong calibration: ESS and WD parameters, test 2.

A.1.4 Analysis of sets of points (without filter)

Below are depicted the plots of the two indicators for the tests not shown above.

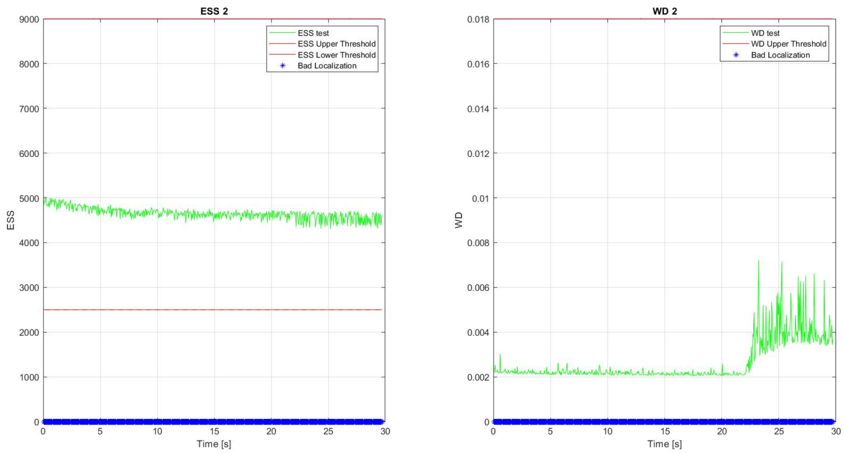

Figure A.32: Stationary situation – No singularity: ESS and WD parameters, test 2.

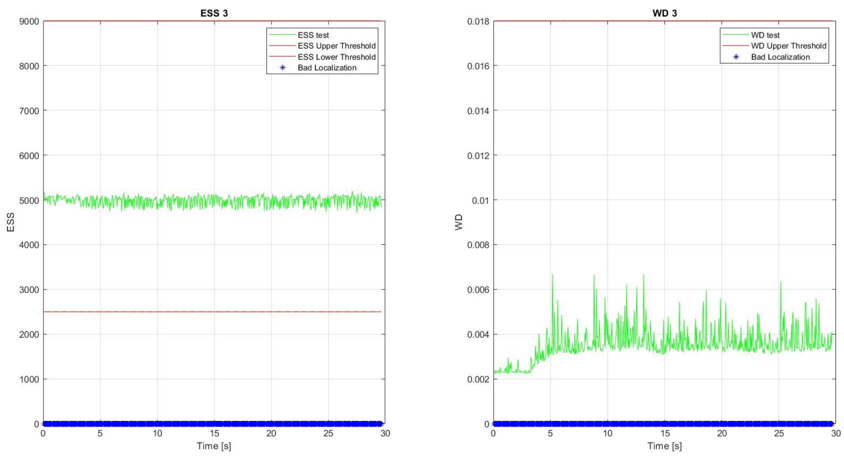

Figure A.33: Stationary situation – No singularity: ESS and WD parameters, test 3.

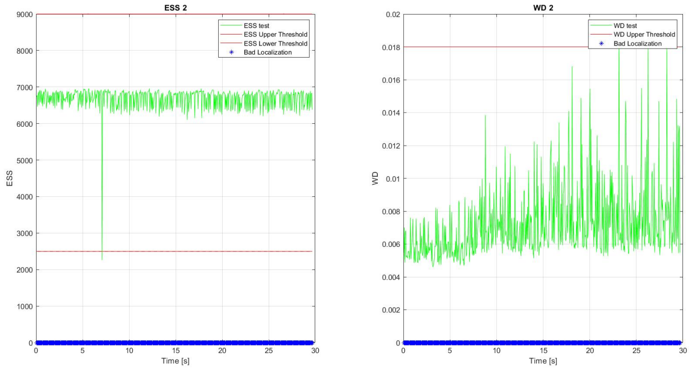

Figure A.34: Stationary situation – Singularity plane: ESS and WD parameters, test 2.

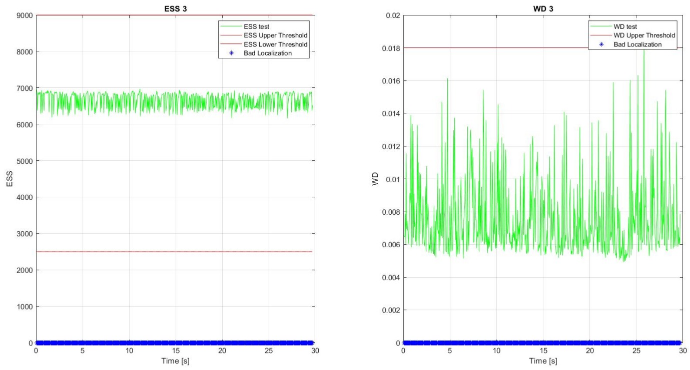

Figure A.35: Stationary situation – Singularity plane: ESS and WD parameters, test 3.

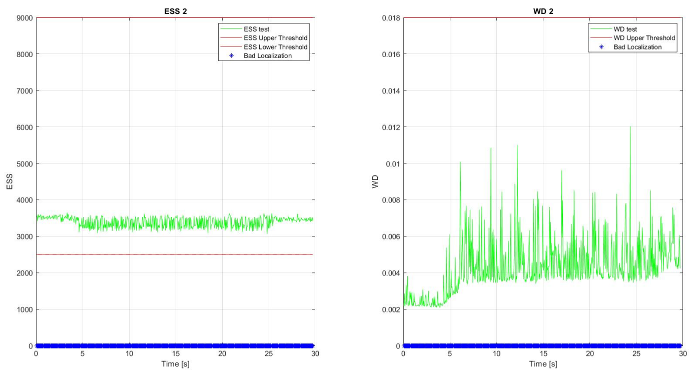

Figure A.36: Coil off – No singularity: ESS and WD parameters, test 2.

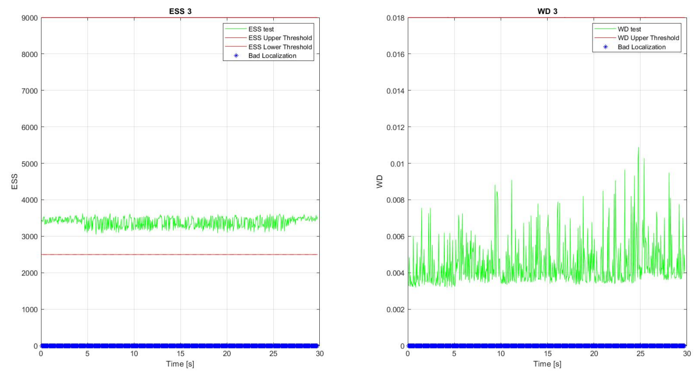

Figure A.37: Coil off – No singularity: ESS and WD parameters, test 3.

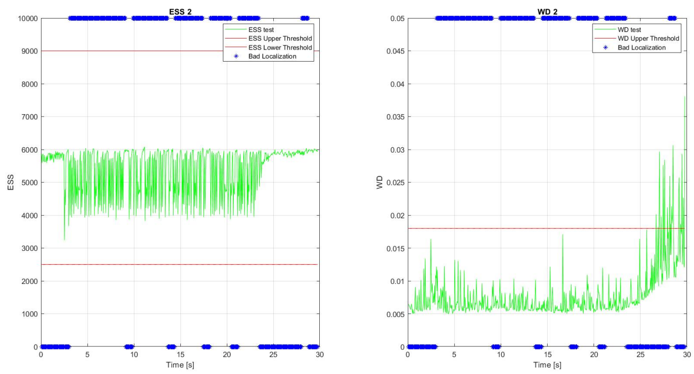

Figure A.38: Coil off – Singularity plane: ESS and WD parameters, test 2.

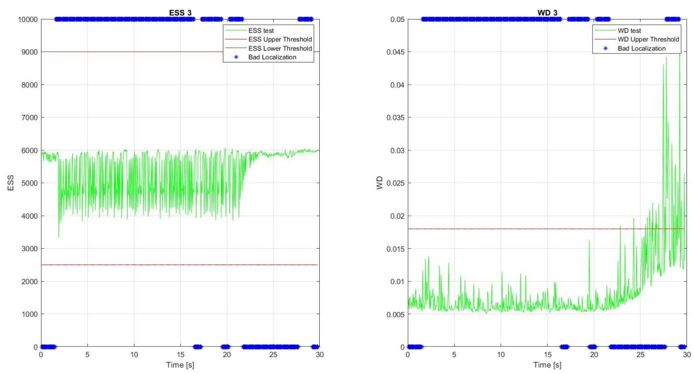

Figure A.39: Coil off – Singularity plane: ESS and WD parameters, test 3.

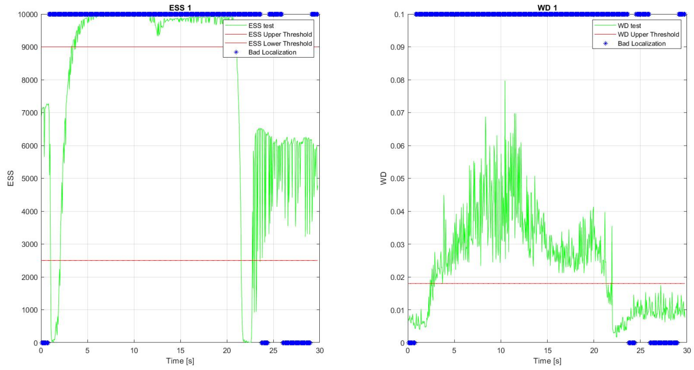

Figure A.40: Endoscope outside the workspace: ESS and WD parameters, test 1.

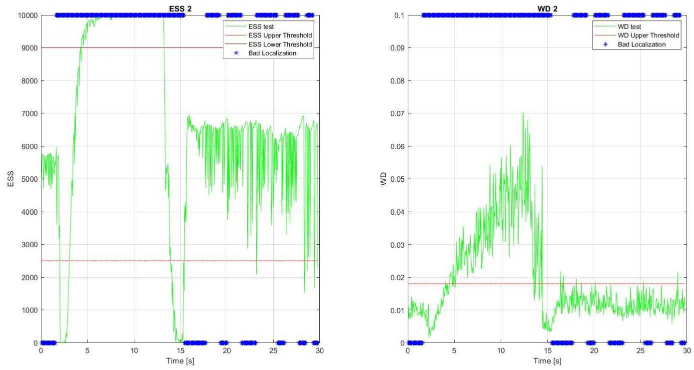

Figure A.41: Endoscope outside the workspace: ESS and WD parameters, test 2.

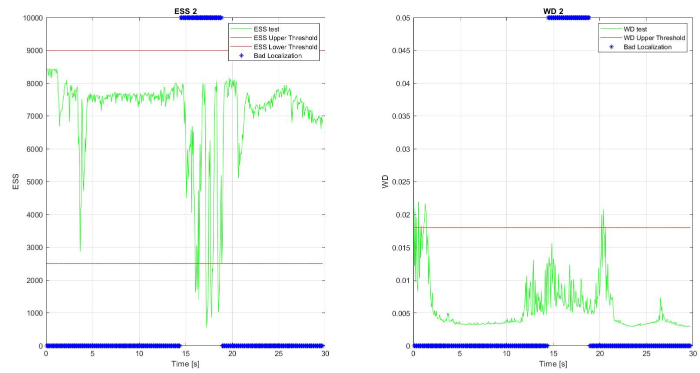

Figure A.42: Joystick movement: ESS and WD parameters, test 2.

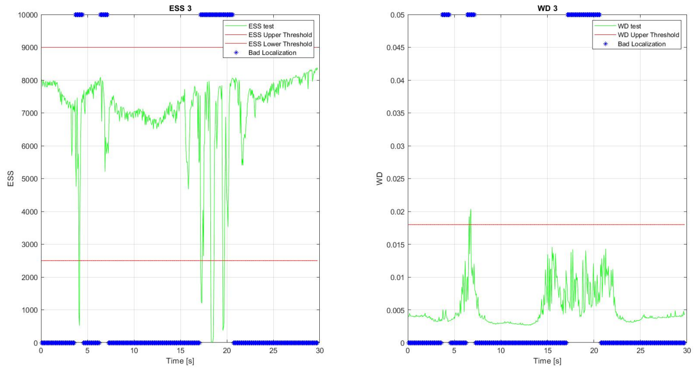

Figure A.43: Joystick movement: ESS and WD parameters, test 3.

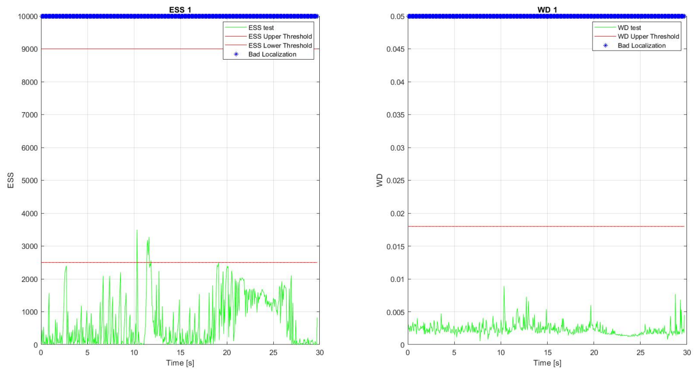

Figure A.44: Wrong calibration: ESS and WD parameters, test 1.

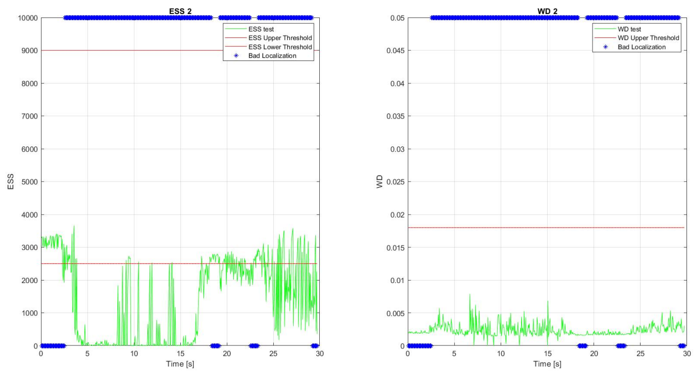

Figure A.45: Wrong calibration: ESS and WD parameters, test 2.

A.2 Validation phase

A.2.1 Static scenarios

All plots of the validation phase for static scenarios are presented below.

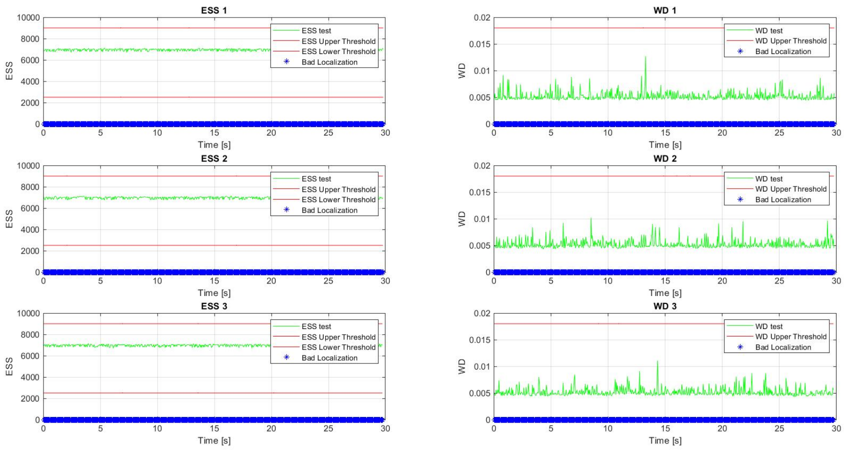

Figure A.46: Stationary situation – No singularity: ESS and WD parameters.

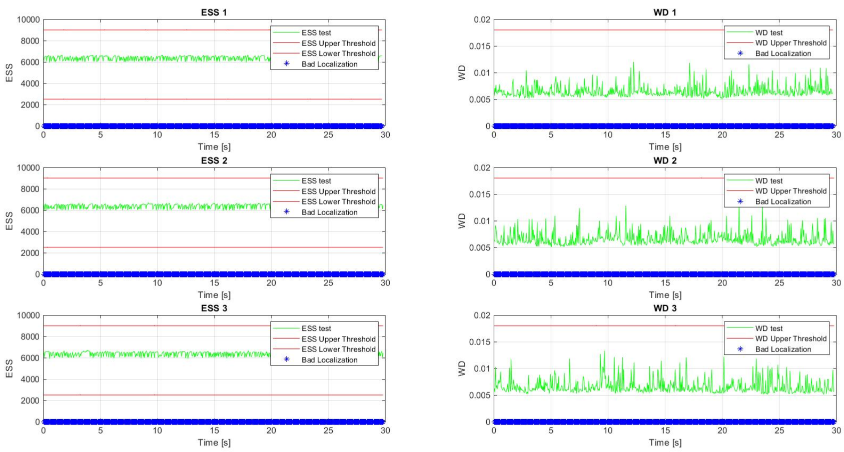

Figure A.47: Stationary situation – Singularity plane: ESS and WD parameters.

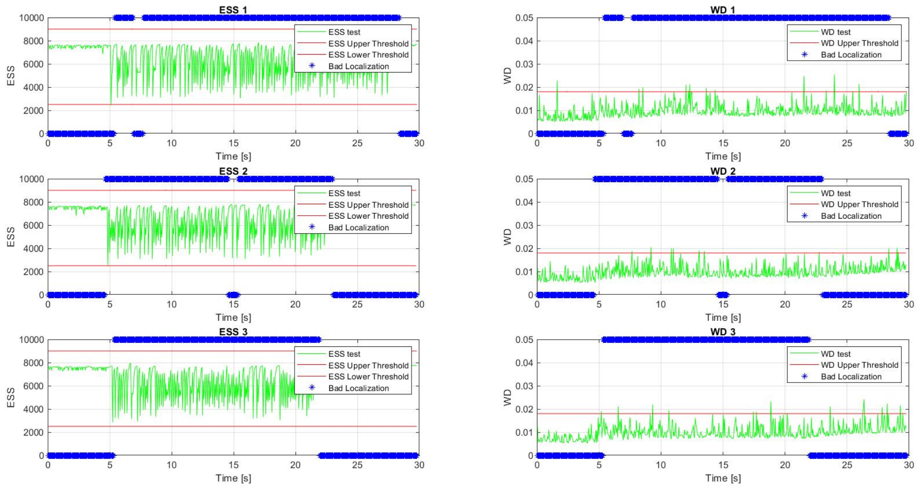

Figure A.48: Coil off – No singularity: ESS and WD parameters.

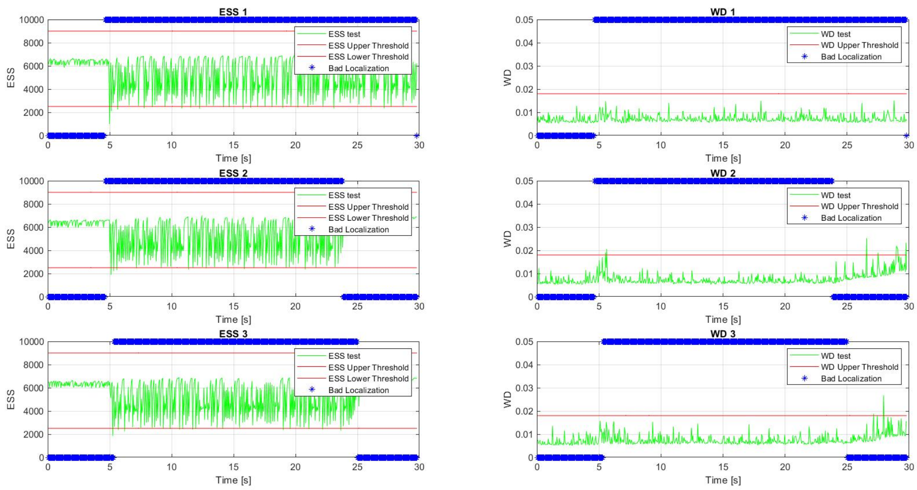

Figure A.49: Coil off – Singularity plane: ESS and WD parameters.

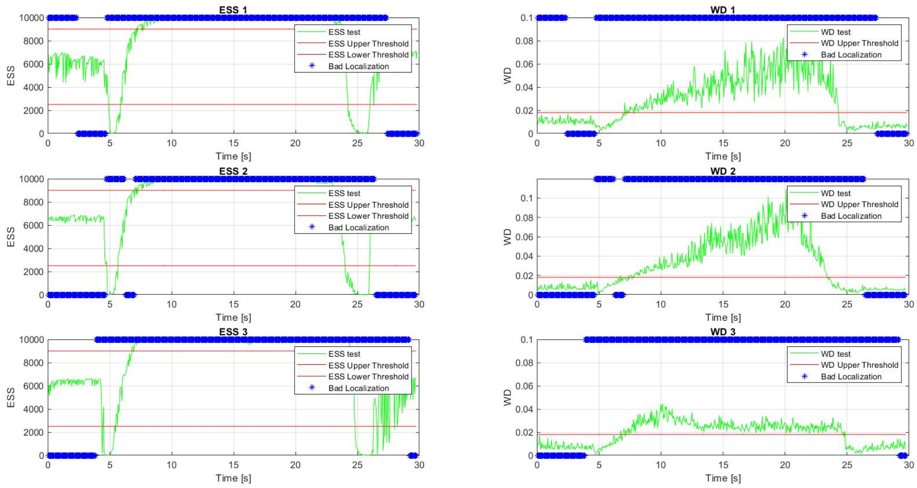

Figure A.50: Endoscope outside the workspace: ESS and WD parameters.

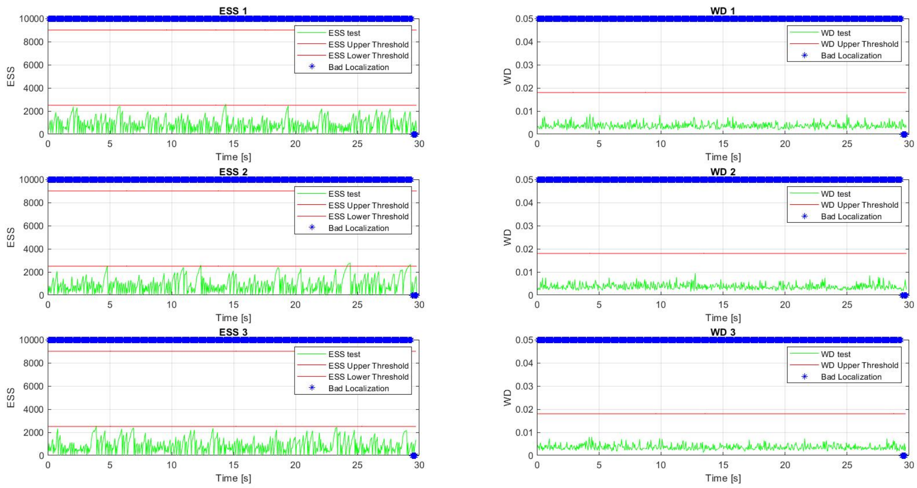

Figure A.51: Wrong calibration: ESS and WD parameters.

A.2.2 Dynamic scenario

The plot of the validation phase for the dynamic scenario is presented below.

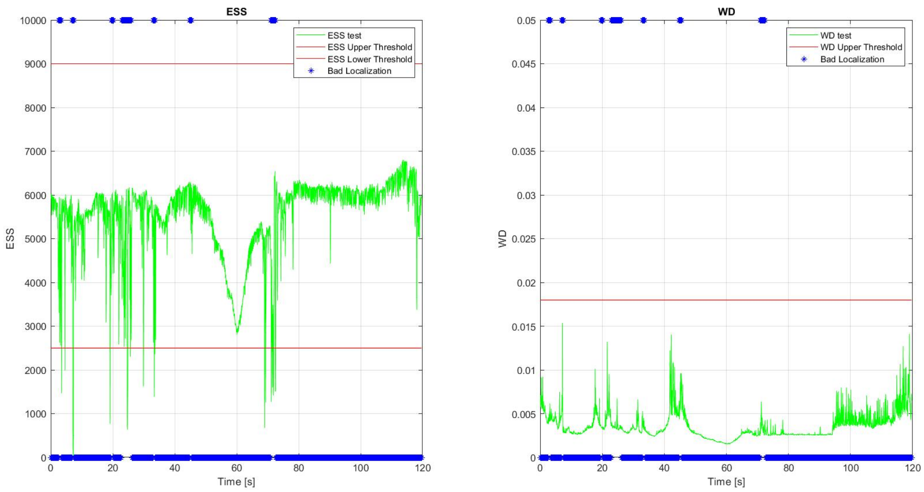

Figure A.52: Joystick movement: ESS and WD parameters.

Appendix B

Explanation of the Code

The implemented code is presented and explained below. The code presented is located within a function in the PF algorithm.

```
// Estimation of localization correctness via parameters
long double particle_weights[N], particle_weights_norm[N];
long double weights_sum = 0, norm_weights_squared_sum=0, ESS;
static long double ESS_old = 5000;

for (int i = 0; i < N; i++) {
    particle_weights[i] = sampler_->GetParticleWeight(i);
    weights_sum += particle_weights[i];
}

for (int i = 0; i < N; i++) {
    particle_weights_norm[i] = particle_weights[i] / weights_sum;
    norm_weights_squared_sum += particle_weights_norm[i]*particle_weights_norm[i];
}

ESS = 1.0 / norm_weights_squared_sum;
ros::NodeHandle nh;

int ESS_increase;
static int block_counter = 0, bad_counter = 0, flag = 0, bad_localization = 0;
block_counter += 1;

if (flag == 0) { // The check is only done if the flag is 0 (not in a bad localization block)
  ESS_increase = abs(ESS - ESS_old);
  if (ESS <= 2500 || ESS >= 9000 || ESS_increase >= 600 || weighted_dists >= 0.018) {
```

```
      bad_counter += 1;
    }

    if (bad_counter >= 7) {  // When at least 7 bad localization points -> bad localization block -> flag 1
      bad_localization = 10000;
      flag = 1;
    }
  }

  if (flag == 1) {
    if (ESS <= 2500) {  // In this case, the problem is probably the wrong calibration of the endoscope
      ROS_WARN_STREAM("Bad localization. The problem is probably an incorrect calibration of the endoscope.");
    }
  }

  ESS_old = ESS;

  if (block_counter == 15) {  // At the end of the 15-point block: start again from 0
    block_counter = 0;
    bad_counter = 0;
    bad_localization = 0;
    flag = 0;
  }

  BL_pub_ = nh.advertise<std_msgs::Float64>("Bad_Localization", 10);
  std_msgs::Float64 BLValue;
  BLValue.data = bad_localization;
  BL_pub_.publish(BLValue);

  ESS_pub_ = nh.advertise<std_msgs::Float64>("ESS", 10);
  std_msgs::Float64 ESSValue;
  ESSValue.data = ESS;
  ESS_pub_.publish(ESSValue);

  WD_pub_ = nh.advertise<std_msgs::Float64>("WD", 10);
  std_msgs::Float64 WDValue;
  WDValue.data = weighted_dists;
  WD_pub_.publish(WDValue);
  // End of estimation

  // Unscented Kalman Filter (UKF)
  static Eigen::Matrix<double, 4, 1> prevState = Eigen::Matrix<double, 4, 1>::Zero();
  static bool isInitialized = false;

```

```
// Define the state covariance matrix
static StateCovarianceMatrix stateCovariance;

if (!isInitialized) {
  smc::rng* prng;
  prng = new smc::rng();
  prevState[0] = prng->Uniform(
          workspace_pos_.x()-workspace_scale_.x()/2,
          workspace_pos_.x()+workspace_scale_.x()/2);
  prevState[1] = prng->Uniform(
          workspace_pos_.y()-workspace_scale_.y()/2,
          workspace_pos_.y()+workspace_scale_.y()/2);
  prevState[2] = prng->Uniform(
          workspace_pos_.z()-workspace_scale_.z()/2,
          workspace_pos_.z()+workspace_scale_.z()/2);
  prevState[3] = prng->Uniform(-M_PI, M_PI);
  delete prng;

  stateCovariance.diagonal() << 0.1, 0.1, 0.1, 0.1;

  isInitialized = true;
}

// Define the measurement noise covariance matrix
MeasurementNoiseCovarianceMatrix measurementNoiseCovariance;
measurementNoiseCovariance.setIdentity();
measurementNoiseCovariance *= 0.00001;

// Define the process noise covariance matrix
ProcessNoiseCovarianceMatrix processNoiseCovariance;
processNoiseCovariance.setZero();
processNoiseCovariance.diagonal() << 0.00015, 0.00015, 0.00015,
  0.01;

// Define the number of sigma points
const int numSigmaPoints = 2 * prevState.rows() + 1;

// Define the sigma points matrix
SigmaPointsMatrix sigmaPoints = SigmaPointsMatrix::Zero();

// Define the weights vector
WeightsVector weights = WeightsVector::Zero();

// Check the error with respect to PF
static int x_counter = 100, y_counter = 100, z_counter = 100;

if (bad_localization == 0) {      // Only check if the PF
  localization is good
```

```
      if (x_[0] - prevState[0] > 0.01 || x_[0] - prevState[0] < -0.01) {
        prevState[0] = x_[0];
        x_counter = 100;
      }
      if (x_[0] - prevState[0] <= 0.01 && x_[0] - prevState[0] >= -0.01) {
        x_counter -= 1;
      }
      if (x_[1] - prevState[1] > 0.01 || x_[1] - prevState[1] < -0.01) {
        prevState[1] = x_[1];
        y_counter = 100;
      }
      if (x_[1] - prevState[1] <= 0.01 && x_[1] - prevState[1] >= -0.01) {
        y_counter -= 1;
      }
      if (x_[2] - prevState[2] > 0.01 || x_[2] - prevState[2] < -0.01) {
        prevState[2] = x_[2];
        z_counter = 100;
      }
      if (x_[2] - prevState[2] <= 0.01 && x_[2] - prevState[2] >= -0.01) {
        z_counter -= 1;
      }
    }

    // Compute the sigma points and weights
    const double lambda = 3 - prevState.rows();
    const double sqrtLambdaPlusN = std::sqrt(lambda + prevState.rows());
    sigmaPoints.col(0) = prevState;
    weights(0) = lambda / (lambda + prevState.rows());
    Matrix<double, 4, 4> sqrt_P = stateCovariance.llt().matrixL();
    for (int i = 0; i < prevState.rows(); i++)
    {
      const VectorXd& prevStateVector = prevState;
      sigmaPoints.col(i + 1) = prevStateVector + (sqrtLambdaPlusN * sqrt_P.col(i));
      sigmaPoints.col(i + 1 + prevState.rows()) = prevStateVector - (sqrtLambdaPlusN * sqrt_P.col(i));
      weights(i + 1) = weights(i + 1 + prevState.rows()) = 0.5 / (lambda + prevState.rows());
    }

    // Compute the predicted sigma points: Random Walk Process Model
    SigmaPointsMatrix predictedSigmaPoints = sigmaPoints;
```

```
bool yaw_correct = false;
double coil_mean_norm_mT = coil_mean_mT.norm();
if (yaw_correct_config_)
{
  yaw_correct = true;
}

int in_sing = 0;
bool pl_use_x_target = false;
double pcoef = 1.0;
dt_ = 0.01;
smc::rng* prng;
prng = new smc::rng();
if (yaw_correct)
{
  if (coil_mean_norm_mT > 20e-3 && !cur_obs_.mfs_coil10.hasNaN())
  {
    if ((in_sing != 3) && (epm_var_mT.array() <
 yaw_correction_var_threshold).all())
    {
      if (!pl_use_x_target)
      {
        for (int i = 0; i < 9; i++) {
          predictedSigmaPoints.row(3)[i] = pcoef*sigmaPoints.row(3)
 [i] + prng->Normal(0, stdYaw/10000.0);
        }
      }
      else
      {
        for (int i = 0; i < 9; i++) {
          predictedSigmaPoints.row(3)[i] = pcoef*sigmaPoints.row(3)
 [i] + dt_*(x_target_[3] - sigmaPoints.row(3)[i]) + prng->Normal(0,
 stdYaw/10000.0);
        }
      }
    }
  }
}

if (!yaw_correct_config_)
{
  for (int i = 0; i < 9; i++) {
    predictedSigmaPoints.row(3)[i] = last_known_yaw_err_;
  }
}
double stdxyz = stdXYZ;
for (int i = 0; i < 3; i++)
{
  if (!pl_use_x_target)
```

```
    {
      for (int j = 0; j < 9; j++) {
        predictedSigmaPoints.row(i)[j] = pcoef*sigmaPoints.row(i)[j]
 + prng->Normal(0, stdxyz/10000.0);
      }
    }
    else
    {
      for (int j = 0; j < 9; j++) {
        predictedSigmaPoints.row(i)[j] = pcoef*sigmaPoints.row(i)[j]
 + dt_*(x_target_[i] - sigmaPoints.row(i)[j]) + prng->Normal(0,
 stdxyz/10000.0);
      }
    }
  }
  delete prng;

  // Compute the predicted state
  StateVector predictedState = predictedSigmaPoints * weights;

  // Compute the predicted state covariance
  StateCovarianceMatrix predictedStateCovariance =
   processNoiseCovariance;
  for (int i = 0; i < numSigmaPoints; i++)
  {
    const StateVector& sigmaPoint = predictedSigmaPoints.col(i);
    StateVector diff = sigmaPoint - predictedState;

    // Perform angle normalization to make sure that the angle yaw is
     within -Pi and Pi
    while (diff(3) > M_PI) diff(3) -= 2. * M_PI;
    while (diff(3) < -M_PI) diff(3) += 2. * M_PI;

    predictedStateCovariance += weights(i) * (diff * diff.transpose()
   );
  }

  // Compute the predicted measurement sigma points
  MeasurementSigmaPointsMatrix predictedMeasurementSigmaPoints =
   MeasurementSigmaPointsMatrix::Zero();
  Vector3d pos;
  pos.setZero();
  double dyaw = 0;

  for (int i = 0; i < numSigmaPoints; i++)
  {
    const StateVector& predictedStateVector = predictedSigmaPoints.
   col(i);
    pos[0] = predictedStateVector[0];
```

```
    pos[1] = predictedStateVector[1];
    pos[2] = predictedStateVector[2];
    dyaw = predictedStateVector[3];

    Eigen::Matrix3d Rc = cur_obs_.R_capsule_world;

    Affine3d T_particle_world;
    T_particle_world.translation() = pos +  capsule_delta_position_;
    T_particle_world.linear() = AngleAxisd(dyaw, Vector3d::UnitZ()) * Rc;
    MfsSensor_t calc_epm;
    MfsSensor_t calc_coil;
    ToSensorReading(T_particle_world, calc_epm, calc_coil);

    predictedMeasurementSigmaPoints(0,i) = calc_epm(0);
    predictedMeasurementSigmaPoints(1,i) = calc_epm(1);
    predictedMeasurementSigmaPoints(2,i) = calc_epm(2);
    predictedMeasurementSigmaPoints(3,i) = calc_epm(3);
    predictedMeasurementSigmaPoints(4,i) = calc_epm(4);
    predictedMeasurementSigmaPoints(5,i) = calc_epm(5);
    predictedMeasurementSigmaPoints(6,i) = calc_coil(0);
    predictedMeasurementSigmaPoints(7,i) = calc_coil(1);
    predictedMeasurementSigmaPoints(8,i) = calc_coil(2);
    predictedMeasurementSigmaPoints(9,i) = calc_coil(3);
    predictedMeasurementSigmaPoints(10,i) = calc_coil(4);
    predictedMeasurementSigmaPoints(11,i) = calc_coil(5);
  }

  // Compute the predicted measurement
  MeasurementVector predictedMeasurement = predictedMeasurementSigmaPoints * weights;

  // Compute the predicted measurement covariance
  MeasurementNoiseCovarianceMatrix predictedMeasurementCovariance = MeasurementNoiseCovarianceMatrix::Zero();
  for (int i = 0; i < numSigmaPoints; i++)
  {
    const MeasurementVector& predictedMeasurementVector = predictedMeasurementSigmaPoints.col(i);
    const MeasurementVector& diff = predictedMeasurementVector - predictedMeasurement;
    predictedMeasurementCovariance += weights(i) * (diff * diff.transpose());
  }
  predictedMeasurementCovariance += measurementNoiseCovariance;

  // Compute the cross-covariance matrix
  Matrix<double, 4, 12> measurementFunctionJacobian = Matrix<double, 4, 12>::Zero();
```

```
for (int i = 0; i < numSigmaPoints; i++)
{
  const StateVector& predictedStateVector = predictedSigmaPoints.col(i);
  StateVector diff = predictedStateVector - predictedState;

  // Perform angle normalization to make sure that the angle yaw is within -Pi and Pi
  while (diff(3) >  M_PI) diff(3) -= 2. * M_PI;
  while (diff(3) < -M_PI) diff(3) += 2. * M_PI;

  const MeasurementVector& predictedMeasurementVector = predictedMeasurementSigmaPoints.col(i);
  const MeasurementVector& measurementDiff = predictedMeasurementVector - predictedMeasurement;
  measurementFunctionJacobian += weights(i) * (diff * measurementDiff.transpose());
}
KalmanGainMatrix kalmanGain = measurementFunctionJacobian * predictedMeasurementCovariance.inverse();

// Compute the updated state
MeasurementVector measurement = MeasurementVector::Zero();
measurement(0) = cur_obs_.mfs_epm(0);
measurement(1) = cur_obs_.mfs_epm(1);
measurement(2) = cur_obs_.mfs_epm(2);
measurement(3) = cur_obs_.mfs_epm(3);
measurement(4) = cur_obs_.mfs_epm(4);
measurement(5) = cur_obs_.mfs_epm(5);
measurement(6) = cur_obs_.mfs_coil(0);
measurement(7) = cur_obs_.mfs_coil(1);
measurement(8) = cur_obs_.mfs_coil(2);
measurement(9) = cur_obs_.mfs_coil(3);
measurement(10) = cur_obs_.mfs_coil(4);
measurement(11) = cur_obs_.mfs_coil(5);

StateVector nextState = predictedState + kalmanGain * (measurement - predictedMeasurement);
prevState = nextState;

// Compute the updated state covariance
stateCovariance = predictedStateCovariance - kalmanGain * predictedMeasurementCovariance * kalmanGain.transpose();

x_pub_ = nh.advertise<std_msgs::Float64>("UKF/position/x", 10);
std_msgs::Float64 xValue;
xValue.data = nextState[0];
x_pub_.publish(xValue);

```

```
y_pub_ = nh.advertise<std_msgs::Float64>("UKF/position/y", 10);
std_msgs::Float64 yValue;
yValue.data = nextState[1];
y_pub_.publish(yValue);

z_pub_ = nh.advertise<std_msgs::Float64>("UKF/position/z", 10);
std_msgs::Float64 zValue;
zValue.data = nextState[2];
z_pub_.publish(zValue);

Eigen::Quaterniond q;
q = Eigen::AngleAxisd(nextState[3], Vector3d::UnitZ()) * cur_obs_.R_capsule_world;
// origially localization was considering z positive in direction of view of the endoscope,
// the new convention is with x positive (see confluence) so I am rotating the final result here
q = q * Eigen::AngleAxisd(M_PI/2, Vector3d::UnitZ());
q = q * Eigen::AngleAxisd(-M_PI/2, Vector3d::UnitY());

qx_pub_ = nh.advertise<std_msgs::Float64>("UKF/orientation/x", 10);
std_msgs::Float64 qxValue;
qxValue.data = q.x();
qx_pub_.publish(qxValue);

qy_pub_ = nh.advertise<std_msgs::Float64>("UKF/orientation/y", 10);
std_msgs::Float64 qyValue;
qyValue.data = q.y();
qy_pub_.publish(qyValue);

qz_pub_ = nh.advertise<std_msgs::Float64>("UKF/orientation/z", 10);
std_msgs::Float64 qzValue;
qzValue.data = q.z();
qz_pub_.publish(qzValue);

qw_pub_ = nh.advertise<std_msgs::Float64>("UKF/orientation/w", 10);
std_msgs::Float64 qwValue;
qwValue.data = q.w();
qw_pub_.publish(qwValue);
// End of UKF

// Deciding between PF and UKF
if (x_[0] - nextState[0] <= 0.006 && x_[0] - nextState[0] >= -0.006 && x_counter < 0) {
  x_[0] = nextState[0];
}
if (x_[1] - nextState[1] <= 0.006 && x_[1] - nextState[1] >= -0.006 && y_counter < 0) {
  x_[1] = nextState[1];
```

```
368 }
369 if (x_[2] - nextState[2] <= 0.006 && x_[2] - nextState[2] >= -0.006
      && z_counter < 0) {
370  x_[2] = nextState[2];
371 }
372 // End of decision
```

Lines 1-64: Estimation of localization correctness via parameters

- **Lines 2-17**: calculation of the ESS parameter; the WD parameter was previously calculated in the PF code.
- **Lines 19-48**: definition of when localization is good ($bad\_localization = 0$) or when it is not good ($bad\_localization = 10000$).
- **Lines 50-63**: publication of the parameters ESS and WD and the value $bad\_localization$.

Lines 66-360: Unscented Kalman Filter algorithm

- **Lines 67-101**: initialization of the state and covariance matrices.
- **Lines 103-137**: if the localization of the PF is good, it is checked whether the difference between the values of the state variables estimated by the UKF and those estimated by the PF is greater than 10 mm. If so, the value of the UKF is forced to be around the PF, and the counter is set to 100. If it is not, the counter is decremented. The counter is used to determine whether the estimates given by the UKF are stable: when the counter goes below a certain threshold, it means that the variable under consideration has not been forced to stay around the PF for a certain period of time and is, therefore, stable.
- **Lines 139-151**: definition of sigma points and their weights.
- **Lines 153-212**: application of Random Walk Process Model to sigma points. As can be seen, the values $stdYaw$ and $stdxyz$ have been divided by 10000, and this is an important difference from PF (where the values are not divided). This is due to the fact that in order not to make the UKF diverge, more importance must be given to the second part of the algorithm, i.e., the part where the measurements from the sensors are used.
- **Lines 214-229**: calculation of the predicted state and predicted state covariance matrix.

- **Lines 231-266**: the magnetic field model is used for each of the sigma points in order to estimate the value given by the sensors if they were at the estimated position.
- **Lines 268-295**: calculation of the predicted measurement, of the predicted measurement covariance matrix, and of the cross-covariance matrix.
- **Lines 296-317**: calculation of the Kalman Gain Matrix; sensors measurement values are taken, which are used to calculate the new state, taking into account both the predicted state and the difference between the sensors measurements and those calculated using the magnetic field model. The state covariance matrix is also calculated.
- **Lines 319-332**: publication of the UKF's estimated position.
- **Lines 334-359**: calculation of the quaternion corresponding to the roll, pitch and yaw angles and publication of the quaternion. Roll and pitch are previously estimated by the Mahoney filter, while yaw is estimated by the UKF.

Lines 362-372: Decision between the PF and UKF estimates

- **Lines 363-371**: in general, the state used is that of the PF. If, however, the state estimated by the UKF is close to that of the PF (difference less than or equal to 6 mm) and is stable (counter below a certain threshold), the state estimated by the UKF is used.

Acknowledgements

I would like to dedicate this space to those who have stood by me throughout my academic journey, lending their support and playing an instrumental role in bringing this work to fruition.

I wish to extend my gratitude to Professor Alessandro Rizzo for affording me the opportunity to undertake my thesis project within the realm of robotics.

I want to sincerely thank Bruno Scaglioni, my supervisor at Leeds, for his guidance during the past eight months while I worked on this project. Your availability and advice have been incredibly valuable to me.

I would like to thank the entire STORM Lab, which stood by me throughout my entire stay in Leeds. In particular, I extend my gratitude to James and Nikita, whose willingness allowed me to conduct various experiments that proved invaluable for my thesis.

Sono profondamente grato ai miei genitori, Clara ed Alberto, i quali da sempre mi sostengono nella realizzazione dei miei progetti. La mia gratitudine si estende ai miei fratelli, Andrea e Matteo, e a mia sorella, Anna, per essere stati sempre presenti e pronti ad aiutarmi quando ne ho avuto bisogno.

Un ringraziamento speciale va a mio gemello, Luca, punto di riferimento insostituibile in ogni aspetto della mia vita. Ti sono grato per i preziosi consigli che mi offri, per la tua costante vicinanza e per i momenti di spensieratezza che condividiamo insieme.

Un ringraziamento di cuore va ad Irene. Grazie per il tempo prezioso che mi dedichi ogni giorno. La tua presenza costante e il tuo incoraggiamento rappresentano due elementi fondamentali per la concretizzazione di ogni mio progetto. Grazie per tutto l'affetto e la forza che mi regali ogni giorno.